Applications of Kinetic Inductance:

Parametric Amplifier & Phase Shifter,

2DEG Coupled Co-planar Structures &

Microstrip to Slotline Transition at RF Frequencies

by

Harshad Surdi

A Thesis Presented in Partial Fulfilment
of the Requirements for the Degree
Master of Science

Approved April 2016 by the
Graduate Supervisory Committee:

Philip Mauskopf, Chair
James T. Aberle
Georgios Trichopoulos

ARIZONA STATE UNIVERSITY

May 2016

ABSTRACT

Kinetic inductance springs from the inertia of charged mobile carriers in alternating electric fields and it is fundamentally different from the magnetic inductance which is only a geometry dependent property. The magnetic inductance is proportional to the volume occupied by the electric and magnetic fields and is often limited by the number of turns of the coil. Kinetic inductance on the other hand is inversely proportional to the density of electrons or holes that exert inertia, the unit mass of the charge carriers and the momentum relaxation time of these charge carriers, all of which can be varied merely by modifying the material properties. Highly sensitive and broadband signal amplifiers often broaden the field of study in astrophysics. Quantum-noise limited travelling wave kinetic inductance parametric amplifiers offer a noise figure of around 0.5 K $\pm$ 0.3 K as compared to 20 K in HEMT signal amplifiers and can be designed to operate to cover the entire W-band (75 GHz – 115 GHz).

The research cumulating to this thesis involves applying and exploiting kinetic inductance properties in designing a W-band orthogonal mode transducer, quadratic gain phase shifter with a gain of ~49 dB over a meter of microstrip transmission line. The phase shifter will help in measuring the maximum amount of phase shift $\Delta\phi_{\max}(I)$ that can be obtained from half a meter transmission line which helps in predicting the gain of a travelling wave parametric amplifier. In another project, a microstrip to slot line transition is designed and optimized to operate at 150 GHz and 220 GHz frequencies, that is used as a part of horn antenna coupled microwave kinetic inductance detector proposed to operate from 138 GHz to 250 GHz. In the final project, kinetic inductance in a 2D electron gas (2DEG) is explored by design, simulation, fabrication and experimentation. A transmission line model of a 2DEG proposed by Burke (1999), is simulated and verified experimentally by fabricating a capacitvely coupled 2DEG mesa structure. Low temperature experiments were done at 77 K and 10 K with photo-doping the 2DEG. A circuit model of a 2DEG coupled co-planar waveguide model is also proposed and simulated.

ACKNOWLEDGMENTS

First and foremost, I would like to thank Dr. Philip Mauskopf for his ever present guidance and support during these two years of research. I have always been inspired by Phil's methods of formulating an idea, it's mathematical validation and practical execution and have always tried and will continue to incorporate them in my research. This thesis would not have been possible without Phil's deep-rooted knowledge and expertise.

I would also like to thank Dr. James Aberle and Dr. Georgios Trichopoulus for being part of my graduate advisory committee. I am also truly grateful to Prof. Chris Groppi for putting his trust in me and giving me the opportunity to join the research group. I would like to thank Hamdi Mani for helping with the experimental setups, Sam Gordon for collaborating on a project, George Che for sharing his fabrication expertise and all my other lab mates for their support. I would also like to commend all the helpful people at ASU's CSSER NanoFab and Dmitry Morozov at Cardiff University and Preston Webster at ASU for providing heterojunction wafers.

My parents, my elder brother and my sister-in-law have always supported and encouraged my pursuit of higher education and I will always be indebted to them. I would also like to commend my friends Rahul Wagh, Yash Mehta, Amey Thorat, Yogesh Palkar and Indraneel Damle for always keeping me grounded.

Last but not the least, I extend my acknowledgements to David Gilmour, Roger Waters, Richard Wright, Nick Mason and Syd Barrett a.k.a. the Pink Floyd for their soul reaching and ever inspiring music.

TABLE OF CONTENTS

CHAPTER Page

3. PART II – MICROSTRIP TO SLOTLINE TRANSITION

LIST OF TABLES

LIST OF FIGURES

Figure Page

Figure Page

Figure Page

Figure Page

Figure Page

Figure Page

Figure Page

CHAPTER 1.

INTRODUCTION AND THESIS ORGANIZATION

This thesis revolves around three applications of kinetic inductance (directly and indirectly). The thesis is divided into three parts (Chapter 2, 3, 4) each part elucidating each individual distinct (though not completely disconnected) projects.

First part of the research work in this thesis deals with travelling wave kinetic inductance parametric amplifier and phase shifter. We have designed and simulated a kinetic inductance phase shifter which is the initial step in realizing a W-band parametric amplifier. Chapter 2 goes through the basics of parametric amplification, non-linear current controlled phase shift, kinetic inductance and how it plays a part in the phase shift, an orthogonal mode transducer (OMT) that employs a W-band circular waeguide to microstrip transition and proposes a fabrication and testing procedure.

Second part of the thesis details the second project which involves a microstrip (MS) -to-slot line (SL) transition for a microwave kinetic inductance detector coupled to a horn coupled antenna operating from 138 GHz to 250 GHz. We design and optimize the MS to SL optimization using Sonnet Suite EM simulator to obtain high transmission coefficient and low reflection loss at 150 GHz and 220 GHz.

Third part of the thesis elaborates the last project which involves theorizing and verification of 2D electron gas (2DEG) coupling to transmission lines & co-planar structures. We design, simulate, fabricate and experimentally verify a capacitively coupled 2DEG mesa structure whose circuit model is proposed by Burke (1999). The chapter goes through the source of kinetic inductance in a 2DEG system, transmission line model of a 2DEG, Sonnet simulations of 2DEG capacitve coupling and finally experimental verification of the circuit model. Finally, attempts are made to theorize and simulate a circuit model of a 2DEG coupled to a co-planar waveguide (2DEG-CPW). It is analytically shown that the simulation results match with theoretical relations.

CHAPTER 2.

PART I

TRAVELLING WAVE KINETIC INDUCTANCE PARAMETRIC AMPLIFIERS AND PHASE SHIFTER

2.1 Introduction

Many astronomical objects are not only observable in visible light but also emit radiation at radio and microwave frequencies. In fact, the cosmic microwave background (CMB) has its spectral radiance peaking at 160.2 GHz [2] in the microwave range of frequencies. Besides observing energetic objects such as pulsars and quasars, radio astronomy enables to “image” most astronomical objects such galaxies, nebulae and even radio emissions from planets. One such astronomical instrumentation that images radio frequencies is the Atacama Large Millimeter/Submillimeter Array (ALMA) The ALMA is an astronomical interferometer of radio telescopes situated in the desert of northern Chile that observes and provides insight on star birth during the early universe and detailed imaging of local star and planet formation [3]. RF and microwave receivers are a crucial part of these astronomical instrumentation. Some of the crucial characteristics that qualify a good receiver are

a) *Efficiency* - which indicates how much of the incident EM radiation photons are converted into detectable signals. Efficiency is often limited by the signal-to-noise ratio of the receiver.

b) *Dynamic range* - which indicates the ratio between the strongest signal falling on the receiver and the weakest measureable signal (or noise level).

c) *Resolution* – this can be thought of as the area over which an infinitely narrow signal is spread. Resolution is limited by the number of detectors and the baseline noise level of each detector.

d) *Dark current and readout noise* – often emerging from leakage and dissipation within the receiver.

In general, the noise of the receiver plays an extremely crucial and a limiting factor in astronomical instrumentation and especially in signal amplification. Although advances in semiconductor technology is reducing the overall noise figure in solid-state detectors and amplifiers, their noise levels increase with frequency of operation simultaneously decreasing the gain-bandwidth product. The most recent development in high electron mobility transistors (HEMT) reports a noise figure of 1.3 K at 5.2 GHz [4] while ≤ 20 K noise over 6 GHz to 50 GHz frequency range is reported for indium phosphide (InP) low noise amplifiers (LNA) [5].

Superconductor-insulator-superconductor junctions (SIS) and other superconductor based amplifier circuits have always shown low noise characteristics in comparison to semiconductor amplifiers. Figure 2.1 shows an early (1990) comparison of Schottky mixer receiver noise temperature and SIS mixer receiver in the GHz range.

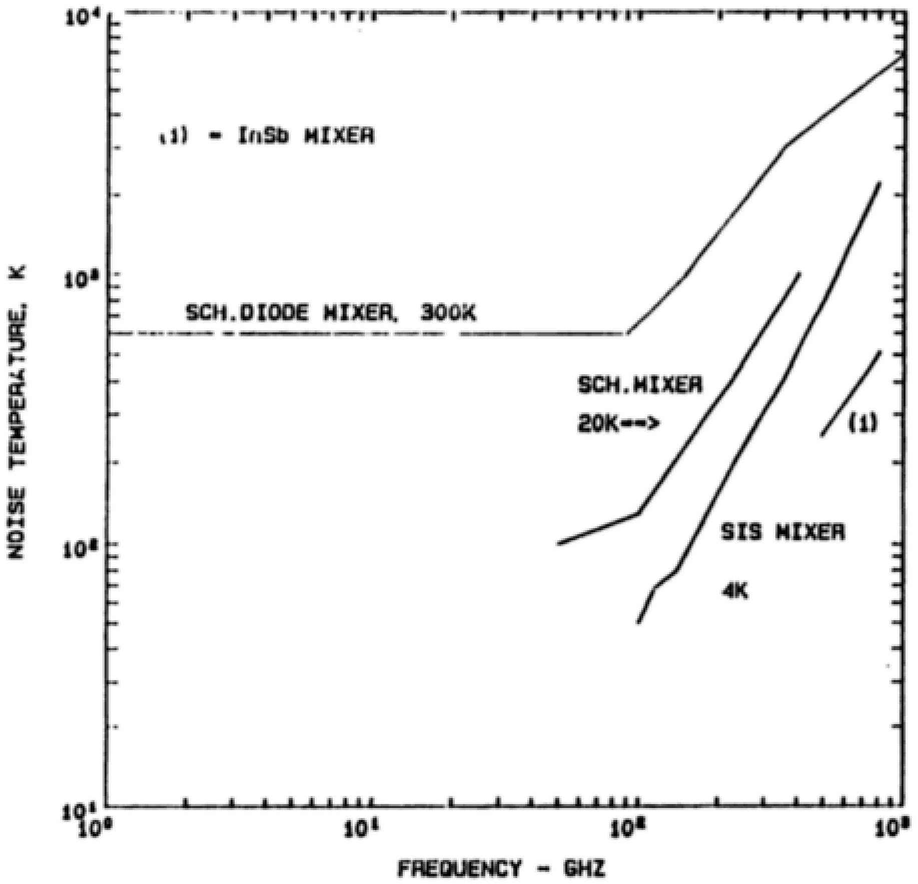

Figure 2.1 Early comparison of semiconductor schottky mixer receiver and a superconductor-insulator-superconductor mixer receiver [6]

2.2 DC-RF Power Amplification vs. RF-RF Power Amplification

In field effect transistor (FET) amplifiers, gain is achieved by increasing the current by modulating the channel of the active device and thus decreasing the transconductance of the transistor. The power in FET amplifiers is flown at DC to amplify signals either at DC or RF frequencies. One of the other ways to achieve amplification is to let the power flow at RF frequencies and thus achieving a RF-RF power conversion. To achieve RF-RF power amplification, parametric amplification is one of the ways and the main theme of this part of the thesis. Parametric power amplifiers being based on amplification using reactive elements in the circuit, they are capable of having a near perfect RF-RF power conversion. Also, parametric amplifiers are not limited by the gain-bandwidth product of the transconductance based amplifiers. Such advantages of parametric amplifiers over transconductance amplifiers are particularly exploited in radio astronomy [7] & [8]. In the rest of the chapter travelling wave kinetic inductance parametric amplifiers will be discussed in details.

2.3 Scientific Motivation for W-band Frequency

The W-band (75 GHz to 115GHz) portion of the electromagnetic spectrum is a rich field for observing astrophysical phenomena of inter-galactic, extragalactic and cosmological origin. The lower frequency range contains the CMB foreground minimum (70 - 100 GHz), where the dust and synchrotron spectral energy distributions reach their lowest magnitudes. This region of the spectrum is frequently used to study the CMB polarization anisotropies [9]. Several instruments and surveys have studied the thermal and kinematic Sunyaev-Zeldovich (SZ) effect in W-band [8] & [10]. The SZ effect is a CMB temperature anisotropy caused by inverse Compton scattering of CMB photons passing through the hot intra-cluster medium of galaxy clusters. The scale of the effect is independent of redshift, and can be used to probe structure formation in the early universe, as well as to constrain cosmological parameters, including dark energy. ALMA Band 3 (84 - 116 GHz), which covers most of W-band, contains a variety of molecular lines, including CO, which are used as molecular hydrogen tracers. These lines probe the kinematics, temperatures and densities at sub-arc second scales in nearby molecular clouds. The continued study of the small scale dynamics around dark cores and protostellar disks will lead to a better understanding of the energy balance between turbulence and magnetic fields, and their role in determining Galactic star formation rates [11]. Line surveys with ALMA can also be carried out to search for previously undetected organic species, and to characterize the complex chemistry that exists around protostars and protoplanetary disks. Cold molecular gas in the interstellar medium can also be studied in absorption of radiation from extragalactic sources, and redshifted CO lines falling in W-band can be used to study the gas, dust and star formation history in sub-millimeter galaxies (SMGs) between $1 \leq z \leq 3$ [12].

2.4 Parametric Excitation

2.4.1 Harmonic Oscillator

In a system that exhibits harmonic oscillations, it typically consists of an entity displaced from its equilibrium and then a restoring force acting on the entity to bring it back to equilibrium. The simplest example would that be of a pendulum (Figure 2.2) in which the tension in the string and gravity are both in equilibrium when the pendulum is stationary in a vertical position. As soon as the pendulum is disturbed from the vertical position in either direction, the equilibrium between the tension in the string and gravity is disturbed. The force of tension in the string now acts at an angle to the gravitational force and only the parallel component of tension is counterbalanced by gravity. The perpendicular component of the tension is now unbalanced and acts as the restoring force in the system. However, due to the inertia of the pendulum, it continues to swing to the other side of the equilibrium and the restoration force due to the perpendicular component of tension now changes direction which makes the pendulum swing back again towards the equilibrium position. This back and forth movement of the pendulum can be thought of as oscillations of the relative position of the pendulum from its mean vertical position. An amplitude and frequency can be associated with this simple oscillator accounting for the maximum displacement of the pendulum from its mean position and the time it takes for one complete back and forth swing, respectively. Considering no damping forces such as friction and relatively small displacement from its mean position, the motion of the pendulum can be described to be a simple “harmonic” oscillation in a sense that the angular acceleration is directly proportional to the displaced angle measured from the vertical position.

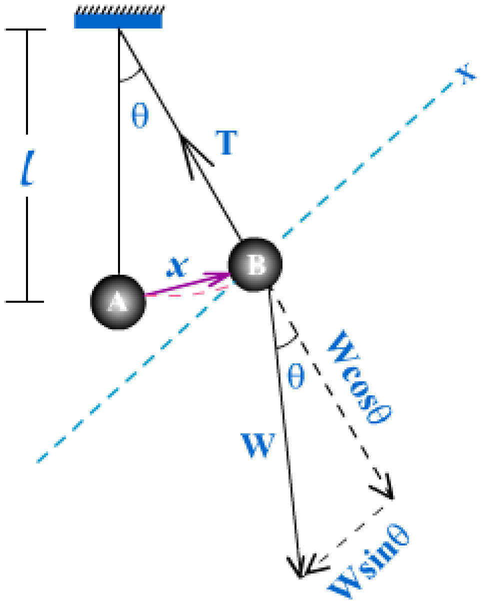

Figure 2.2 Forces of string tension and gravity acting upon the pendulum bob. Component of the gravitational pull counteracts the tension in the string.

The forces balancing on the string are, weight of the bob (W) acting vertically downward and tension in the string (T) acting along the string. The weight of the bob can be resolved into two rectangular components - $Wcos\,\theta$, along the string and $Wsin\,\theta$, perpendicular to the string. Since there is no motion along the string, the component $Wcos\ \theta$ must balance tension T, therefore $Wcos\ \theta = T$. So only $Wsin\ \theta$ component is the net force which is responsible for the acceleration in the bob of the pendulum. Therefore, by Newton’s second law of motion,

$$-Wsin\ \theta = m \times a \tag{2.1}$$

But since $W = mg$, we have $m \times a = -m \times g \sin\theta$ or

$$a = -g\ sin\ \theta \tag{2.2}$$

θ being very small for small displacements, we can assume $\sin\theta = \theta$, therefore

$$a = -g\ \theta \tag{2.3}$$

If x is the linear displacement in the bob from its mean position, the arc AB is nearly equal to x. Therefore, from Figure 2.2, we can say $\theta = x/l$. Substituting the value of θ in (2.1) we get,

$$a = -g\frac{x}{l} \tag{2.4}$$

And thus,

$$a \propto -x \tag{2.5}$$

satisfying a simple harmonic oscillator condition.

2.4.2 Parametric Oscillation

Extending further from the concept of a simple harmonic oscillator and the analogy of a pendulum suspended by a string, now consider if the length of the string was increased as the pendulum passes through the centre and decreased as the pendulum reaches the maximum side on either side of the centre. This change in the length of the string or a “parameter” of the pendulum system causes the amplitude of the pendulum swing to increase progressively. The change or the “forcing” of the parameter now has to be done at twice the frequency of the pendulum swing, once when the pendulum is at either maximum deflection from the centre and once when the pendulum is at the centre. So often the parametric amplification works at a frequency different than the natural oscillating frequency of a system since we want to amplify the output of a system before every oscillation of the system. However, to this system of the pendulum is a nonlinear system since the gravitational force which is the restoration force here, is directly proportional to the sine of the angle of deflection rather than just the angle itself. The parametric oscillator principle will be best understood by looking at the parametric resonance in a linear resonator [13] elaborated as follows. Figure 2.3 shows a rigid rod suspended on a freely rotating axis. Two identical weights are balanced on the rod at equal distance from the centre of the rod.

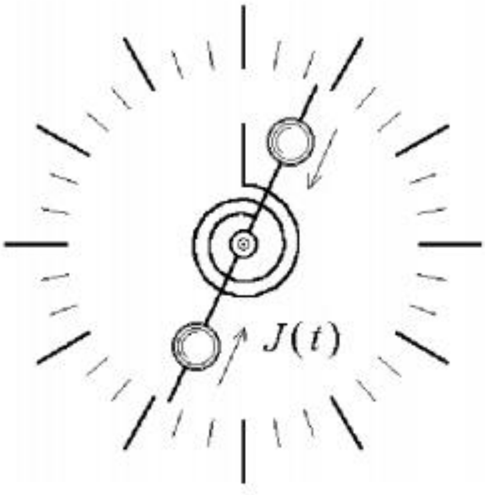

Figure 2.3 A torsion spring oscillator with a balanced rotor whose moment of inertia is forced to vary periodically [12].

A spiral spring with one of its ends attached to the rod and other fixed to an immovable support provides the restoring torque $-D\varphi$ to the rod when it displaces by an angle φ with respect to the initial angle. The two identical weights can be shifted towards and away from the axis on the rod which then changes the moment of inertia J of the rod-weights-spring system which we can call it as a rotor. When the weights are balanced nearer to the axis, the moment of inertia J of the rotor decreases and when the weights are balanced away from the axis the moment of inertia increases. So, for a certain position of the balanced weights, the moment of inertia J will cause the rotor to oscillate at a natural frequency given by $\omega_0 = \sqrt{\frac{D}{J}}$. This means as the moment of inertia J is changed so is the natural frequency. Now, in this system the distance of the balanced weights from the axis, and therefore the moment of inertia J, is the "parameter" which can be modulated periodically to cause progressively growing oscillations with a natural frequency of ω_0.

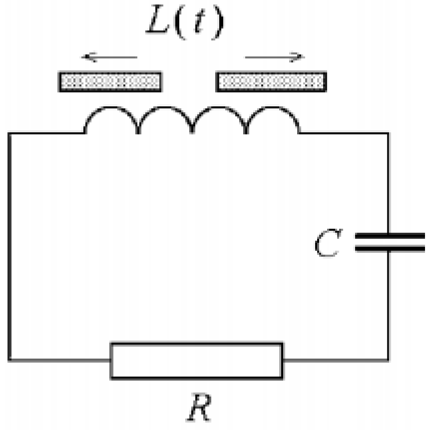

Figure 2.4 Analogous LCR-circuit with a coil whose inductance can be modulated

Building on this, parametric oscillators are also possible in electromagnetic circuits. For example, is a LCR circuit (Figure 2.4), oscillations can be induced by changing the capacitor by moving its two plates closer or away from each other or by changing the inductance by moving its core in and out of the coil.

2.4.3 Parametric Amplification in RF Circuits

The procedure of parametric amplification is best described in [14]. In a LC tank circuit, for a given plate spacing of the capacitor *C*, the tank will oscillate at its natural resonant frequency. At the voltage maxima during one of its oscillations, if we pull apart the plates on the capacitor or when the electrostatic force between the plates is maximum, we essentially do work against the electric field. If no dissipative losses are considered, this work is injected in the form of energy into the tank circuit and thus amplifies the amplitude of the oscillation. In a similar manner, at the voltage minima, the capacitor plates can be pushed together and since voltage is zero at this time, no work is done. This push and pull of the plates on the capacitor can be repeated twice every oscillation to continue amplification of the oscillating signal.

In practice, a separate oscillator provides a “pump” energy into the system. A RF input signal is amplified by a pump signal (Figure 2.5), nominally oscillating at twice the signal frequency. A typical variable capacitor is a varactor diode and an example of a variable inductor can be superconducting kinetic inductance transmission line (discussed later). The pump signal modulates the diode or the kinetic inductance causing it to produce negative reactance at the signal frequency.

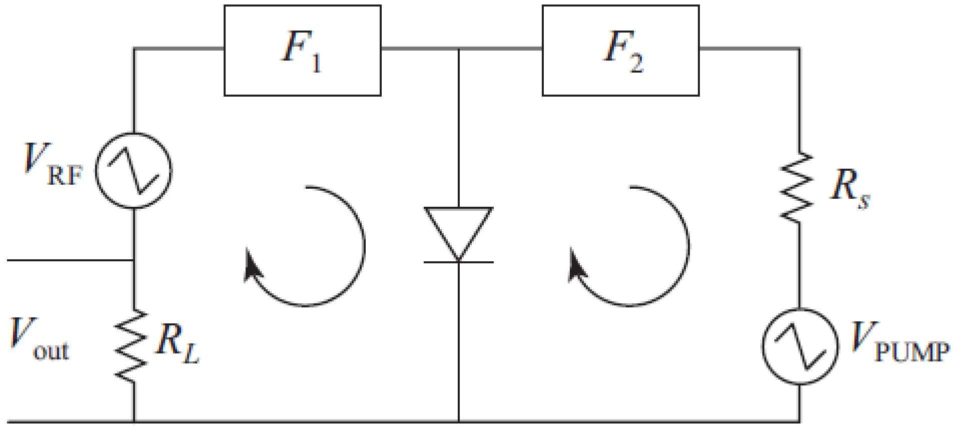

Figure 2.5 A simple Parametric Amplifier [13]

In RF circuits (and even in optical systems), parametric amplification can be achieved by pumping a nonlinear reactance with a large pump signal in order to achieve mixing of frequencies with gain or to achieve negative resistance in the circuit. Parametric amplifiers can be broadly classified into two distinct types: phase-incoherent up converting parametric amplifiers and negative-resistance parametric amplifiers. Phase-incoherent up converting parametric amplifiers employ a fixed incoherent incommensurate pump frequency f_p to mix with a small signal RF source frequency f_s and produce an output with a higher frequency and gain. Whereas in the negative resistance parametric amplifiers, the pump frequency lies in between the signal frequency f_s and $2f_s$ and the idler frequency is less than f_s. In a degenerate parametric amplifier case (which will be discussed later on), the idler frequency can also be equal to the signal frequency f_s and the pump is set at $2f_s$. But to understand the origins of the parametric amplification, we first need to look at the Manley-Rowe relations [15]

2.4.4 Manley-Rowe Power Relations

J.M. Manley and H.E. Rowe theorized and analysed the input and output flow of power in a nonlinear reactive element at its different frequencies. They concluded with an expression that quantifies how much of the total output power gets distributed among the harmonics. Following properties [16] of the Manley-Rowe relations give a general outline on how these relations can be put in context:

1] The Manley-Rowe relations are independent of the nature of the voltage-capacitance or voltage-inductance relations for a nonlinear reactance

2] Power of various driving sources does not affect the gain of the amplifier

3] Any external circuit in series or parallel to the nonlinear reactance does not affect the power distribution in the harmonic frequencies

Manley-Rowe relations for power distribution provide the metrics for ideal performance of nonlinear reactance mixers and amplifiers. An abridged version of the basic derivation of the Manley-Rowe relations will be discussed follows and later on equations dealing with a specific case applicable to four-wave degenerate mixing employed in this project will be discussed in details.

2.4.5 Deriving Manley-Rowe Relations

Although in the original paper Manley and Rowe state that their derivation would had also been possible with a nonlinear inductance, nonlinear capacitance is used to arrive at the harmonic frequency power relations.

Consider two voltage sources V_1 and V_2 at frequencies f_1 and f_2 respectively connected in parallel with a lossless voltage dependent nonlinear capacitance $C(V)$ (Figure 2.6)

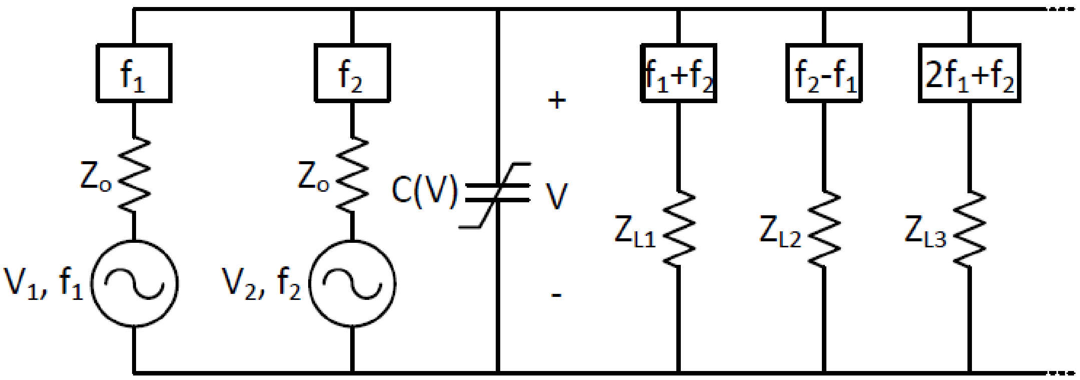

Figure 2.6 Circuit with a voltage dependent nonlinear capacitor $C(V)$ [17]

The two sources have Z_0 as their generator impedance. Bandpass filters are connected in each of the source branches with centering frequencies of f_1 and f_2 respectively. The bandpass filter is assumed to have an ideal frequency response passing only a single frequency and with an open circuit for out-of-band. An infinite number of resistive loads are connected across the nonlinear capacitor and with ideal bandpass filters in series of each one of the resistive loads. The passband frequency response of each of the bandpass filters is centred at a specific harmonic combination of the two driving frequencies f_1 and f_2. These harmonic frequencies are a result of nonlinear mixing in the nonlinear capacitance of f_1 and f_2. The only assumption made here is that f_1 and f_2 are incommensurate which means that the ratio of the two is not a whole integer and will always satisfy

$$\frac{\omega_1}{\omega_2} \notin Q \tag{2.6}$$

Considering the total charge q to be flowing in and out of the nonlinear capacitor. It can be expressed in the Fourier series as

$$q = \sum_{n=-\infty}^{\infty} \sum_{m=-\infty}^{\infty} q_{m,n} e^{j(m\omega_1 + n\omega_2)t} \tag{2.7}$$

where the series coefficients of charge, $q_{m,n}$ are expressed as

$$q_{m,n} = \frac{1}{4\pi^2} \int_{-\pi}^{\pi} \int_{-\pi}^{\pi} V.C(V) e^{-j(mx+ny)} dxdy \tag{2.8}$$

Where $x = \omega_1 t$ and $y = \omega_2 t$. Taking the time derivatives of the charge series coefficients, we can get the total current, $I_{m,n}$ through *C(V),*

$$I_{m,n} = \frac{dq_{m,n}}{dt} = \frac{\partial q_{m,n}}{\partial t} + \frac{\partial q_{m,n}}{\partial \omega_1} \frac{\partial \omega_1}{\partial t} + \frac{\partial q_{m,n}}{\partial \omega_2} \frac{\partial \omega_2}{\partial t} \tag{2.9}$$

But with the incommensurability of f_1 and f_2 *or* ω_1 and ω_2 we have $\frac{\partial q_{m,n}}{\partial \omega_1} = \frac{\partial q_{m,n}}{\partial \omega_2} = 0$ since there will be no time-average power due to interacting harmonics Therefore, the total current reduces to the partial time derivative of the charge series term

$$I = \frac{dq}{dt} = \sum_{n=-\infty}^{\infty} \sum_{m=-\infty}^{\infty} I_{m,n} e^{j(m\omega_1 + n\omega_2)t} \tag{2.10}$$

the individual harmonic current being

$$I_{m,n} = j(m\omega_1 + n\omega_2) q_{m,n}. \tag{2.11}$$

The voltage across the nonlinear capacitor can also be expressed as a two dimensional Fourier series,

$$V_{m,n} = \sum_{n=-\infty}^{\infty} \sum_{m=-\infty}^{\infty} V_{m,n} e^{j(m\omega_1 + n\omega_2)t} \tag{2.12}$$

where the series coefficients can be expressed as

$$V_{m,n} = \frac{1}{4\pi^2}\int_{-\pi}^{\pi}\int_{-\pi}^{\pi} V e^{-j(mx+ny)} dxdy \tag{2.13}$$

By combining the above equations to form the products of $I_{m,n}$ and $V_{m,n}$ to obtain the series coefficients for power $P_{m,n}$, we get

$$\begin{aligned} \sum_{n=-\infty}^{\infty}\sum_{m=-\infty}^{\infty} \frac{mV_{m,n}I_{m,n}^*}{mf_1 + nf_2} &= \sum_{n=-\infty}^{\infty}\sum_{m=-\infty}^{\infty} \frac{m2\Re\{V_{m,n}I_{m,n}^*\}}{mf_1 + nf_2} \\ &= \sum_{n=-\infty}^{\infty}\sum_{m=-\infty}^{\infty} \frac{mP_{m,n}}{mf_1 + nf_2} \end{aligned} \tag{2.14}$$

where $P_{m,n}$ are the power coefficients flowing in and out of the nonlinear capacitor at frequencies $nf_1 + mf_2$. The average power at the frequency $mf_1 + nf_2$ is given by the following

$$P_{m,n} = V_{m,n}I_{m,n}^* + V_{m,n}^*I_{m,n} = V_{m,n}I_{m,n}^* + V_{-m,-n}I_{-m,-n}^* = P_{-m,-n} \tag{2.15}$$

since,

$$\begin{aligned} &\left\{V_{m,n}e^{j(m\omega_1+n\omega_2)} + V_{-m,-n}e^{j(m\omega_1+n\omega_2)}\right\} \\ &\qquad \times \left\{I_{m,n}e^{j(m\omega_1+n\omega_2)} + I_{-m,-n}e^{-j(m\omega_1+n\omega_2)}\right\} \\ &\qquad = V_{m,n}I_{-m,-n} + V_{-m,-n}I_{m,n} = V_{m,n}I_{m,n}^* + V_{m,n}^*I_{m,n} \\ &\qquad = V_{m,n}I_{m,n}^* + V_{-m,-n}I_{m,n}^* \end{aligned} \tag{2.16}$$

But by conservation of energy, the power through a nonlinear reactance is

$$\sum_{m=-\infty}^{\infty}\sum_{n=-\infty}^{\infty} P_{m,n} = 0 \tag{2.17}$$

Multiplying each term of (2.16) by $(m\omega_1 + n\omega_2)/(m\omega_1 + n\omega_2)$ and then separating them, we can write the following equation

$$\omega_1 \sum_{n=-\infty}^{\infty} \sum_{m=-\infty}^{\infty} \frac{mP_{m,n}}{mf_1 + nf_2} + \omega_2 \sum_{n=-\infty}^{\infty} \sum_{m=-\infty}^{\infty} \frac{nP_{m,n}}{mf_1 + nf_2} = 0 \tag{2.18}$$

Now from (2.11) we have,

$$\frac{I_{m,n}}{mf_1 + nf_2} = jq_{m,n} \tag{2.19}$$

So from equations (2.11), (2.15), (2.16) and (2.19) we can write the following relation

$$\frac{P_{m,n}}{mf_1 + nf_2} = \frac{\left(V_{m,n}I^*_{m,n} + V_{-m,-n}I^*_{-m,-n}\right)}{mf_1 + nf_2} = \frac{V_{m,n}I^*_{m,n}}{mf_1 + nf_2} + \frac{V_{-m,-n}I_{m,n}}{mf_1 + nf_2} \tag{2.20}$$

or

$$\begin{aligned} \frac{mP_{m,n}}{mf_1 + nf_2} &= V_{m,n}\left(-jq^*_{m,n}\right) + V_{-m,-n}\left(jq_{m,n}\right) \\ &= -jV_{m,n}q^*_{m,n} + jV_{-m,-n}q^*_{-m,-n} \end{aligned} \tag{2.21}$$

Equation (2.21) implies that the factor $P_{m,n}/(mf_1 + nf_2)$ is independent of f_1 and f_2. So for any arbitrary selection of f_1 and f_2, we can always keep the circuit adjusted to C so that the resultant current keeps all the voltage amplitudes ($V_{m,n}$) unchanged. Since $q_{m,n}$ is a function of $V_{m,n}$, it will also remain unchanged. Therefore, even with arbitrary f_1 and f_2, the term $P_{m,n}/(mf_1 + nf_2)$, will remain unchanged. Therefore, to satisfy (2.18) we have,

$$\sum_{n=-\infty}^{\infty} \sum_{m=-\infty}^{\infty} \frac{mP_{m,n}}{mf_1 + nf_2} = 0 \tag{2.22}$$

and for the power flow with respect to the index *n*,

$$\sum_{n=-\infty}^{\infty} \sum_{m=-\infty}^{\infty} \frac{nP_{m,n}}{mf_1 + nf_2} = 0 \tag{2.23}$$

Ideal metrics for gain and stability and the parametric systems can be quantified by these Manley-Rowe relations. For example, consider voltage V_1 a small signal from one of the voltage generator and V_2 a large pump signal from the other voltage generator. Both the signals drive the nonlinear capacitance. The power flows in and out of the capacitor at a frequency $f_3 = f_1 + f_2$. The above power equations (2.22) and (2.23) then reduce to

$$\frac{P_1}{f_1} + \frac{P_3}{f_3} = 0 \tag{2.24}$$

$$\frac{P_2}{f_2} + \frac{P_3}{f_3} = 0 \tag{2.25}$$

Power flowing into the nonlinear capacitance can be considered as positive and the power flowing out of the nonlinear capacitor. Rearranging the terms in (2.16) and (2.17) we can get the following relation for the ratio of output power to the input power extracted at f_3

$$gain = \frac{f_3}{f_1} \tag{2.26}$$

This equation essentially gives the maximum gain possible of a parametric amplifier when up converting a signal of frequency f_1 to a frequency f_3. In the case when the parametric amplifier is down converting the input signal to a lower frequency, the Manley-Rowe relations give the maximum gain possible to be

$$gain = \frac{f_1}{f_3} \tag{2.27}$$

which is always less than one or in other terms is always at a loss.

In practical cases, the voltage generator on an average maintains a frequency of ω over a sufficiently long time but does not have a single frequency resonance. The frequency response is spread over a band of frequency, usually with ω having the highest response. The voltage the generated can be modelled as

$$V = V_0 e^{j(\omega t+\phi)} \tag{2.28}$$

where ϕ is an arbitrary phase that varies with time and has a zero mean value.

2.4.6 Negative Resistance Parametric Amplifiers

Figure 2.7 shows a negative resistance parametric amplifier in which a current flows at signal frequency f_s and with a pump frequency f_p and idler frequency $f_i = f_p - f_s$. The non-linear voltage dependent time varying capacitor can be defined as

$$C(t) = C_0\{1 + 2Mcos(\omega_p t)\} \tag{2.29}$$

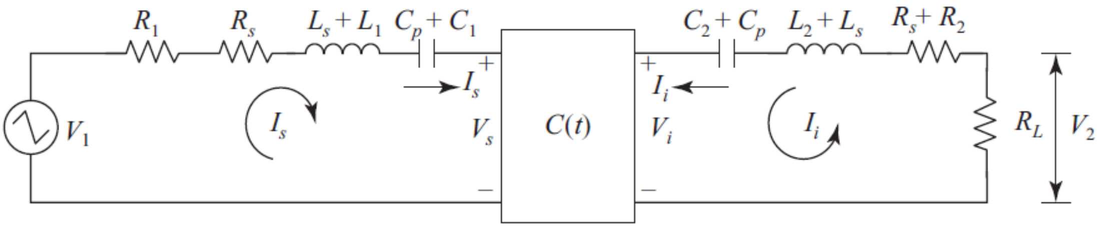

Figure 2.7 Equivalent circuit of a negative-resistance parametric amplifier [13]

The voltage

$$v_i = \frac{1}{2}\{V_i e^{j(\omega_p - \omega_s)t} - V_i^* e^{j(\omega_p - \omega_s)t}\} \tag{2.30}$$

and the idler current

$$i_i = \frac{1}{2}\{I_i e^{j(\omega_p - \omega_s)t} - I_i^* e^{-j(\omega_p - \omega_s)t}\} \tag{2.31}$$

then we can write,

$$\begin{bmatrix} I_i \\ I_i^* \end{bmatrix} = \begin{bmatrix} j\omega_i C_0 & j\omega_i C_0 M \\ -j\omega_s C_0 M & -j\omega_s C_0 \end{bmatrix} \begin{bmatrix} V_i \\ V_i^* \end{bmatrix} \tag{2.32}$$

and

$$\begin{bmatrix} V_i \\ V_i^* \end{bmatrix} = \frac{1}{1-M^2} \begin{bmatrix} \dfrac{1}{j\omega_i C_0} & \dfrac{M}{j\omega_s C_0} \\ -\dfrac{M}{j\omega_i C_0} & -\dfrac{1}{j\omega_s C_0} \end{bmatrix} \begin{bmatrix} I_i \\ I_i^* \end{bmatrix} \tag{2.33}$$

For the input and output circuits to the non-linear capacitor $C(t)$, we can write

$$\begin{aligned} V_1 = I_s[R_1 + R_s + j\omega_s(L_s + L_i) + \frac{1}{j\omega_s\big(C_p + C_i\big)} + \frac{1}{j\omega_s(1-M^2)C_0} \\ + \frac{MI_i^*}{j\omega_i(1-M^2)C_0} \end{aligned} \tag{2.34}$$

and

$$\begin{aligned} V_2 = I_i \Bigg[R_2 + R_s + j\omega_i(L_s + L_2) + \frac{1}{j\omega_i\big(C_p + C_2\big)} + \frac{1}{j\omega_i(1-M^2)C_0} \\ + \frac{MI_s^*}{j\omega_i(1-M^2)C_0}\Bigg] \end{aligned} \tag{2.35}$$

Using the tuning condition that,

$$\omega_s^2 = \frac{1}{L_s + L_1}\left[\frac{1}{C_p + C_1} + \frac{1}{(1-M^2)C_0}\right] \tag{2.36}$$

and

$$\omega_i^2 = \frac{1}{L_s + L_1}\left[\frac{1}{C_p + C_2} + \frac{1}{(1-M^2)C_0}\right] \tag{2.37}$$

in equations (2.34) & (2.35) we get the following expressions,

$$V_1 = (R_1 + R_s)I_s - \frac{jMI_i^*}{\omega_i(1-M^2)C_0} \tag{2.38}$$

and

$$V_2 = (R_2 + R_s)I_i - \frac{jMI_s^*}{\omega_s(1 - M^2)C_0} \tag{2.39}$$

Assuming $V_2 = 0$, we can solve (2.38) and (2.39) for I_i. Substituting this I_i in the expression of gain

$$G_0 = \frac{4R_iR_2|I_i|^2}{V_1^2} \tag{2.40}$$

and by simplifying the gain expression more, we get the following equation

$$G_0 = \frac{4R_1R_2\{\omega_iC_0R_n(1 - M^2)\}^2}{M^2(R_1 + R_s - R_n)^2} \tag{2.41}$$

where

$$R_n = \frac{M^2}{\omega_i\omega_s(R_2 + R_s)(1 - M^2)^2C_0^2} \tag{2.42}$$

The negative resistance R_n appears in the circuit because of the following. Frequency mixing occurs in the circuit due to application of pump power to the non-linear capacitance and the idler frequency is generated. When the current flows with this idler frequency, further mixing of pump and idler frequency occurs which generates f_s and harmonics of f_p and f_i. When the power generated through frequency mixing exceeds that of the supplied signal power at frequency f_s, the reactive element exhibits a negative resistance.

2.4.7 Non-linear Inductance

Derivations in previous sections evolve around non-linear capacitance as the reactive component. However, a non-linear inductance just as well can be the non-linear reactive element. The non-linear inductance can stem from either magnetic materials that exhibit nonlinear permeability with effects like saturation which makes the resulting inductance a function of the applied current or the non-linear inductance can also stem from kinetic inductance in in superconducting transmission lines as will be discussed in section 2.3.9. For now, we look at what the difference in equations will be in the case when a non-linear capacitance is replaced by a non-linear inductance.

Assuming a non-linear inductance for the non-linear reactance with a single valued relating between voltage V and the time rate of change of current, I. For voltage amplitudes $V_{m,n}$, the inductor generates a definite set of amplitudes I_{m_1,n_1}. So by conservation of energy implies the power $P_{m,n}$ to be

$$\sum_{m,n} W_{m,n} = 0 \tag{2.43}$$

or

$$\frac{1}{2}\sum_{m,n} V_{m,n} I_{m,n} \cos\phi_{m,n} = 0 \tag{2.44}$$

For the non-linear inductor case, the current $I_{m,n}$ is replaced by $I_{m,n}/\omega_{m,n}$ and differentiate with respect to ω_s.

$$-\frac{1}{2}\sum_{m,n} \frac{V_{m,n} I_{m,n}}{\left(m\omega_s + n\omega_p\right)^2} m \cos\phi_{m,n} = 0 \tag{2.45}$$

replacing $I_{m,n}/(m\omega_s + n\omega_p)$ by $I_{m,n}$ we will get back the Manley-Rowe relations exactly same as (2.22) and (2.23)

$$\sum_{n=-\infty}^{\infty} \sum_{m=-\infty}^{\infty} \frac{mP_{m,n}}{mf_1 + nf_2} = 0 \tag{2.46}$$

and

$$\sum_{n=-\infty}^{\infty}\sum_{m=-\infty}^{\infty}\frac{nP_{m,n}}{mf_1 + nf_2} = 0 \tag{2.47}$$

2.4.8 Four Wave Mixing and Phase Shift

The pump tone for the parameter amplifier design in this research is chosen such that

$$2\omega_p = \omega_s + \omega_i \tag{2.48}$$

where ω_p, ω_s and ω_i are the pump, signal and idler frequencies. Since the phase velocity of the wave is given by $v_{ph} = 1/\sqrt{L_{tot}C}$, and the total inductance consists the geometric as well as the kinetic inductance, the phase velocity varies with the length of the transmission line and the current being carried.

The gain produced by FWM between the three tones can be predicted by numerically integrating coupled mode equations over the length of transmission line, l:

$$\frac{dA_p}{dl} = \frac{Ik_p\alpha}{2I_*^2}\left[\left|A_p^2\right| + 2|A_s^2| + 2\left|A_i^2\right|\right]A_p + 2A_sA_iA_p^*e^{-i\Delta\beta l} \tag{2.49}$$

$$\frac{dA_s}{dl} = \frac{Ik_p\alpha}{2I_*^2}\left[|A_s^2| + 2\left|A_i^2\right| + 2\left|A_p^2\right|\right]A_s + A_i^*A_p^2e^{-i\Delta\beta l} \tag{2.50}$$

$$\frac{dA_i}{dl} = \frac{Ik_p\alpha}{2I_*^2}\left[\left|A_i^2\right| + 2|A_s^2| + 2\left|A_p^2\right|\right]A_i + A_s^*A_p^2e^{-i\Delta\beta l} \tag{2.51}$$

The integration is performed under the simplifying assumption that the pump remains un-depleted during the mixing process,

$$\frac{dA_p}{dl} = 0 \tag{2.52}$$

and that the idler current has zero amplitude at the beginning of the NLTL. Additional equations can be added to include the pump harmonic generation over the line length, but they are omitted here because of the un-depleted pump approximation. In actuality, these harmonics can be attenuated through the use of specific line geometries. In the absence of any applied DC or AC current, a superconducting transmission line can be modelled as a dispersion less line with propagation constant $\beta(\omega) = \omega/v_{ph}$ where v_{ph} is the phase velocity given by $v_{ph} = 1/\sqrt{L_{total}C}$. As a tone propagates along the transmission line, it experiences a phase shift $\Delta\phi = \omega l/v_{ph}$ equivalent to the electrical length of the line, in radians. In this case, the line dispersion,

$$\Delta\beta = \beta(\omega_s) + \beta(\omega_i) - 2\beta(\omega_p) = 0 \tag{2.53}$$

Once current is applied to the circuit, the phase velocity for a given tone acquires a current dependence such that

$$v_{ph}(I) = v_{ph_0}\left(1 - \alpha\frac{I^2}{2I_*^2}\right) \tag{2.54}$$

As a consequence, the tones experience a non-linear phase shift,

$$\Delta\phi = \frac{\phi}{2}\left(\frac{I}{I_*^2}\right) \tag{2.55}$$

which causes a phase mismatch between the pump, signal and idler tones. The signal gain predicted in this case is,

$$G_s = 1 + (\xi\Delta\phi(I)^2) \tag{2.56}$$

Since ξ_{crit} is known, $\Delta\phi(I)$ sets a limit on the maximum achievable signal gain, which translates into a requirement on the length of the NLTL. The phase slippage can be counteracted by engineering a dispersion into the line, which, at an optimal value of,

$$\Delta\beta = -\frac{2\Delta\phi}{l} = -\frac{\alpha k_p |A_P|^2}{2I_*^2} \tag{2.57}$$

accesses an exponential gain regime, where [17]

$$G_s = \frac{e^{2\xi\phi}}{4} \tag{2.58}$$

The dispersion engineering is dual purpose. In addition to cancelling the phase mismatch, it prevents shock front generation that occurs when $\Delta\phi \geq 1$ [17]. The dispersion engineering is accomplished by periodically widening the transmission line to decrease the impedance at the first few pump harmonic frequencies, ω_p, $2\omega_p$ and $3\omega_p$ [17]. The series of three widened sections are repeated over a pattern interval

$$l_{pat} = 2\omega_p v_{phi}/2 \tag{2.59}$$

with the separation between sections being $l_{pat}/3$ [18]. Figure 2.8 shows the results of numerically integrating the gain equations (2.50) – (2.52) for the case of a non-dispersion engineered NLTL at 90 GHz.

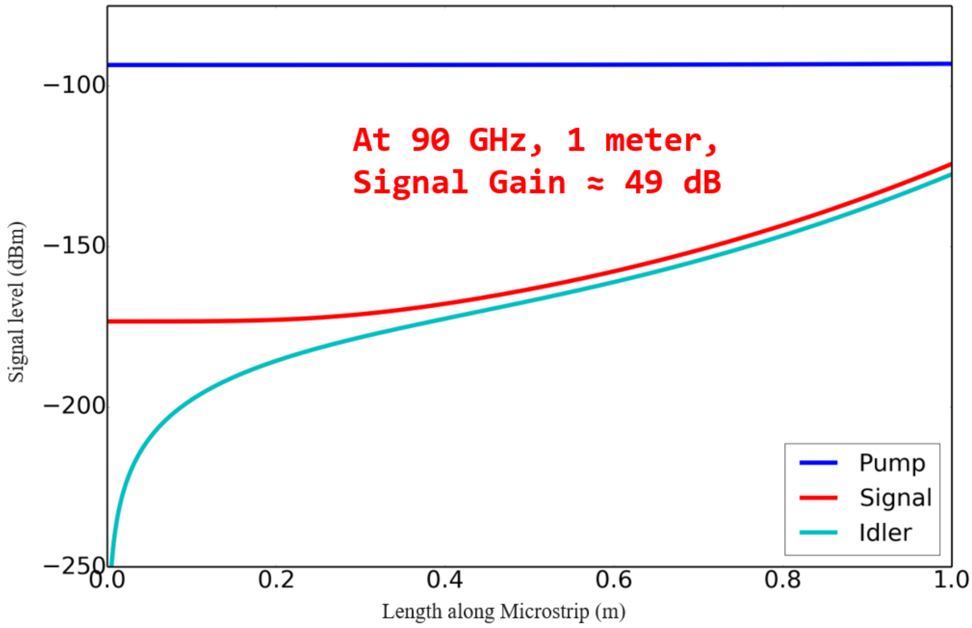

Figure 2.8 Pump, signal and idler signal levels with distance along the microstrip line

In the simulation, mixing was allowed to occur over a 3 m length of NbTiN NLTL. In this case, 34 dB of signal gain is produced. This value will increase if the periodic impedance structures are included in the simulation. Figure 2.9 shows signal and idler amplification as a function of line length, for the same geometry and circuit parameters used in Figure 2.8. The results shown in the figures are for $\omega_s \approx \omega_p = 90\ GHz$.

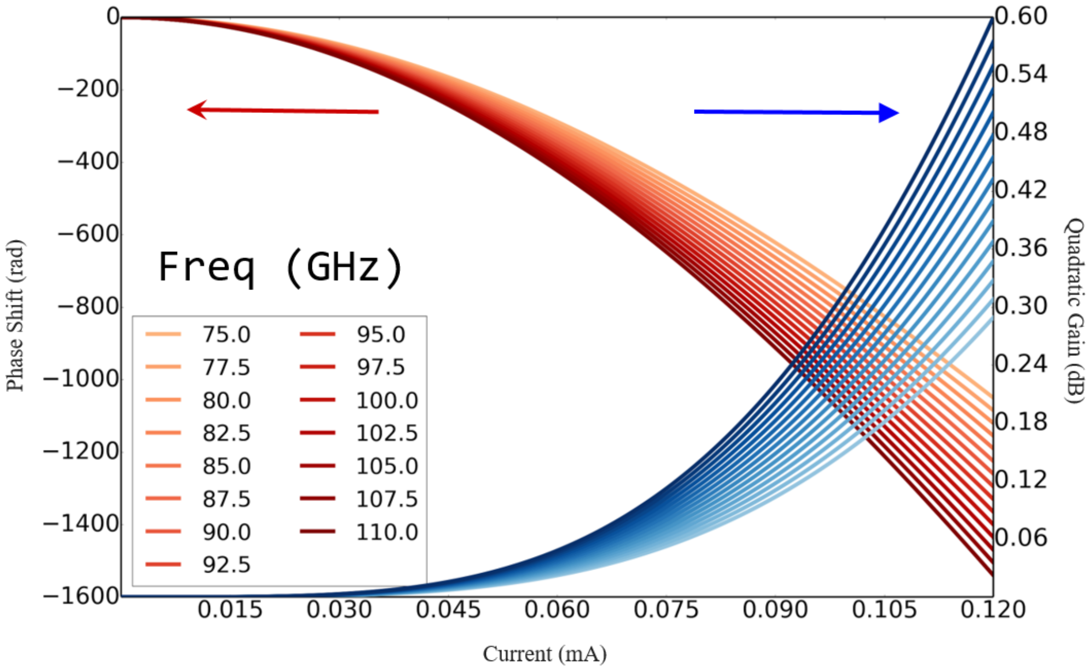

Figure 2.9 The simulated phase shift and quadratic gain of the parametric amplifier as a function of dc current.

2.4.9 Source of Kinetic Inductance

Bardeen-Cooper-Schrieffer (BCS) theory predicts that in a superconductor cooled to below its critical temperature, T_c. Cooper pairs are accelerated in the presence of a time varying electric field with frequency less than the band gap frequency,

$$f = \frac{2\Delta}{h} \tag{2.60}$$

where $\Delta = 1.76\, k_B T$ is the superconducting band gap. Their inertial opposition to the acceleration results in a phase delay between the applied and transmitted signals, which is modelled as an extra distributed 'kinetic' inductance added to the geometric inductance, for

$$L_{total} = L_k + L_{geo} \tag{2.61}$$

Equating the Cooper pairs' kinetic energy with an inductive energy yields,

$$\frac{1}{2}\, L_k I^2 = \frac{1}{2}\, (2m_e v^2)(n_{cp} l A) \tag{2.62}$$

where $2m_e$ is the mass of a Cooper pair, n_{cp} is the number density of pairs, l is the length of the transmission line, A is the cross sectional area of the line, and $I = 2n_{cp} e v A$ is the superconductor current. The intrinsic kinetic inductance [19] is then,

$$L_{k_0} = \left(\frac{m_e}{2n_{cp} e^2}\right)\left(\frac{l}{A}\right) \tag{2.63}$$

and is shown to be a function of the transmission line geometry. Mattis-Bardeen theory provides another expression for the intrinsic kinetic inductance,

$$L_{k0} = \frac{\bar{h}\rho_n}{\pi \Delta A} \tag{2.64}$$

where L_{k0} is the intrinsic kinetic inductance per unit length, and ρ_n is the normal state resistivity of the superconductor [20]. The ratio of the kinetic inductance to the total inductance, α will therefore be greater in materials with high normal state resistivity, and the superconducting film should be made as long and narrow as possible. For NbTiN, $\rho_n = 100$ µΩm, which is three orders of magnitude greater than typical resistivities for aluminium films [17]

2.5 Phase Shifter Design

Now that it is established in previous sections that to design an optimized W-band kinetic inductance parametric amplifier, an accurate measurement and characterization of phase shift $\Delta\phi_{max}$ as a function of pump power, signal and pump frequency and length of the transmission line, is crucially important and necessary. Also, since the phase shift $\Delta\phi_{max}$ increases as length of the transmission line, in order to perceive a measurable amount a transmission line of approximately 503mm is designed. The entire phase shifter design will consist of a microwave circuit with a feeding circular waveguide port and a waveguide to microstrip transition, four waveguide probes – two for each orthogonal polarization, an impedance matching transformer section on the microstrip, two ~503 mm transmission lines – one each at the two arms of same polarization, a terminating microstrip-to-waveguide transition (a replica of the waveguide-to-microstrip transition) and an output circular waveguide. The W-band signal will be fed into the circular waveguide with horn antennas attached to the waveguide through couplers. A directional coupler will be used before the feed horn to mix the signal and pump frequencies. The microwave circuit is packaged in a aluminium casing specially designed to accommodate the circular waveguide and the microwave circuit chip. A schematic of the various components of the entire phase shifter design is shown in Figure 2.10.

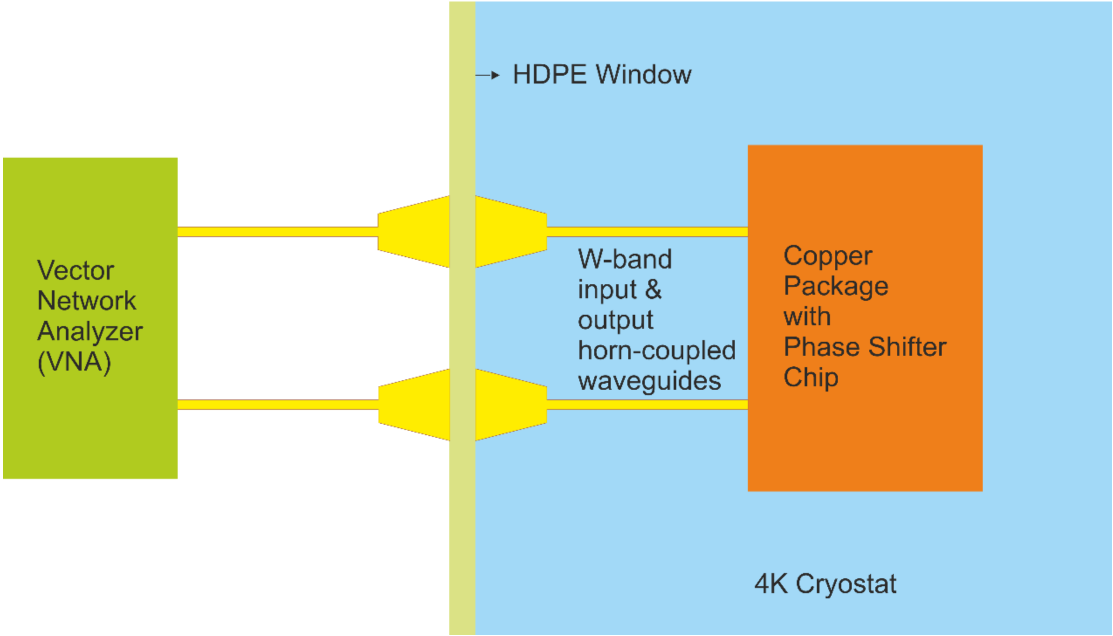

Figure 2.10 Schematic diagram of the entire phase shifter design

The design of all the above mentioned components are discussed in details in the following sub-sections.

2.5.1 W-band Circular Waveguide

Circular waveguide is a round metal pipe that supports TE and TM waveguide modes. The cylindrical components of the transverse field in a circular waveguide [21] are as follows:

$$E_\rho = -\frac{j}{k_C^2}\left(\beta\left(\frac{\partial E_z}{\partial \rho}\right) + \frac{\omega\mu}{\rho}\left(\frac{\partial H_z}{\partial \phi}\right)\right) \qquad (2.65)$$

$$E_\phi = -\frac{j}{k_C^2}\left(\frac{\beta}{\rho}\left(\frac{\partial E_z}{\partial \phi}\right) - \omega\mu\left(\frac{\partial H_z}{\partial \rho}\right)\right) \qquad (2.66)$$

$$H_\rho = \frac{j}{k_C^2}\left(\frac{\omega\epsilon}{\rho}\left(\frac{\partial E_z}{\partial\phi}\right) - \beta\left(\frac{\partial H_z}{\partial\rho}\right)\right) \tag{2.67}$$

$$H_\phi = -\frac{j}{k_C^2}\left(\omega\epsilon\left(\frac{\partial E_z}{\partial\rho}\right) + \frac{\beta}{\rho}\left(\frac{\partial H_z}{\partial\phi}\right)\right) \tag{2.68}$$

where $k_c^2 = k^2 - \beta^2$, and $e^{-j\beta z}$ propagation has been assumed. The transverse electric (TE) mode in a circular waveguide will be when $E_z = 0$ while the transverse magnetic mode (TM) will be for $H_z = 0$. The first TE mode to propagate is TE_{11} and for a TM wave it is the TM_{01}The dominant mode that can propagate in a circular waveguide is the TE_{11} mode since it has the lowest frequency of all the modes, TE or TM. The cut-off frequency for a TE_{11} [21] mode of a circular waveguide is given by

$$f_c = \frac{1.841}{2\pi a\sqrt{\mu\epsilon}} \tag{2.69}$$

where a is the radius of the circular waveguide.

Figure 2.11. shows the attenuation due to conductor loss versus frequency for various modes of a circular waveguide [21].

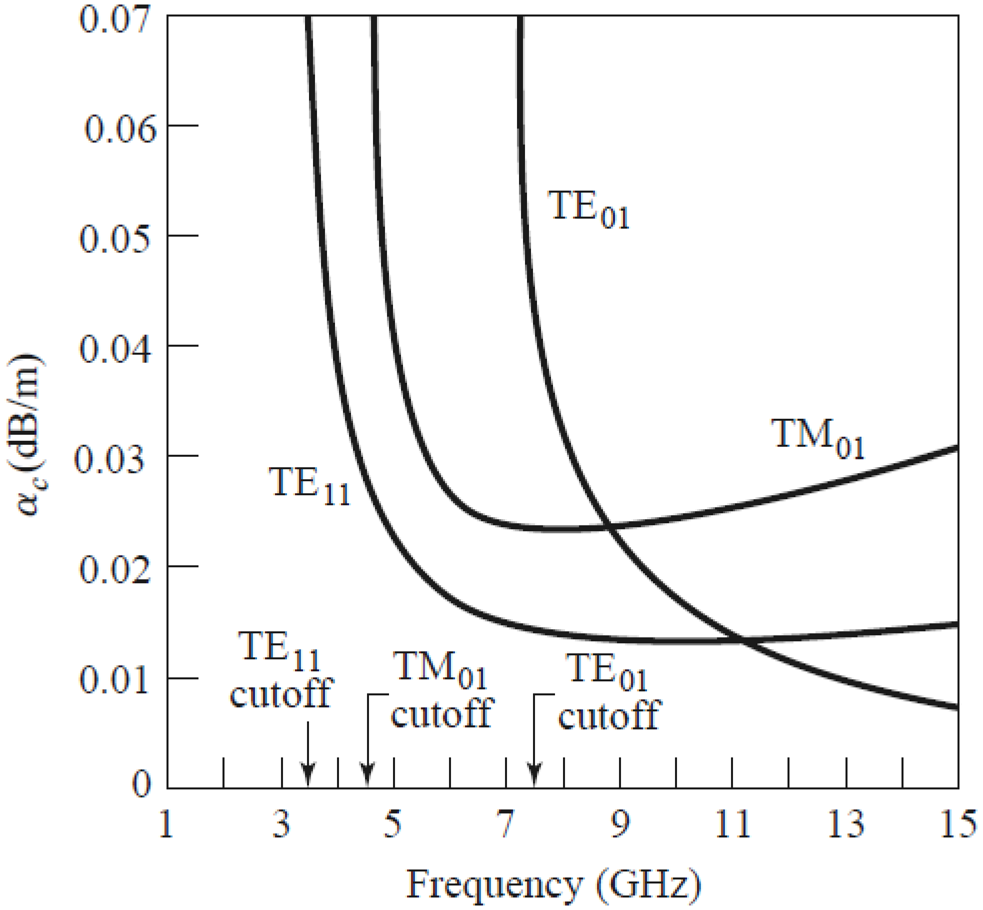

Figure 2.11 Attenuation of various modes in a circular waveguide with radius $a = 2.54\ cm$ [21]

Figure 2.12 shows the cut-off frequencies of a few TE and TM modes of a circular waveguide normalized to the dominant TE_{11} mode frequency [21].

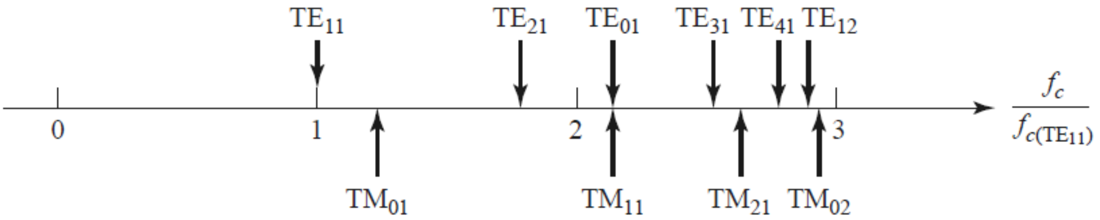

Figure 2.12 Cut-off frequencies of the first few TE and TM modes of a circular waveguide relative to the cut-off frequency of the dominant TE_{11} mode [21].

Figure 2.13 shows field lines of some TE and TM modes of a circular waveguide. A circular waveguide-to-microstrip transition aims at transforming the field lines of the dominant TE_{11} mode to the quasi-TEM mode of a microstrip (discussed in the next sub-section).

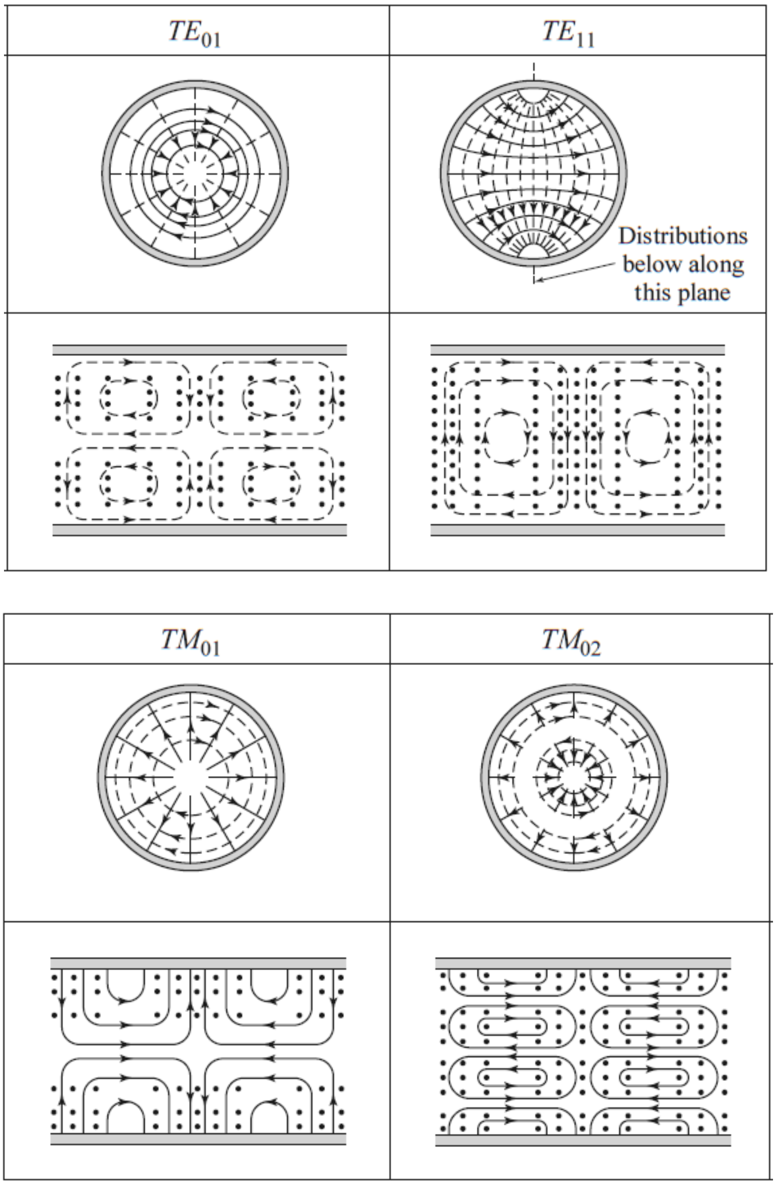

Figure 2.13 Circular and along the waveguide field distributions of different TE and TM modes in a circular waveguide [21].

So according to equation (2.70) for a W-band (75 GHz to 115 GHz) circular waveguide, the radius used in the phase shifter design is 1.42 cm. To calibrate the phase shift in the phase shifter, we operate the circular waveguide with two polarizations orthogonal to each other one at a time.

2.5.2 Microstrip Transmission modes

A microstrip line consists of a conductor of width W on a athin, grounded dielectric substrate of thickness d and relative permittivty ϵ_r as shown in Figure 2.14.

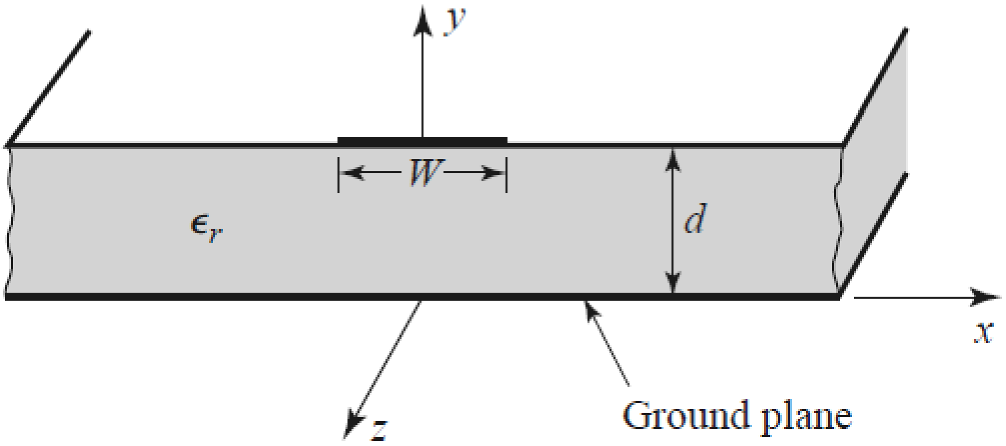

Figure 2.14 Microstrip line on a dielectric substrate of permittivity ϵ_r

If the dielectric permittivity was 1 i.e. $\epsilon_r = 1$, the conductor would be embedded in a homogeneous medium which would be able to carry a pure TEM transmission line with phase velocity $v_p = c$ and propagation constant $\beta = k_0$. However, in a practical case, the conductor lies on a dielectric substrate with non-unity permittivity and since dielectric does not fill the region above the strip, the field lines are now not contained entirely in the dielectric region between the conductor and the substrate as shown in Figure 2.15. For this reason, the microstrip line cannot support a pure TEM wave

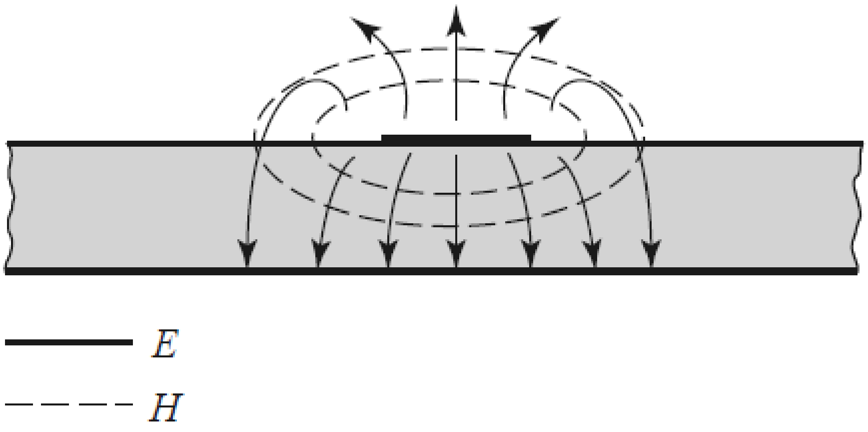

Figure 2.15 Field lines in both the dielectric substrate and in air in a microstrip line

In actuality, the fields of a microstrip line constitute a hybrid $TM-TE$ wave or $quasi-TEM$ mode. The phase velocity and the propagation constant of microstrip is then given by

$$v_p = \frac{c}{\sqrt{\epsilon_{eff}}} \tag{2.70}$$

$$\beta = k_0\sqrt{\epsilon_{eff}} \tag{2.71}$$

where ϵ_{eff} is the effective dielectric constant since some of the field lines are in the dielectric region and some are in air. The effective dielectric constant satisfies the relation

$$1 < \epsilon_{eff} < \epsilon_r \tag{2.72}$$

and depends on the substrate dielectric constant, substrate thickness and the conductor width and the frequency. The empirical formula for the effective dielectric constant is given by

$$\epsilon_{eff} = \frac{(\epsilon_r + 1)}{2} + \frac{\epsilon_r - 1}{2} - \frac{1}{\sqrt{1 + \frac{12d}{W}}} \tag{2.73}$$

In the phase shifter design, the dielectric is a silicon-on-insulator substrate with thickness of ~332 μm etched to 30 μm and a relative permittivity of $\epsilon_r = 11.7$ and with a 3 μm microstrip line deposited with a thickness of ~200 nm of niobium titanium nitride (NbTiN) for reasons made clear in previous sections. Two pairs of two of such microstrip lines are designed for the phase shifter circuit with each pair for a single polarization of the wave guided TE_{11} mode of W-band signal.

2.5.4 Circular Waveguide to Microstrip transition

Microwave transitions are used to launch microwave power from one kind of transmission line to another with minimum possible reflective and dissipative losses. Desirable characteristics of a transition [19] are:

a) Low transmission and reflective losses over the operating bandwidth.

b) Ease of connection and dis-connection to a microstrip with reproducibility.

c) In-line design, robustness and simple fabrication.

d) Adaptability to different substrate dielectric thicknesses.

The mechanical design should be appropriate to physically match both electrical and magnetic field distributions between the two media as close as possible to keep the discontinuity reactance small. The electrical design should also be optimized to match the impedances and minimize interface discontinuities and avoid losses over the operating bandwidth. In general, electric and magnetic fields are matched by shaping the structure of the transition while impedance matching and discontinuity reactance compensation is realized by $\lambda/4$ transformers.

In any microwave transition, minimizing the interface discontinuity reactances is preferred over compensating for the discontinuities which limits the frequency range. This is done by matching both the electric and magnetic field patterns of the two media at the interface. An example of the field pattern transformation from a co-axial waveguide to a microstrip transition is shown in Figure 2.16

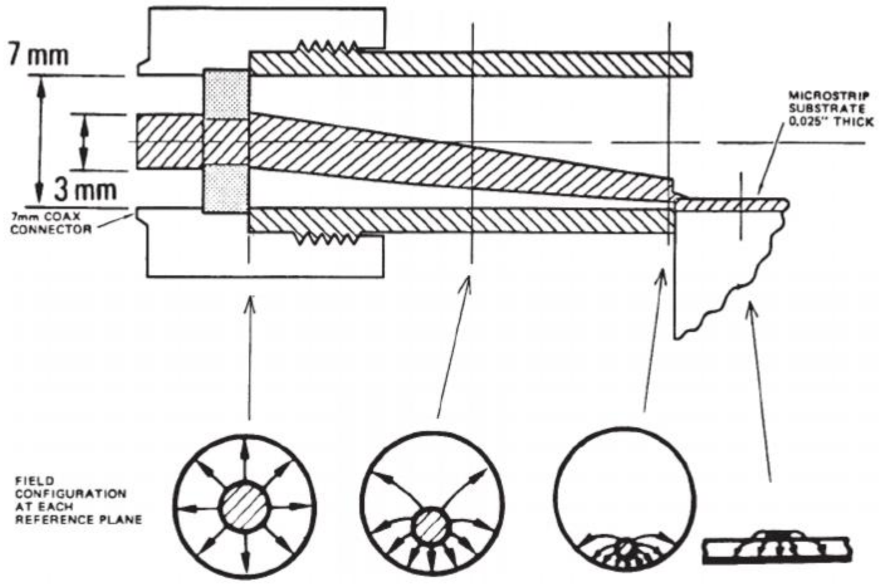

Figure 2.16 Coaxial-to-microstrip transition field configuration [22]

Another example of a ridged waveguide to microstrip transition with electric field configurations is shown in Figure 2.17

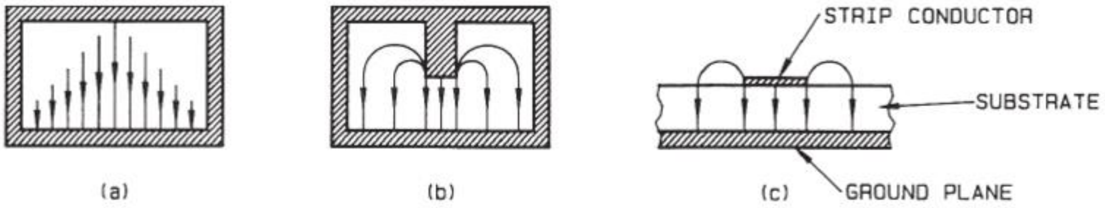

Figure 2.17 Ridged waveguide-to-microstrip transition electric field configuration [22].

The circular waveguide-to-microstrip transition will also be similar to the one shown in Figure 2.16 except the waveguide and the microstrip are orthogonal to each other. Waveguide to microstrip transition have been dealt with in the literature in early days [20], [21] & [22]. The transition is basically done using a microstrip "probe" which essentially matches the waveguide impedance to the microstrip impedance. The probe is a rectangular patch/patches whose length and width are tuned to minimize the reflections and maximize the transmission. The probe used in the phase shifter's design is of the type shown in Figure 2.18 [24] where it is inserted in the transverse cross-section of the circular waveguide through an aperture in the waveguide wall. A short or a "back-short" is also placed at an optimum location from the microstrip probe to couple maximum energy from the TE_{11} mode of the waveguide to the $quasi - TEM$ mode of the microstrip line. The back-short serves to reflect any wave propagating in the wrong way and back towards the probe where it combines in phase with the incident wave. Although theoretically the back-short should be placed at $\lambda/4$ distance from the microstrip probe, in reality it is slightly adjusted to minimize the return losses.

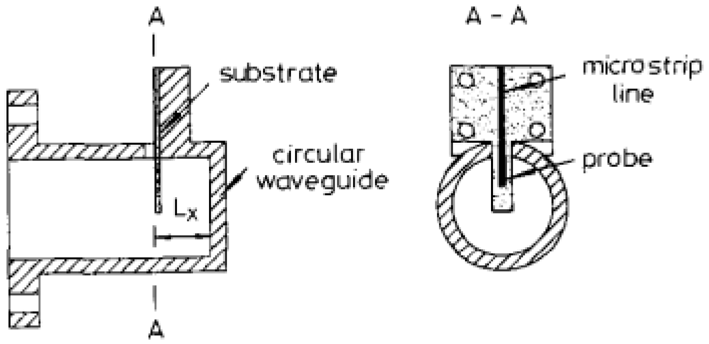

Figure 2.18 Circular waveguide-to-microstrip transition [24]

The circular waveguide-to-microstrip arrangement used in design of the phase shifter is shown in Figure 2.19. The entire microwave circuit consists of a W-band circular waveguide of radius 1.42 mm, a silicon substrate of ~30 μm thickness with a permittivity of $\epsilon_r = 11.7$, two pairs of two (in total four) waveguide-to-microstrip transitions – two for each polarization, impedance transformer to convert from a 100 µm line down to 3 µm, two 3µm wide and ~503 mm long microstrip lines on the same polarization arm and two 3 µm wide and ~23.8 mm long for the other polarization. The dual polarization waveguide-to-microstrip transition and circular waveguide are replicated on the output port as well. The waveguide-to-microstrip transition or the microstrip "probe", also involves a back-short along the circular waveguide but on the opposite side of the substrate wafer. A circular choke flange around the waveguide, to filter out the propagation of unwanted microstrip modes is also included in the circuit design.

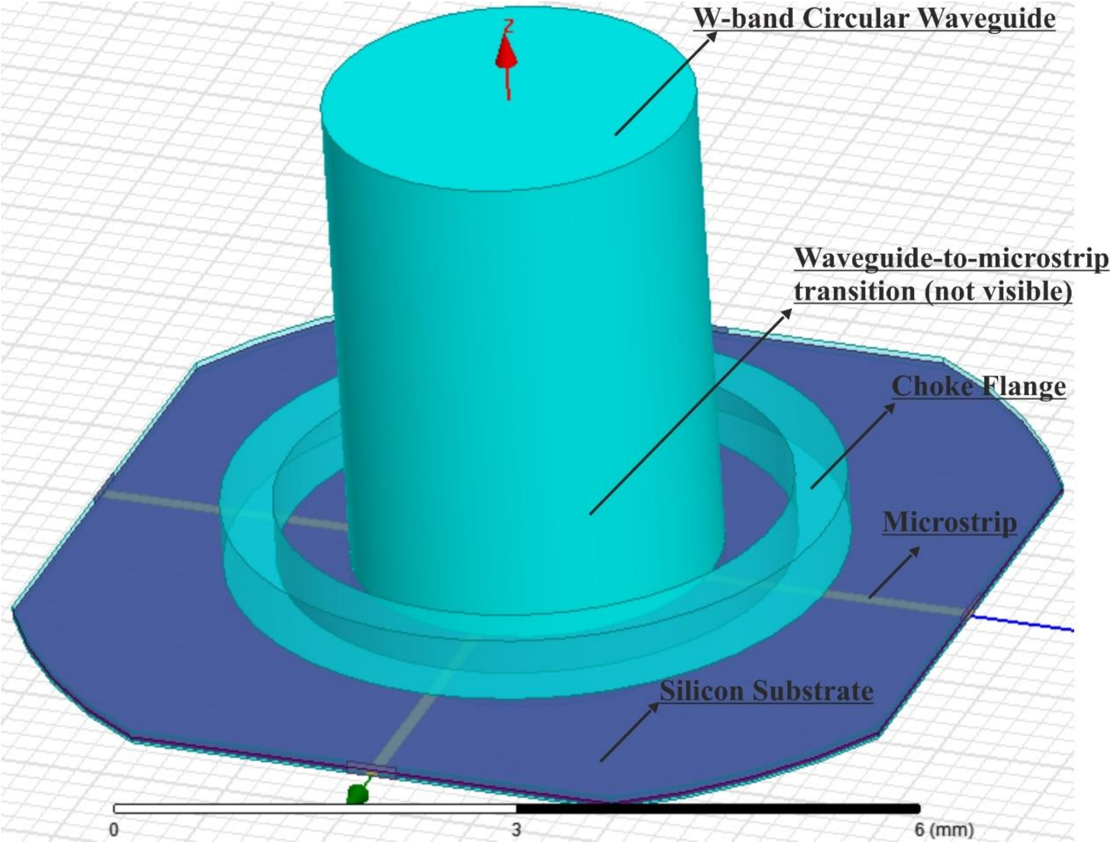

Figure 2.19 The W-band circular waveguide-to-microstrip transition design

2.6 Simulations and Design Optimization

Electromagnetic simulations were done in order to optimize the circular waveguide-to-microstrip transition. Ansys High Frequency Structural Simulator (HFSS) EM software was used to simulate the W-band transition design. An open source HFSS-Matlab API [23] which controls the input fields of HFSS was used to run and save various circuit design parameter optimizations. For simulation purposes only one waveguide-to-microstrip transition is simulated since the symmetry of input and output waveguides will ensure same wavguide-to-microstrip and microstrip-to-waveguide transition. Following sub-sections will elucidate on various aspects of the simulation.

2.6.1 Structure

A cross-section of the complete waveguide-to-microstrip transition circuit is shown in Figure 2.20.

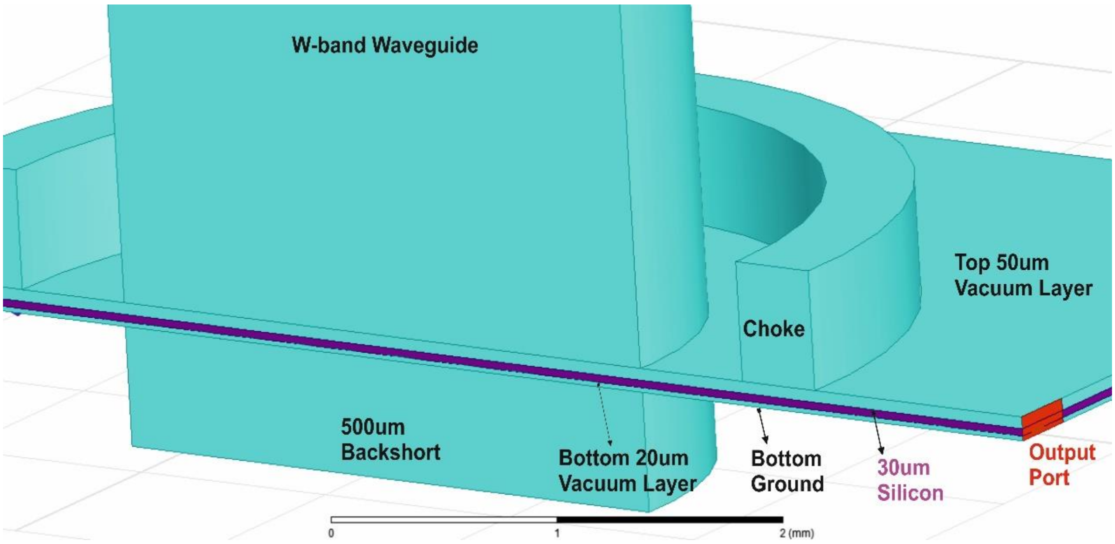

Figure 2.20 Cross-section of waveguide-to-micrsotrip transition circuit.

The W-band circular waveguide has a radius of 1.42 cm and is terminated on the input end with a “wave port”. The W-band signal is launched in the negative z direction from this wave port which travels down the W-band waveguide. The wave port is configured for two orthogonal polarizations as shown in Figure 2.21. The default boundary conditions in HFSS for a structure part are perfect electric boundaries and therefore the side walls of the W-band waveguide are terminated appropriately.

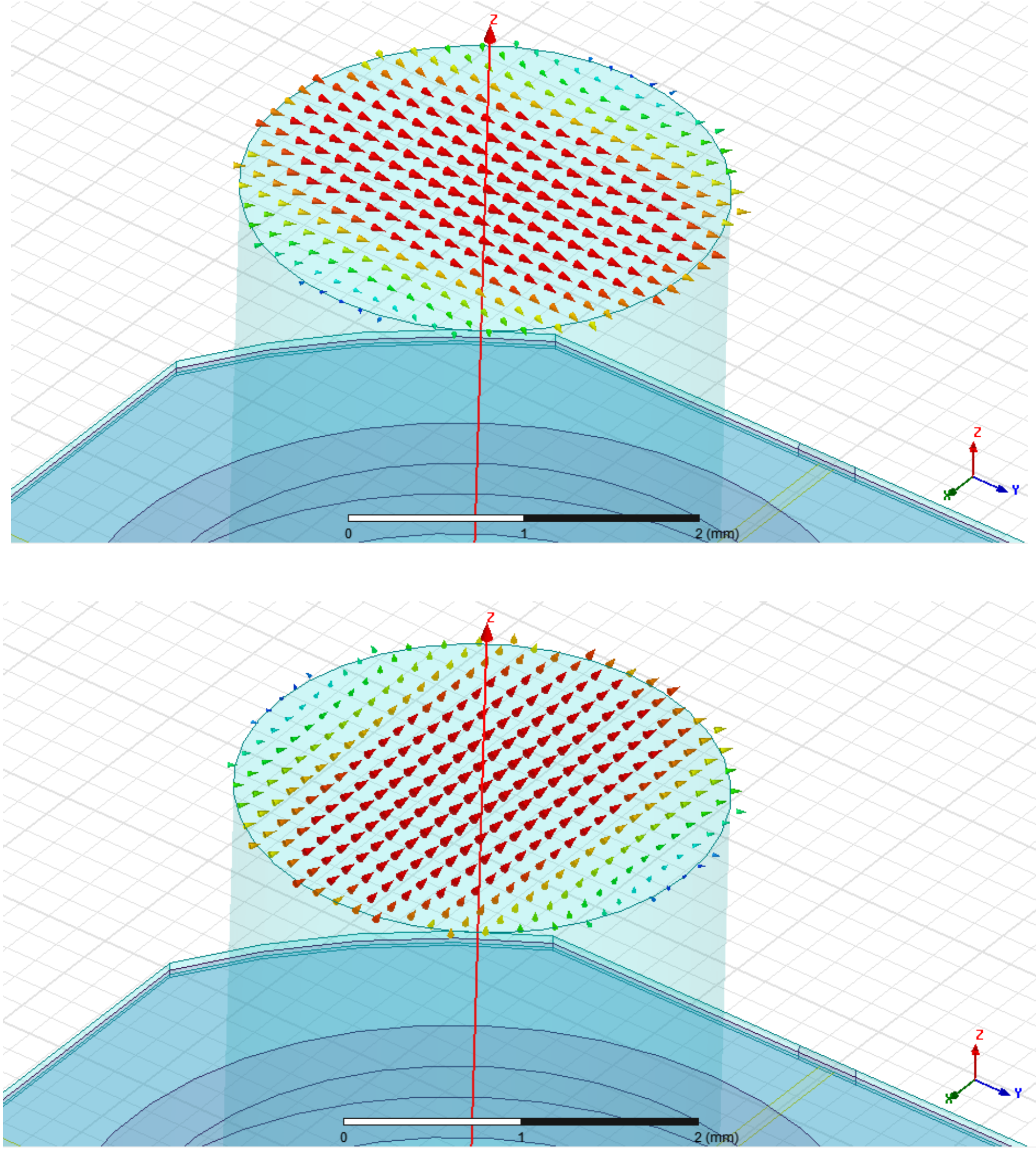

Figure 2.21 Two orthogonal polarization modes of the input “wave port”

The port at which the transmission through the waveguide-to-microstrip transition is measured is another wave port that covers the entire cross-section at the end of the microstrip which includes the silicon substrate, the vacuum gap above the silicon substrate, vacuum gap below the silicon substrate and the microstrip line itself, as shown in Figure 2.22. There are four such output wave ports that measure the transmission at the end of each microstrip line. Each of the two orthogonal polarizations launched at the input wave port atop the W-band waveguide are detected at one of the two pairs of two output wave ports.

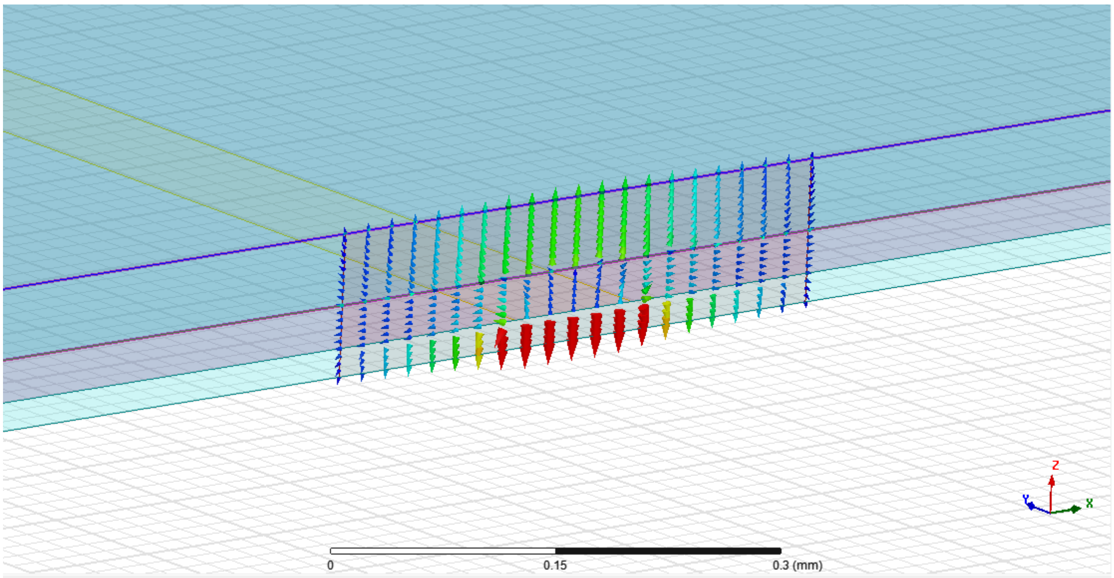

Figure 2.22 Output wave port at the end of a microstrip line that spans over the entire cross-section of the circuit at that point.

The microstrip on the chip is directly above the back-short plate separated by a 20 µm vacuum layer. The metal work is intentionally placed directly above the back-short plate so that the incoming electromagnetic wave from the input wave port sees the silicon first and then the microstrip probe and impedance matching sections after that. This is done for better coupling of the electromagnetic energy from the waveguide as well as the back-short. A vacuum gap of 50 μm separates the waveguide plate from the silicon substrate.

2.6.2 Impedance Boundary Conditions

The entire waveguide-to-microstrip transition circuit consists of different boundary conditions with different impedances. All the vacuum and air boundaries are terminated with an impedance of 377 Ω. All silicon interface boundary impedances are terminated by 110 Ω. Since the microstrip will be of NbTiN, which will be superconducting at 1.2 K will have zero resistance and as calculated previous, a kinetic inductance L_k of 5.7pH/square, the microstrip is assigned an impedance sheet with reactance of $2\pi\omega L_k. \Omega/\mathrm{square}$.

2.6.3 Waveguide-to-Microstrip Transition Design Optimization

Waveguide-to-microstrip transition consists of a microstrip probe which intercepts the *TE* mode wave launched in the circular waveguide and captures the electromagnetic energy to convert it into a *quasi-TEM* wave that is supported by the microstrip. Here, we have four of these microstrip probes arranged at the beginning two orthogonal pairs of two parallel but opposite running microstrip lines as shown in Figure 2.23.

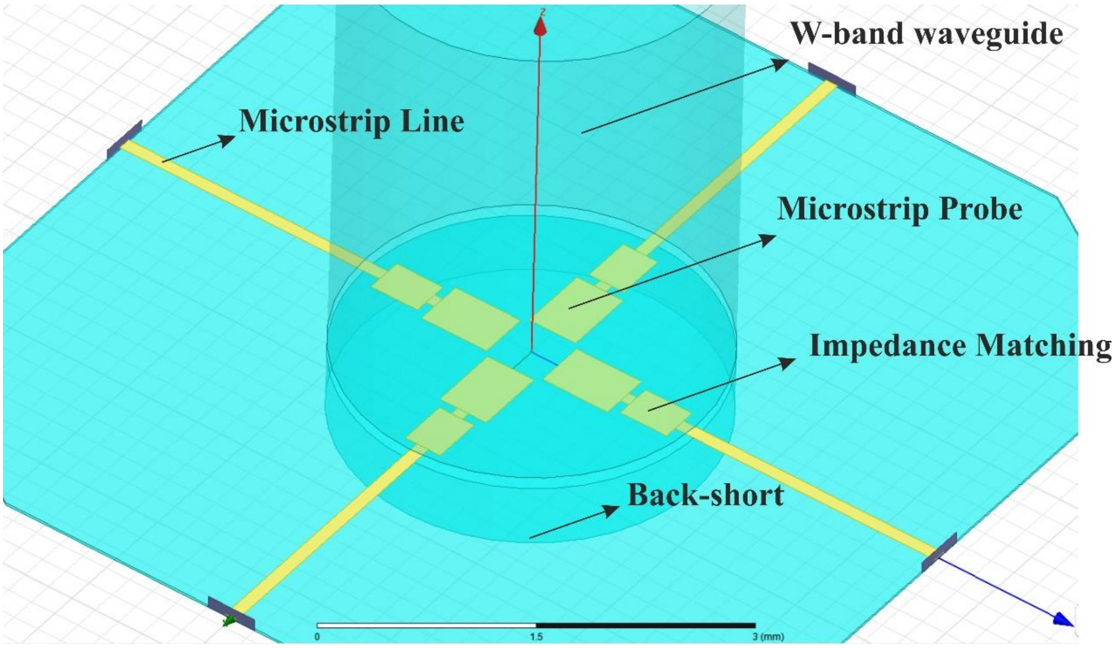

Figure 2.23 Microstrip probe design

The microstrip probes are followed by an impedance matching section which matches the input waveguide impedance to the impedance of the microstrip. Since the microstrip is a NbTiN superconducting metal, it is designed to not have any distributed resistance. However, because of the kinetic inductance distributed over the entire length of the microstrip line, the impedance matching has to be done for a reactance of

$$X_L = 2\pi\omega L_k \tag{2.74}$$

where L_k is 5.7pH/square and ω is the operating frequency. The impedance then becomes

$$Z = 0 + 2\pi\omega L_k \tag{2.75}$$

which is frequency dependent. Therefore, the impedance matching should be as much broadband as possible. Microstrip probe and impedance transformer design is well elaborated in [24]. The impedance matching section consists of a high inductive line placed in series with the probe to resonate out its capacitive reactance. This is followed by a quarter-wave impedance transformer to match the impedance of the circular waveguide to the microstrip line (Figure 2.24).

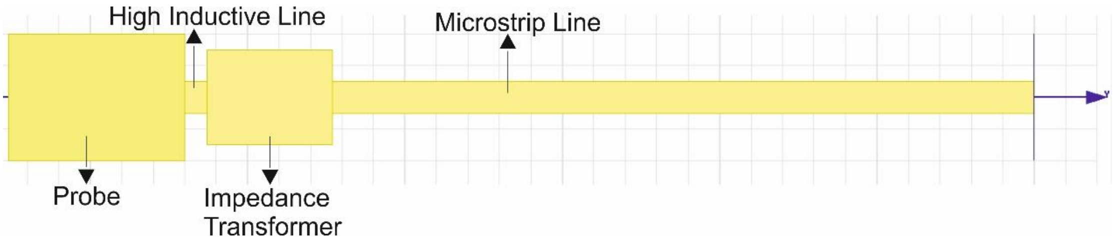

Figure 2.24 Microstrip probe, high inductive line and impedance transformer components of the transition.

The length and widths of the probe, high inductive line and impedance transformer (Figure 2.25) were optimized over various optimization runs which were aimed at maximizing the transmission (S21), minimizing the reflection (S11) and maximizing the absorption efficiency given by (2.77), over the 75GHz to 115GHz bandwidth.

$$Absorbtion\ Efficiency = 1 - (S11)^2 - (S21)^2 \qquad (2.76)$$

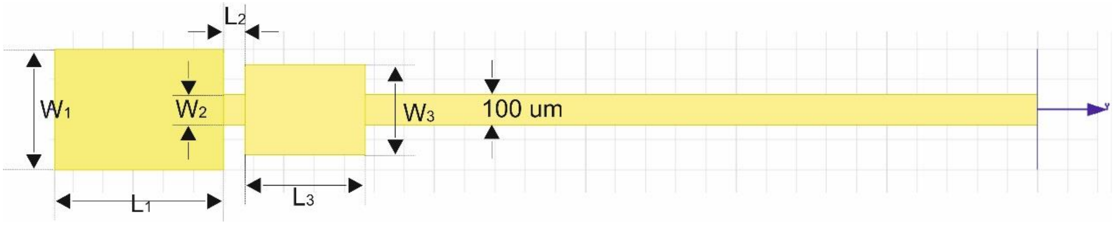

Figure 2.25 Lengths and widths of the probe, high inductive line and impedance transformer components.

A few of the optimization runs of L_1, W_1, L_2, W_2, L_3 & W_3 are shown in the following figures.

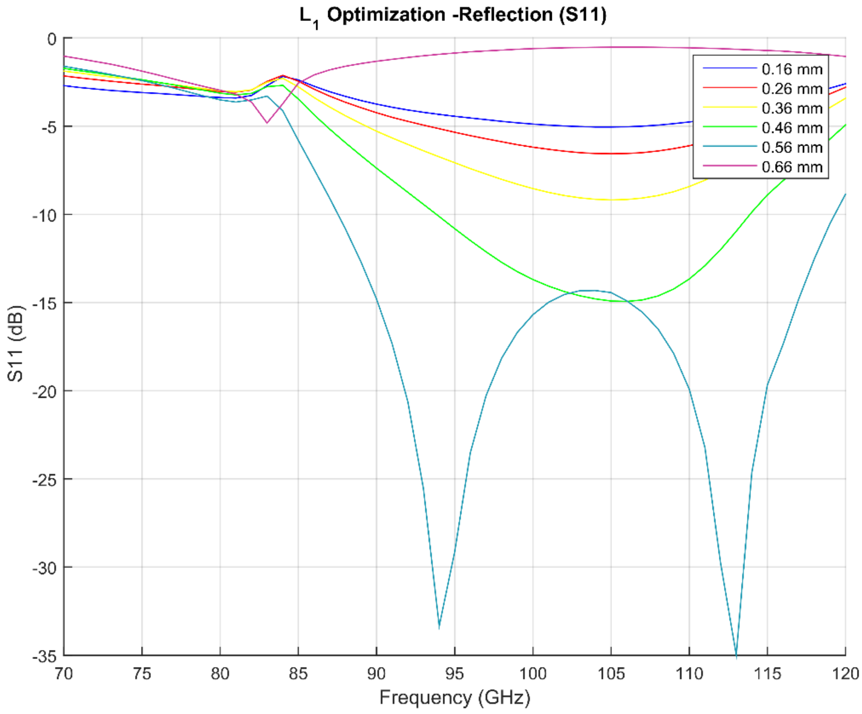

Figure 2.26 Reflection characteristics (S11) of L_1 optimization runs

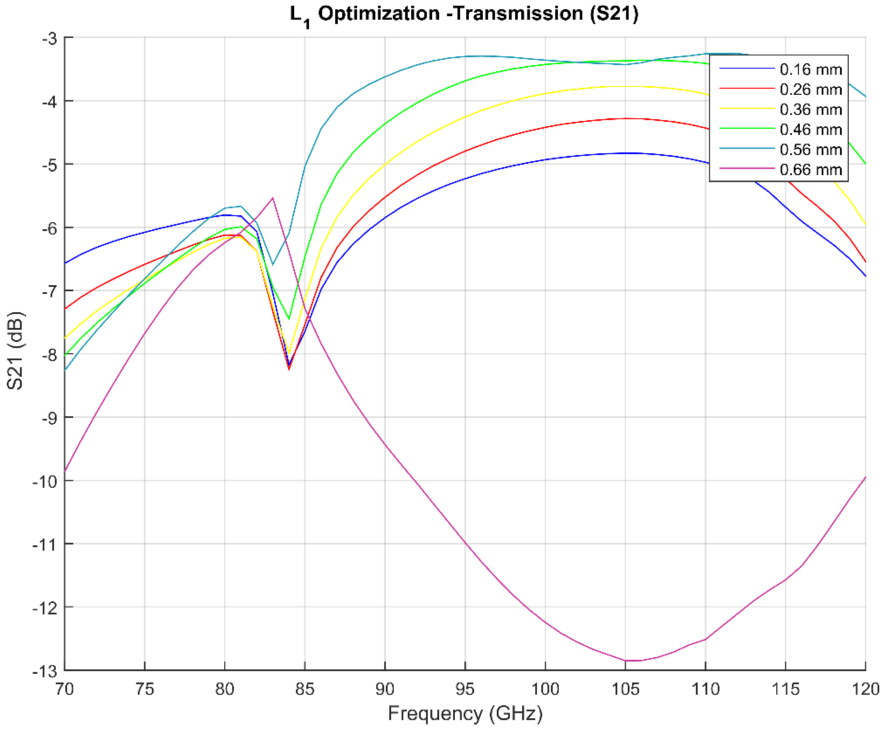

Figure 2.27 Transmission characteristics (S21) of L_1 optimization runs

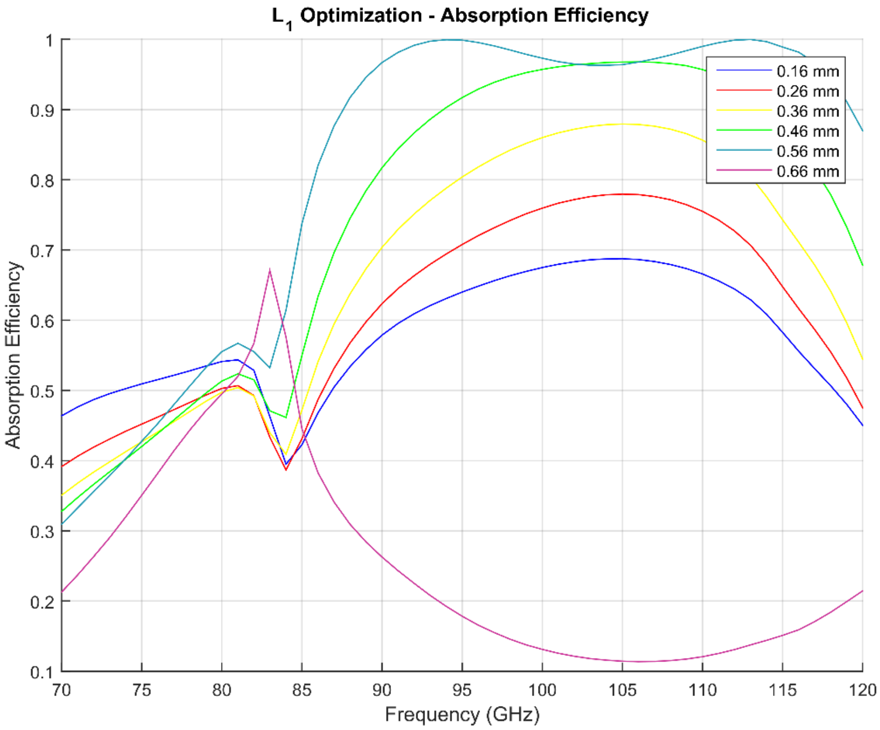

Figure 2.28 Absorption Efficiency of L_1 optimization runs

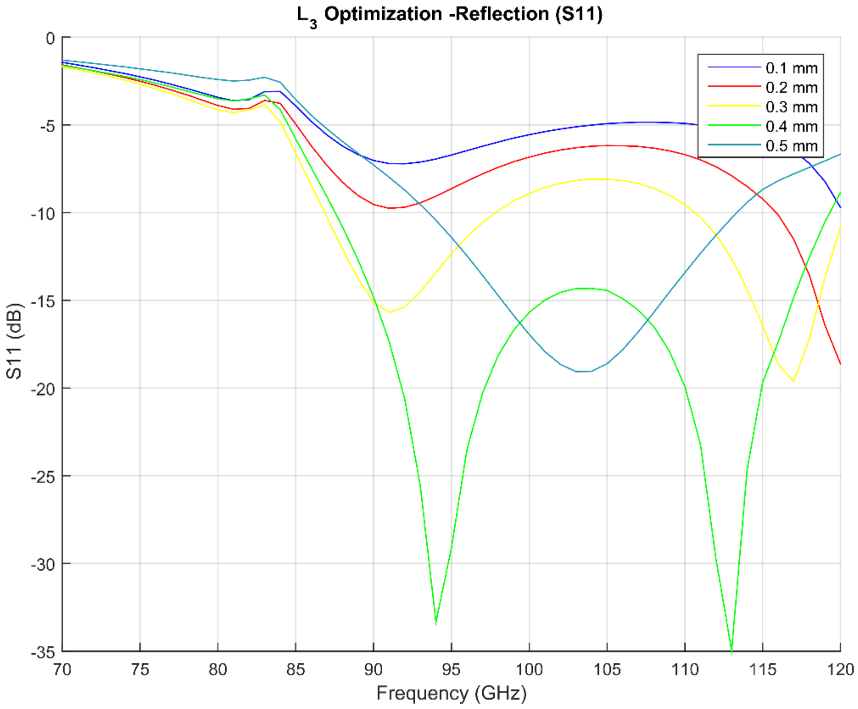

Figure 2.29 Reflection characteristics (S11) of L_3 optimization runs

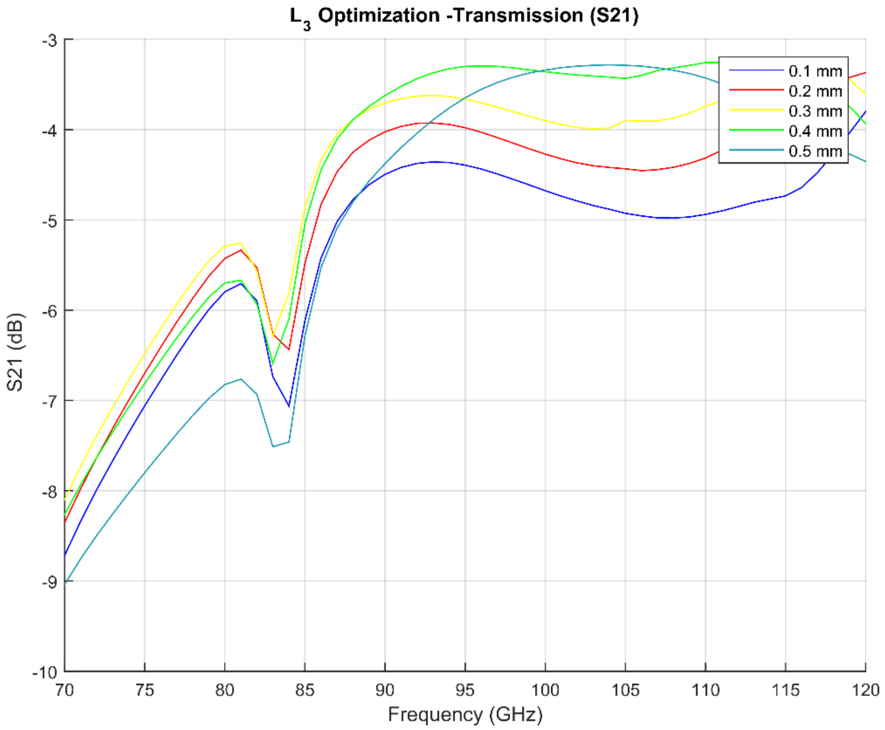

Figure 2.30 Transmission characteristics (S21) of L_3 optimization runs

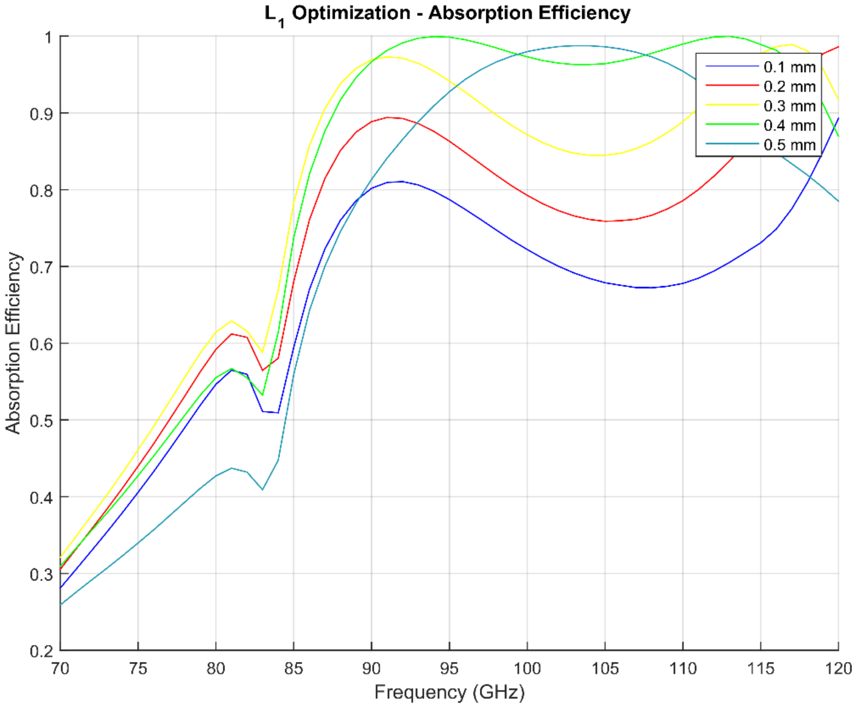

Figure 2.31 Absorption Efficiency of L_3 optimization runs

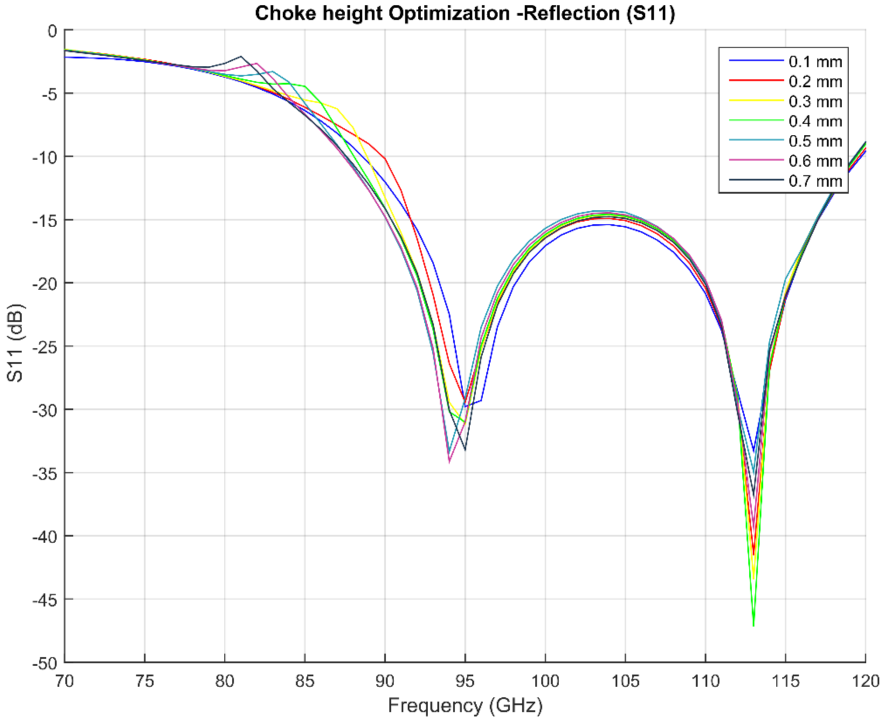

Figure 2.32 Reflection characteristics (S11) of choke height optimization runs

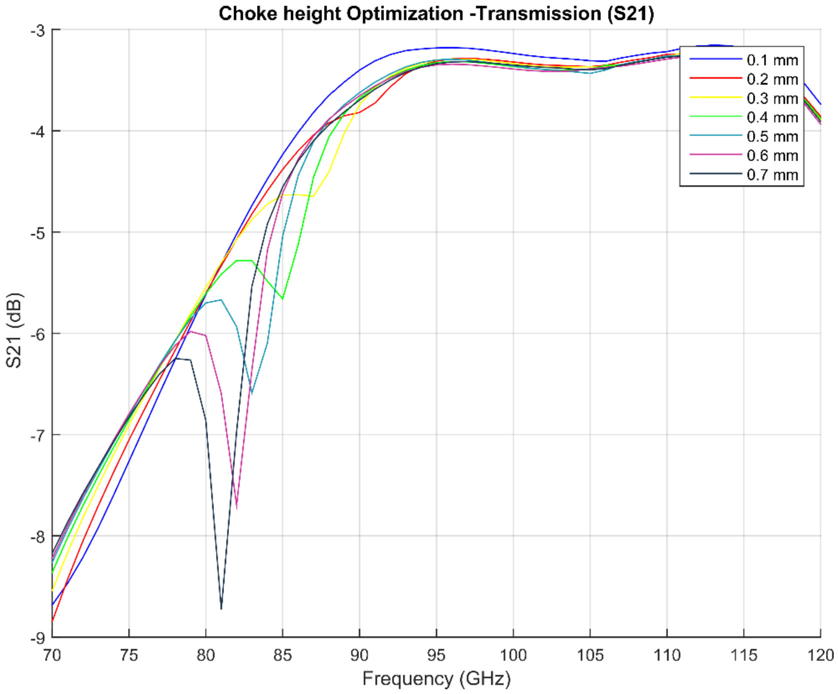

Figure 2.33 Transmission characteristics (S21) of choke height optimization runs

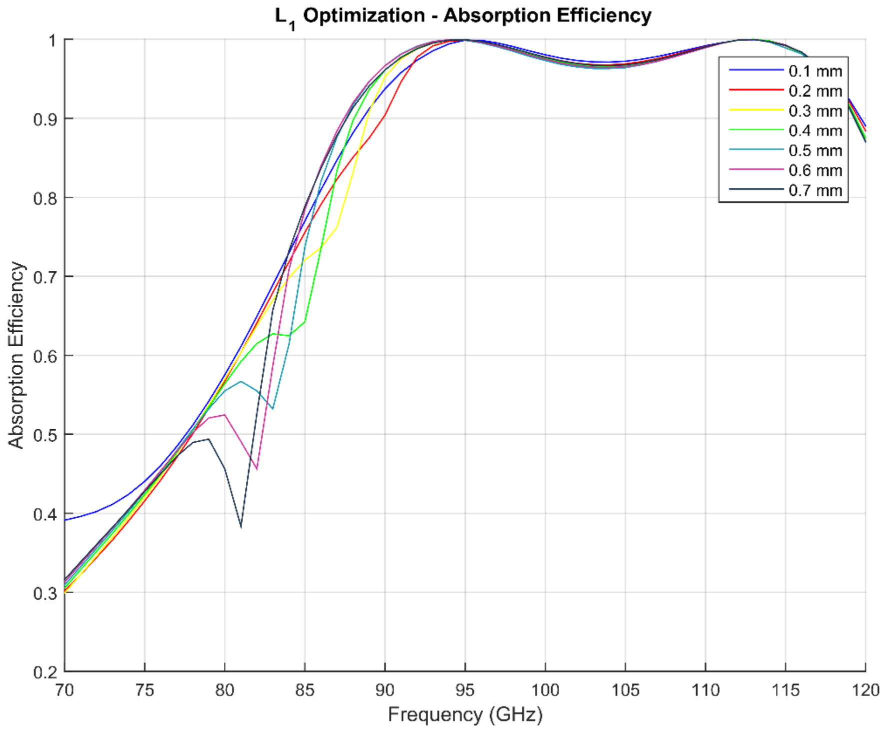

Figure 2.34 Absorption Efficiency of choke height optimization runs

No.	Parameter	Optimized Value
1	L_1	0.56 mm
2	W_2	0.4 mm
3	L_2	0.07 mm
4	W_2	0.1 mm
5	L_3	0.4 mm
6	W_3	0.3 mm
7	Choke Height	0.5 mm
8	Back-short	0.5 mm

Table 2.1 Optimized parameters of waveguide-to-microstrip transition

2.6.4 Tapering transformer

The eventual width of the microstrip line that is ~503mm long and through which the phase shift is to be measured is 3 µm wide. However, for ease of impedance matching and microstrip probing the microstrip line width at the end of the impedance matching component in Figure 2.21 is kept at 100 µm. Therefore there is a need to transform the 100 µm line to a 3 µm. This transformation is done by a tapering section elaborated as follows.

A load of Z_L can be matched to a input impedance Z_{in} by using a quarter-wave section of transmission line with $Z_c = \sqrt{Z_L Z_{in}}$ (Figure 2.35). The impedance is then matched only at the frequency at which the electrical length of the matching section is $L = \lambda/4$ [25].

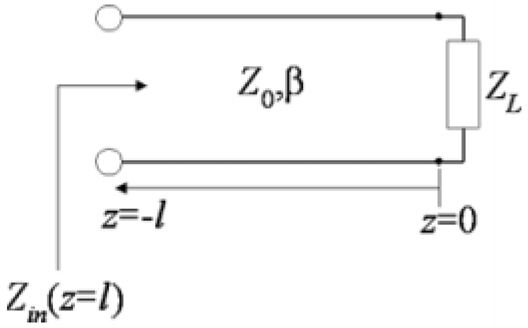

Figure 2.35 Quarter-wave transformer for matching Z_{in} and Z_L [26].

However, a single quarter-wave transformer is inadequate for a wider bandwidth application. The bandwidth can be increased by using cascaded quarter wave transformer sections which can match to the load in steps (Figure 2.36) or a continuous transformation like a tapering (Figure 2.37). The length of the tapering transformer is determined by the lowest operation frequency and the maximum reflection coefficient allowed in the pass band (Figure 2.38).

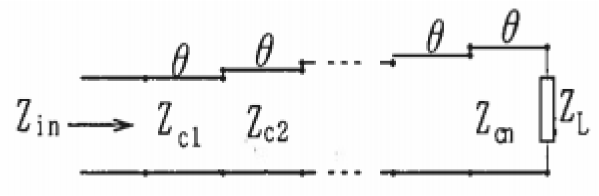

Figure 2.36 Stepped impedance transformer [29]

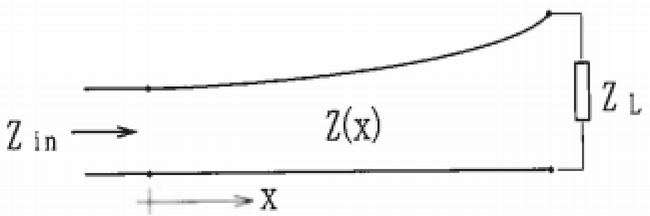

Figure 2.37 Continuous impedance transformer [29]

The impedance of a tapered matching is defined by its length L and its tapering function. The bandwidth of a tapered line increases [30]. If the tapered section has an electrical length of two or more wavelengths, the impedance transformation takes place with negligible reflections over a broad band of frequencies [31].

Sonnet Suites simulations were done in order to simulate a triangular tapering from 100 µm down to 3 µm. The optimized length of the taper L is 0.7 mm. Following illustrations show the structure and transmission and reflection characteristics of the tapering transformer. Since the microstrip is to be biased (as discussed in previous sections), a bias T solder pad is placed before the beginning of the taper. A grounding pad is added on the path to dc pad that shorts out unwanted resonances.

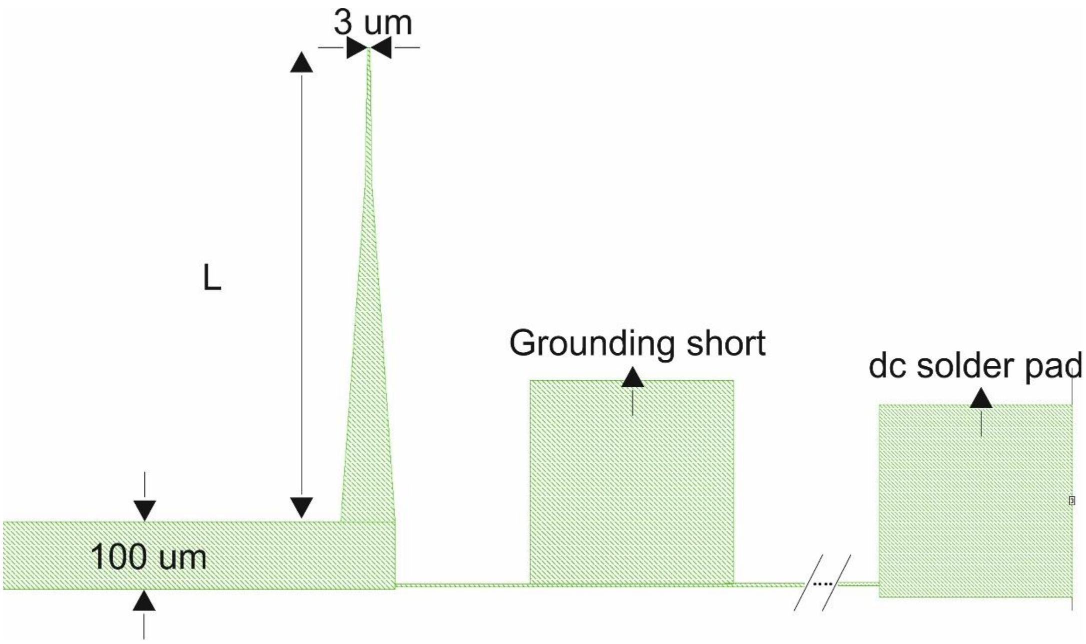

Figure 2.38 100 µm to 3 µm tapered transformer with grounding short and dc bias T.

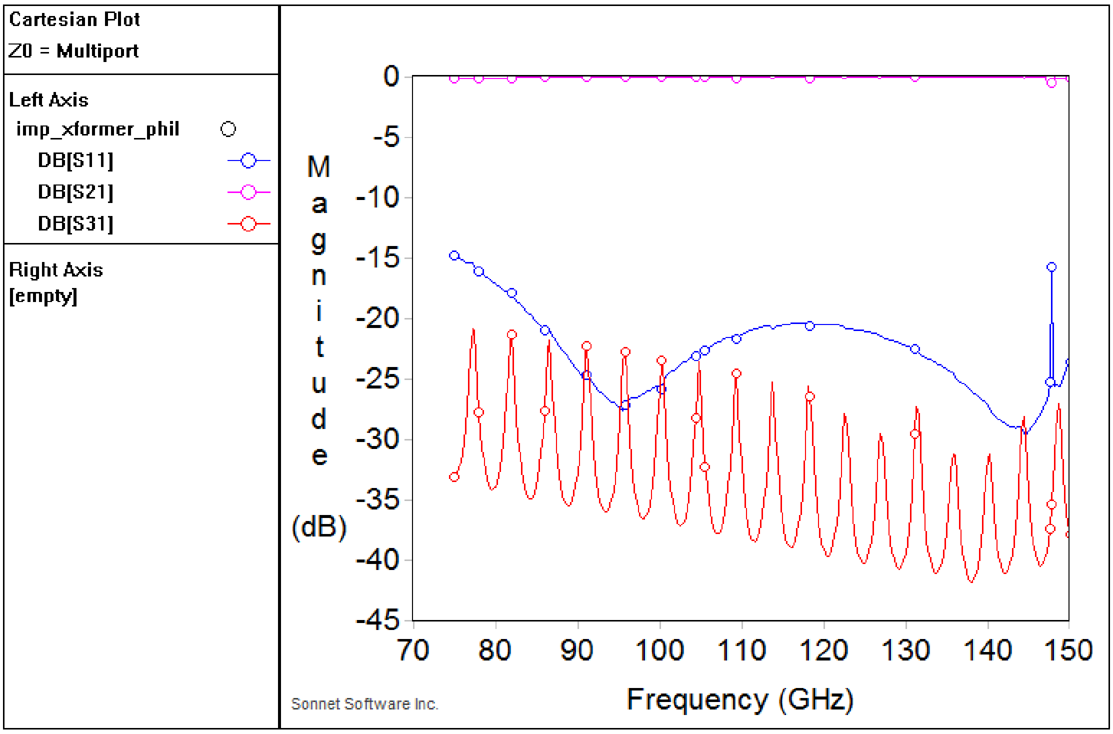

Figure 2.39 S parameters of the tapered transformer. S11 indicates the reflection coefficient from the 100 µm line, S21 indicates the transmission coefficient to the 3 µm line and S31 indicates the transmission coefficient to the dc solder pad.

2.6.5 Calibration Microstrip Lines

The two pairs of two microstrip lines in the phase shifter circuit have one pair for calibration and the other pair for the actual phase shifting. The calibration microstrip lines are ~23.8 mm long starting with a waveguide-to-microstrip transition and an impedance transformer tuned to one orthogonal polarization. Since the circular waveguides are fed by horn antennas and then are attached to the chip housing package through couplers, a calibration of this whole arrangement is necessary before the phase shifter branch is operated. The calibration microstrip lines will give a baseline for reflection and transmission through the horn antennas-waveguides-coupler-chip construction.

2.7 Fabrication

Currently, the phase shifter is designed and simulated and it is proposed to be fabricated here at ASU and to be tested with our collaborators at Jet Propulsion Laboratory (JPL) and National Institute of Science and Technology (NIST). As discussed earlier the entire phase shifter circuit on the silicon substrate will have two waveguide-to-microstrip transitions each with two pairs of two microstrip probe – two probes for each polarization of the W-band signal, identical impedance matching sections and tapered transformers to convert 100 µm sections everntually to 3 µm microstrip lines. There will be two pairs of two arms of microstrip lines, one arm having a ~503mm long microstrip line while the other with a ~23.8 mm long microstrip line. The CAD layout of the phase shifter circuit is illustrated in Figure 2.41. The silicon substrate is etched from a ~332 µm thick silicon-on-insulator (SOI) wafer (Figure 2.40).

A handle wafer surrounds the etched silicon substrate which is very useful in to carry the wafer while processing, during measurements and packaging. To etch a depth of ~300 µm of the SOI down to the silicon substrate, an anisotropic Bosch etch is necessary with a resist of very low selectivity over silicon (approximately 1:100). A deposition of NbTiN is done with a sputter deposition here at ASU. All the fabrication and processing steps are illustrated in Figure 2.42.

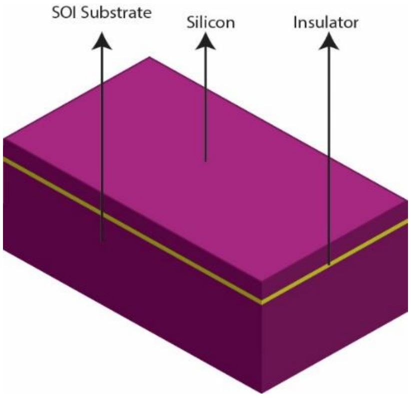

Figure 2.40 SOI wafer with insulator (SiO_2) and 30 µm silicon substrate.

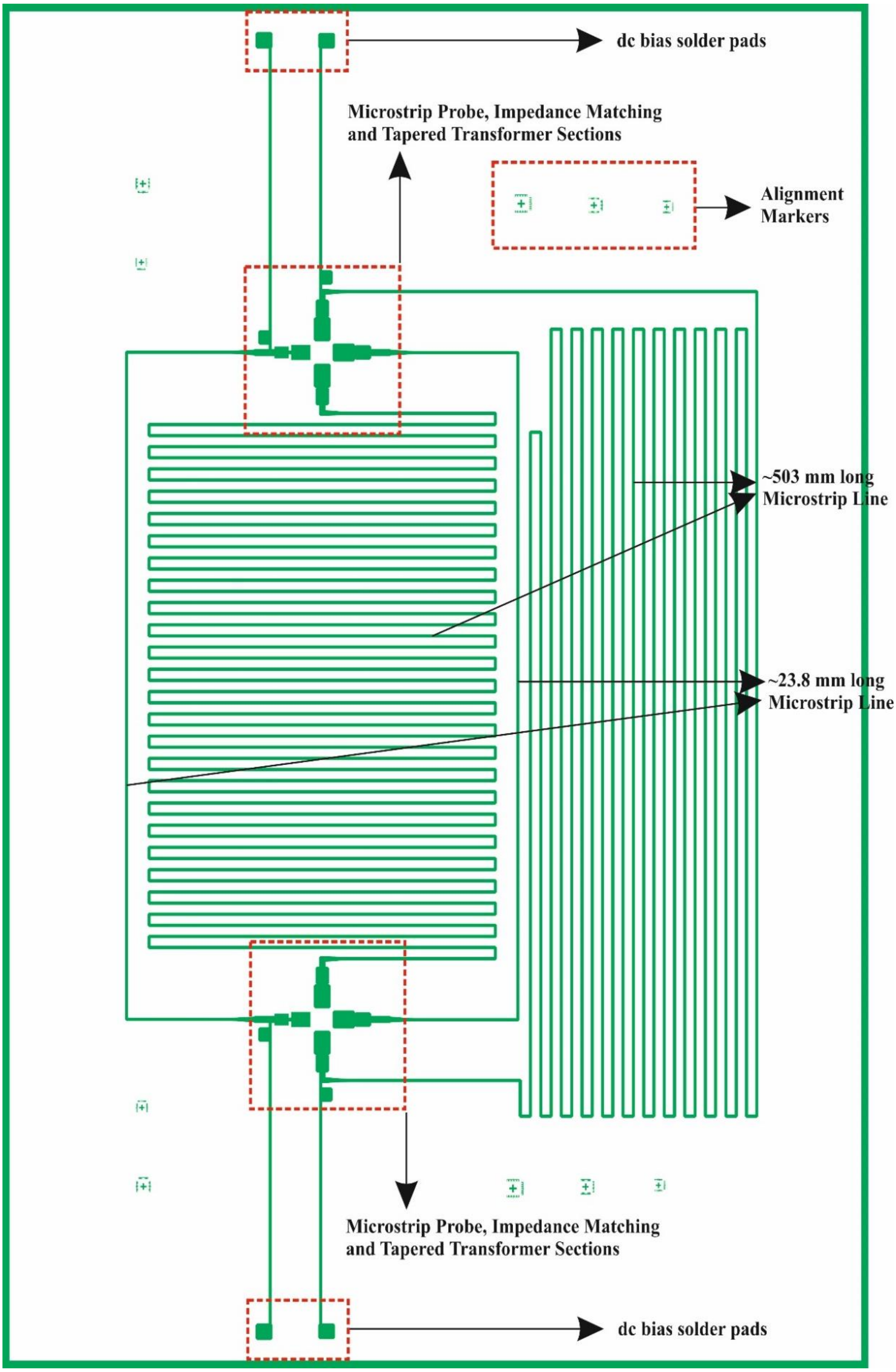

Figure 2.41 CAD layout of the phase shifter circuit

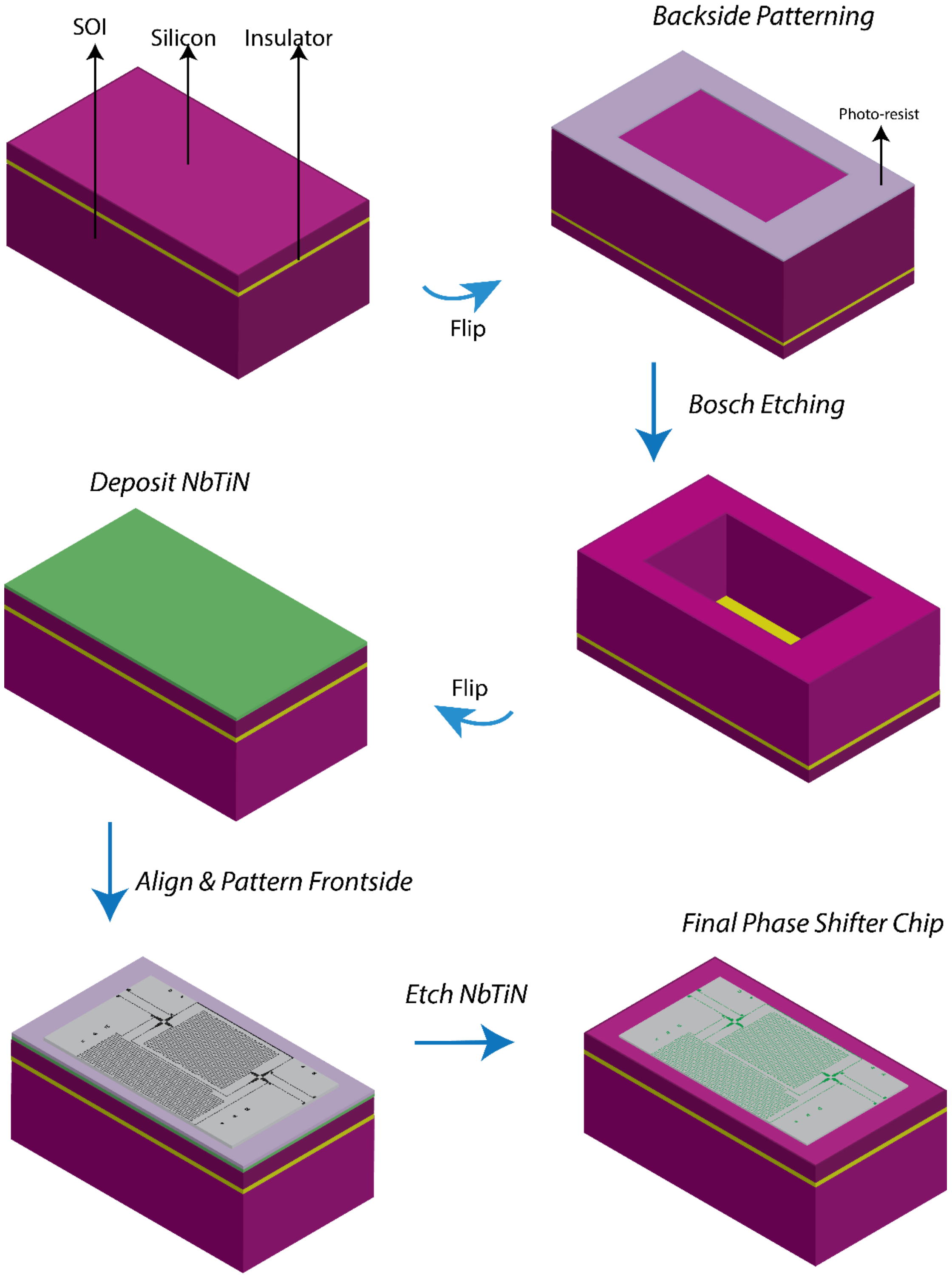

Figure 2.42 Fabrication process of the phase shifter chip

2.8 Packaging

The phase shifter chip and a pair of PCBs for bias-T, will be housed in a three-piece copper enclosure, to be precision machined at ASU in Spring, 2016. The input and output W-band circular waveguides will be attached with a coupler section to the copper packaging. The packaging is chosen of copper so as to ensure minimum thermal contraction when cooled to 4.2 K and also because of ease of manufacturing. The two W-band circular waveguides will be fed by a pair of horn antennas coupled at their open ends. This entire arrangement of the horn antennas, circular waveguides and the copper packaging that houses the phase shifter chip will be placed inside a cryostat that cools to 4.2 K (Figure 2.43).

A 1-liter liquid Helium cryostat will be used to house the phase shifter during testing. A small, single stage 4 K cryostat was chosen because of its fast turnover time, and ~ 6-hour hold-time. The copper phase shifter enclosure will be mounted to the 4 K cold plate with the side holding the welded circular waveguide pointing out towards an NW-40 vacuum flange. The two pieces of waveguide will be fed through a small vacuum chamber and joined to rectangular W-band horns that connect with standard circular-to-rectangular waveguide flanges. The input and output signal will be coupled between two pairs of W-band horns, mounted face to face at a 1/16" vacuum window fabricated from high density polyethylene (HDPE) (Figure 2.44). HDPE was chosen because it is economical, while permitting sufficient W-band transmission without the need for fabricating a multi-layer window. Since the phase shift test is a relative measurement, the maximum magnitude of S21 is not an important consideration, and some signal loss can be incurred through the vacuum window without compromising the measurement. The W-band signal will be coupled to the test setup via Vector

Network Analyser (VNA) extenders that are currently available for use in our laboratory.

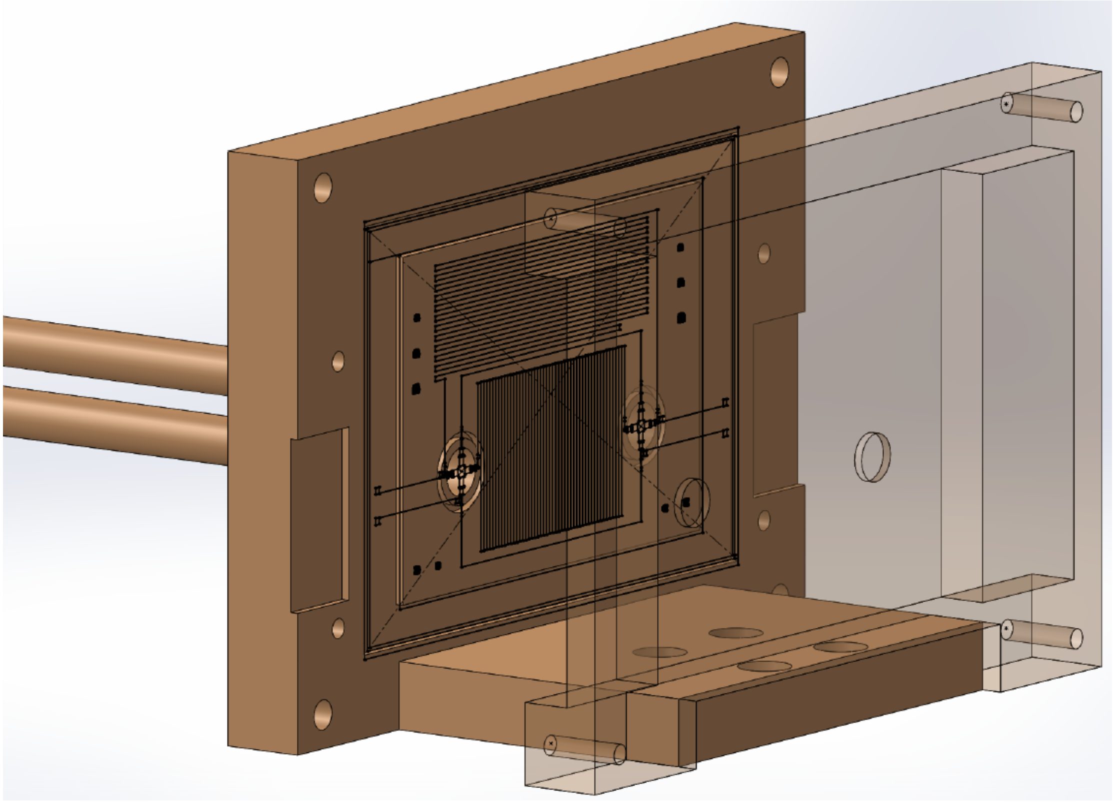

Figure 2.43 Copper packaging that will house the phase shifter chip and which will be mounted on the 4.2 K stage of the test cryostat. As seen, the two W-band circular waveguides are coupled to the packaging. The copper piece on the right side will be joined with the piece on the right with screws leaving a 50 μm gap between the chip and the right piece.

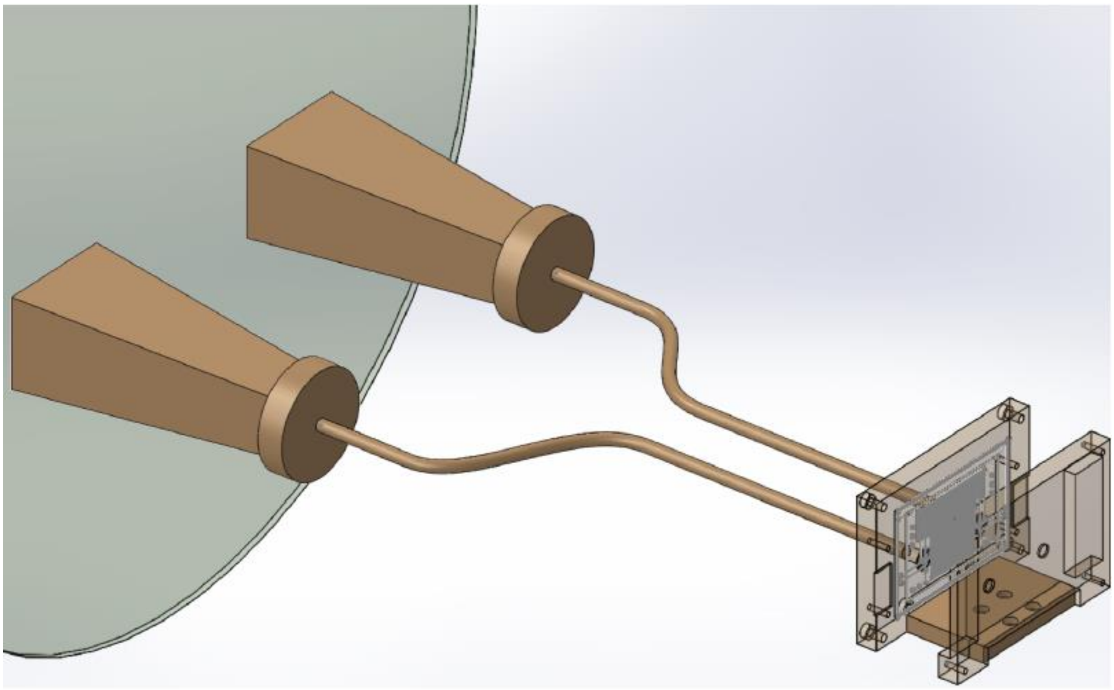

Figure 2.44 A view from inside the test cryostat where the package and waveguides are coupled to the horn antennas that face the HDPE window.

2.9 Conclusions and Future Scope

A distributed kinetic inductance of a superconductor transmission line is utilized into obtaining a length and current dependent phase velocity and hence a variable phase shift $\Delta\phi$. A pump tone and a signal tone can be mixed together to obtain gain in the signal tone that is quadratically dependent on the maximum phase shift $\Delta\phi_{max}$. We have designed here a ~503 mm phase shifting NbTiN superconducting transmission line which theoretically predicts a gain of ~49 dB for a meter of transmission line and a phase shift of ~ 1300 radians at 90 GHz. We have also designed the complete circuit required to achieve this phase shifter and a copper package housing the phase shifter that is to be mounted on a 1.2 K stage inside a cryostat. The W-band signal (75 GHz to

115 GHz) signal is thought to be fed through horn antennas coupled to the circular waveguide on the phase shifter side and with another set of horn antennas that will feed through a HDPE window from outside the cryostat.

The designs are ready for fabrication and manufacturing and will be assembled and tested here at ASU.

CHAPTER 3.

PART II

MICROSTRIP TO SLOT LINE TRANSITION FOR 150 GHz and 220 GHz FREQUENCIES

3.1 Introduction and Scientific Motivation

A project to develop a 20-element prototype arrays of horn-coupled, polarization-sensitive microwave kinetic inductance detectors (MKIDs) that are each sensitive to multiple spectral bands between 130 and 280 GHz, is part of a proposal in collaboration with research groups from Columbia, Stanford, Cardiff and ASU. These MKID arrays are tailored for experiments that are designed to simultaneously characterize the polarization properties of both the cosmic microwave background (CMB) and Galactic dust emission. The research program focuses on (i) developing the coupling between our distributed aluminum MKID design and the Truce-developed on-chip millimeter-wave polarimeter circuit and (ii) demonstrating that the sensitivity of theses arrays is competitive. The 20-element arrays we chose to develop allows to test the detector performance and the full readout bandwidth, and the prototype array design is directly scalable to 331-element arrays, which can be tiled into a 9268 detector array.

Figure 3.1 shows photographs of their horn and detector chip and a rendering of a microwave kinetic inductance detector (MKID) that is sensitive to 150 and 220 GHz spectral bands. Incoming radiation enters a detector holder that supports a planar detector chip in front of a waveguide back short and uses a waveguide choke to prevent lateral leakage of fields from the waveguide.

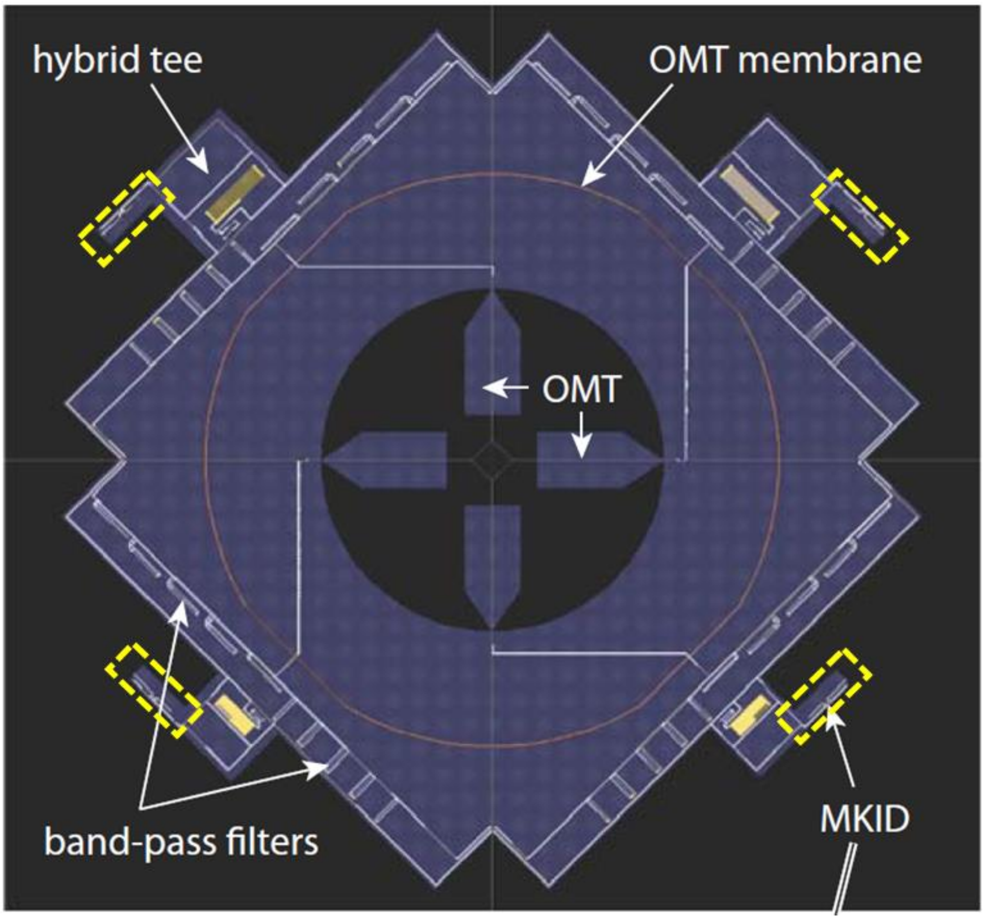

Figure 3.1 A prototype of a multi-chroic device

The detector chip (Figure 3.1) uses a broadband orthogonal mode transducer (OMT) to couple the incoming light from the waveguide onto high impedance coplanar waveguide (CPW) lines. The OMT separates the incoming light according to linear polarization. Along each path, a broadband CPW to micro-strip (MS) transition comprised of 7 alternating sections of CPW and MS is used to transition the radiation onto MS lines. Next, diplexers comprised of two separate five pole resonant stub band-pass filters separate the radiation into 75 to 110 and 125 to 170 GHz pass-bands. The signals from opposite probes within a single sub-band are then combined onto a single MS line using the difference output of a hybrid tee. This part of the thesis deals in designing and optimizing the CPW to MS transition as shown in Figure 3.2.

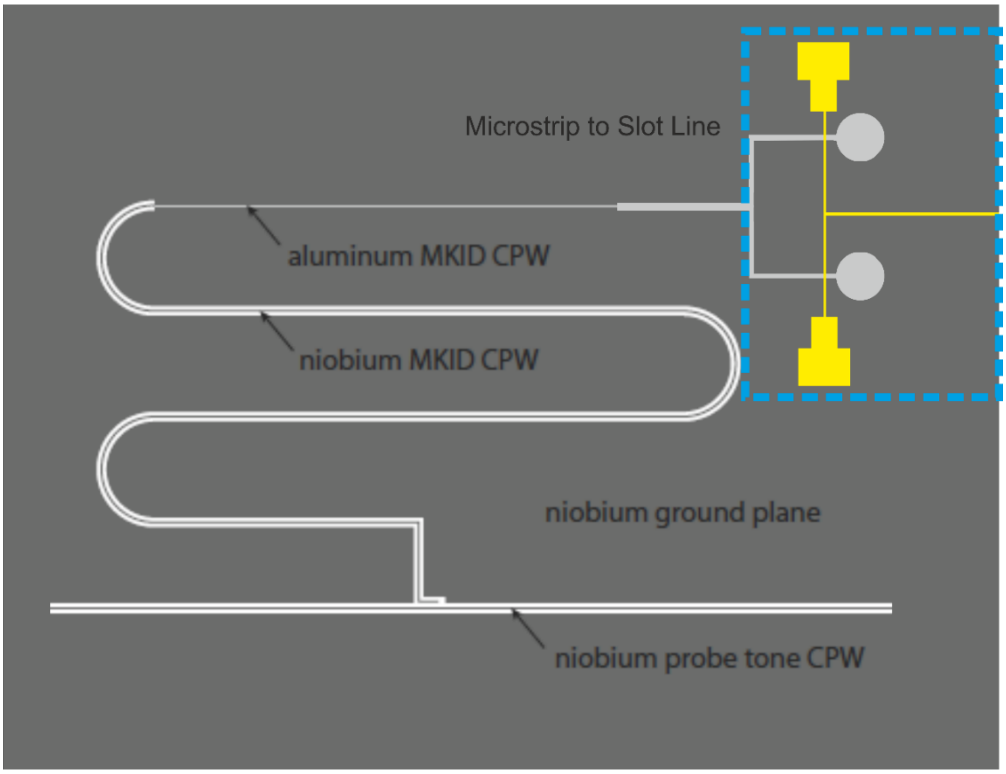

Figure 3.2 Insertion place of microstrip to slot line transition

3.2 Slot Line

A slot line is a planar structure first proposed for use in MICs by Cohn, 1968 [34]. The basic slot line configuration shown in Figure 3.3 consists of a dielectric substrate with a narrow slot etched in the metallization on one side of the substrate. The other side of the substrate is without any metallization.

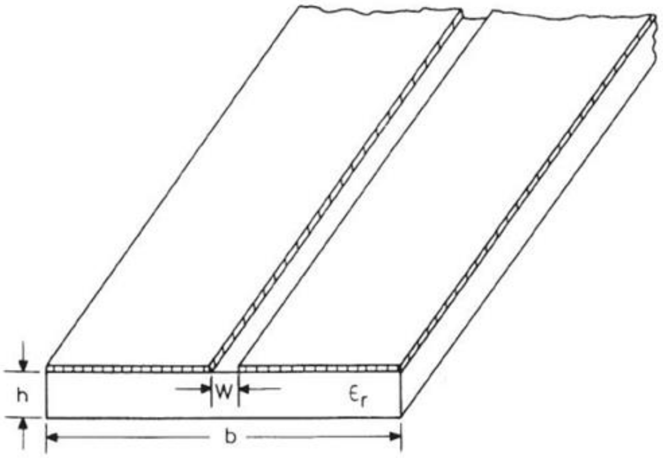

Figure 3.3 Slot line configuration [22].

A practical slot line, the radiation is minimized by using a high permittivity substrate which causes the wavelength transmitted in the slot line λ' to be small compared to the free space wavelength λ. This closely confines the electric and magnetic fields to the slot with negligible radiation loss. For instance, for a substrate relative permittivity $\epsilon_r = 20$, the ratio of the wavelengths in the substrate and free space will be $\lambda'/\lambda = 1/3$. When an alternating voltage is applied between the two metal planes of the slot line, an electric field extends across the slot and the magnetic field is perpendicular to the slot as illustrated in Figure 3.4. Observing the magnetic field lines in Figure 3.4, the magnetic field lines curve and return to the slot at half wavelength intervals. The surface current density is greatest at the edges of the slot and decreases rapidly with distance from the slot.

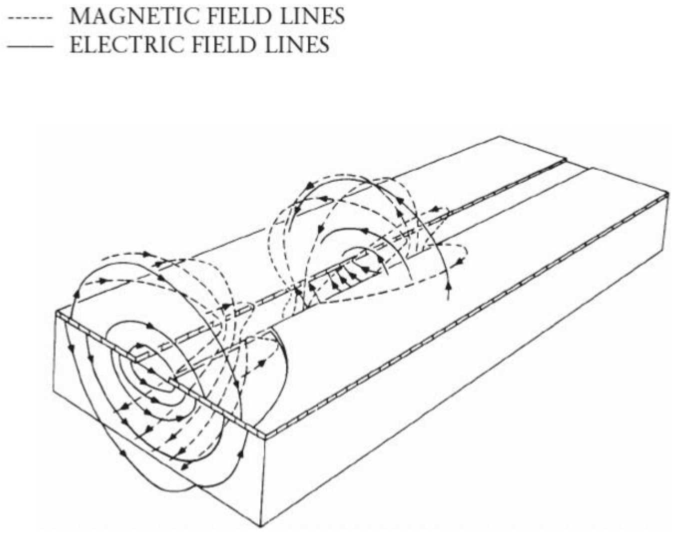

Figure 3.4 Field distribution in a slot line.

3.2.1 Slot Line Field Equations

The slot line can be characterized by its electrical parameters of characteristic impedance Z_0 and the phase velocity ν. Because of the non-TEM nature of the slot line mode these parameters are not constant but vary with frequency. The slot line has no cut-off frequencies down to $f = 0$ where if metal coated substrate is assumed infinite in length and width, ν/c approaches unity and Z_0 approaches zero. The slot line fields can be divided into three electric field components and three magnetic field components. The longitudinal component of the electric field is weak since most of the electric field is confined between the two conductors. If the width W (Figure 3.3) is much smaller than the free space wavelength λ_0, the electric field across the slot can be thought of as an equivalent line source of magnetic current. This leaves the far-field with only three components of the magnetic field H_x, H_r and E_ϕ. For a distance r in the air region the field equations [22] can be written as

$$H_x = AH_0(k_c r) \tag{3.1}$$

$$H_r = -\left(\frac{\gamma_x}{k_c^2}\right)\frac{\partial H_x}{\partial r} = \frac{A}{\sqrt{1-\left(\frac{\lambda_s}{\lambda_0}\right)}}H_1(k_c r) \tag{3.2}$$

$$E_\phi = \frac{j\omega\mu}{k_c^2}\frac{\partial H_x}{\partial r} = -\frac{\eta H_r \lambda_s}{\lambda_0} \tag{3.3}$$

where γ_x is the propagation constant along the x-direction which is the propagation and k_c is related to the slot wavelength λ_s by the equation

$$k_c = j\frac{2\pi}{\lambda_0}\sqrt{\left(\frac{\lambda_0}{\lambda_s}\right)^2 - 1} \tag{3.4}$$

3.2.2 Slot Line Wavelength

As illustrated in Figure 3.4 the slot line fields are not confined to the substrate alone and are extended into the air region above the slot and below the substrate as well. Therefore the effective permittivity of a slot line (ϵ_{re}) is less than the substrate permittivity (ϵ_r). The zeroth order value of ϵ_{re} for a slot on an infinitely thick substrate is the average dielectric constant of the two media [35],

$$\epsilon_{re} = \frac{\epsilon_r + 1}{2} \tag{3.5}$$

and therefore,

$$\frac{\lambda_s}{\lambda_0} = \sqrt{\frac{2}{\epsilon_r + 1}} \tag{3.6}$$

For a slot line of finite thickness substrate, the above value of λ_s/λ_0 is approached for the cut-off thickness for the TE_0 surface wave mode [22].The cut-off thickness is given by

$$\frac{h}{\lambda_0} = \frac{0.25}{\sqrt{\epsilon_r - 1}} \tag{3.7}$$

3.2.3 Slot Line Impedance

The characteristic impedance Z_0 cannot be defined uniquely because of the non-TEM nature of the slot line. From the power-voltage relationship the impedance can be written as [36]

$$Z_{0s} = \frac{|V|^2}{2P}. \tag{3.8}$$

where V is the peak voltage across the slot. The average power P is written in terms of energy storage W_t, which can be written in terms of rate of change of total susceptance B_t wit frequency,

$$W_t = \left(\frac{V^2}{4}\right)\left(\frac{\partial B_t}{\partial \omega}\right) \tag{3.9}$$

and since

$$W_t = \frac{\pi P}{2\omega}\frac{v}{v_g} \tag{3.10}$$

we can write

$$Z_{0s} = \frac{v}{v_g}\frac{\pi}{\frac{\omega \partial B_t}{\partial \omega}}. \tag{3.11}$$

For $p = \lambda_0/\lambda\_s$, it may be expressed as

$$Z_{0s} = \eta \frac{v}{v_g} \frac{\pi}{p} \left\{ \frac{\Delta p}{-\Delta(\eta B_t)} \right\}. \tag{3.12}$$

Here the phase velocity v is related to the group velocity v_g as,

$$\frac{v}{v_g} = 1 - \frac{f}{\frac{\lambda_s}{\lambda_g}} \frac{\Delta\left(\frac{\lambda_s}{\lambda_0}\right)}{\Delta f}. \tag{3.13}$$

3.2.4 Slot Line Discontinuity – Short End

A slot line when terminated by merely ending the slot or by filling the slot with a conductor surface lying in the plane of the slot, it creates a short end discontinuity. The current flows on the metal surface at the end of the slot as shown in Figure 3.5. The stored magnetic energy due to the surface currents at the short end gives rise to an inductive reactance at a plane normal to the slot axis and coincident with the end of the slot.

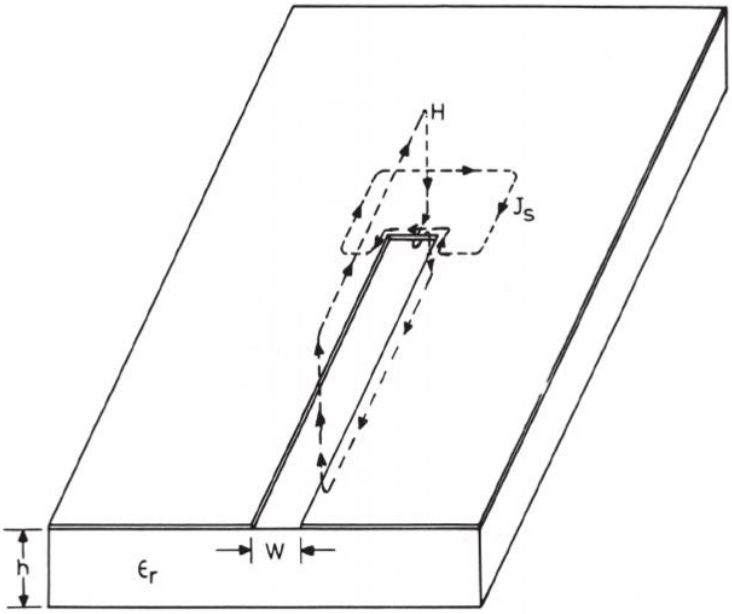

Figure 3.5 Short end field and current distributions [22]

The end reactance of a short ended slot line is purely inductive and increases with increase in slot width and h/λ_0 ratio. Propagation of power in surface waves and radiation causes losses in the short end in a slot line and are described by an equivalent resistance of R. The equivalent circuit of a short end on a slot line is therefore a series combination of an inductor and a resistor.

3.2.5 Slot Line Discontinuity – Open End

A slow tapering out at the end of the slot line contributes to an open end as shown in Figure 3.6. A typical open end used in practice is a circular disc open end or a combination of a flared slot and a half disc open end as shown in Figure 3.7

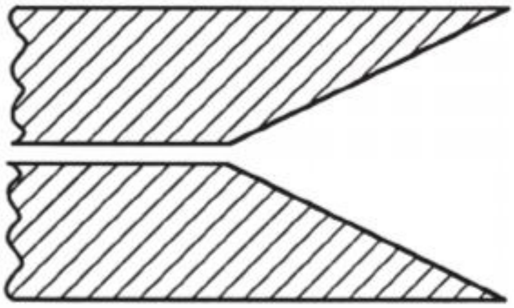

Figure 3.6 A flared open end as a slot line discontinuity.

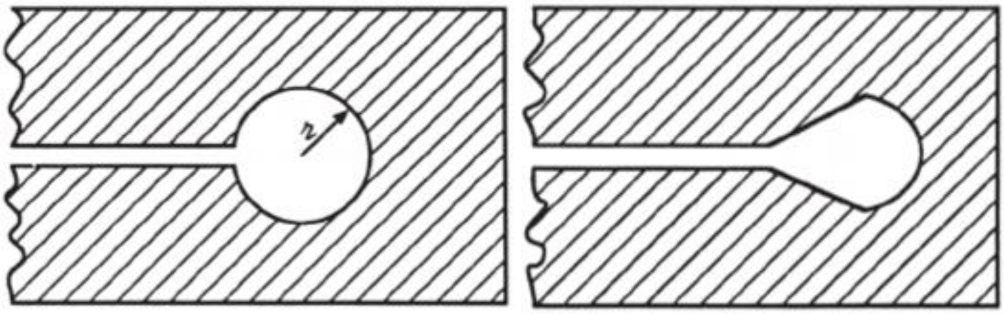

Figure 3.7 Circular disc open ended and a combination of flare and half-disc open ended slot line discontinuity.

A larger disc radius in the circular disc open end the smoother is the termination and better will be the open-circuit behavior. The circular disc may also behave like a resonator if the slot width is very narrow as compared to the disc radius [37].

3.3 Microstrip Discontinuities

Microstrip discontinuities include open ends, gaps, steps in width, right angled bends, T-junction and cross junctions of which stepped width, right angles and T-junctions are used in this design of microstrip-to-slot line. Following sub-sections elaborate these three discontinuities.

3.3.1 Stepped Discontinuity

A difference in widths of the microstrip at a junction contributes a stepped discontinuity. The two varying widths have difference in their impedances. The discontinuity results in an excess capacitance C_s as shown in Figure 3.8

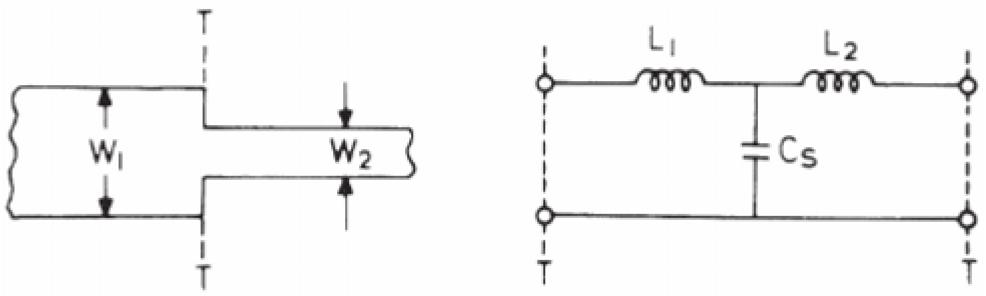

Figure 3.8 Microstrip stepped discontinuity and its equivalent circuit [22].

In terms of distributed elements, the discontinuity capacitance C_s has the effect of an increase in the wide line's length and an equal decrease in the narrow line's length that is given by [38],

$$\Delta l_{oc} f(\epsilon_r)\left[1-\frac{W_2}{W_1}\right] \tag{3.14}$$

where Δl_{oc} is the open circuit line extension given by,

$$\frac{\Delta l_{oc}}{h}=\frac{C_{oc}}{W}\frac{cZ_{0m}W}{h\sqrt{\epsilon_{re}}} \tag{3.15}$$

where C_{oc} is the open end capacitance (calculated empirically) and $f(\epsilon_r)$ is given by,

$$f(\epsilon_r)=1.25+0.19\tan^{-1}(6.16-\epsilon_r). \tag{3.16}$$

The inductance per unit length associated with the step discontinuity in a microstrip of width W_1 is given by [39]

$$L_{w1}=\frac{Z_{0m}\sqrt{\epsilon_{re}}}{c}\ (H/m). \tag{3.17}$$

The individual additional inductances L_1 and L_2 can be written in terms of the total inductance L_s by [22],

$$L_1=\frac{L_{w1}}{L_{w1}+L_{w2}}L_s. \tag{3.18}$$

$$L_2=\frac{L_{w2}}{L_{w1}+L_{w2}}L_s. \tag{3.19}$$

and the corresponding additional lengths may be written as

$$\frac{\Delta l_1}{h}=\frac{\Delta l_2}{h}=\frac{L_s}{L_{w1}+L_{w2}} \tag{3.20}$$

3.3.2 Right Angle Bends

A bend in a microstrip may be formed between equal or unequal impedance lines. An equivalent circuit as shown in Figure 3.9 includes an extra capacitance and parallel conductance.

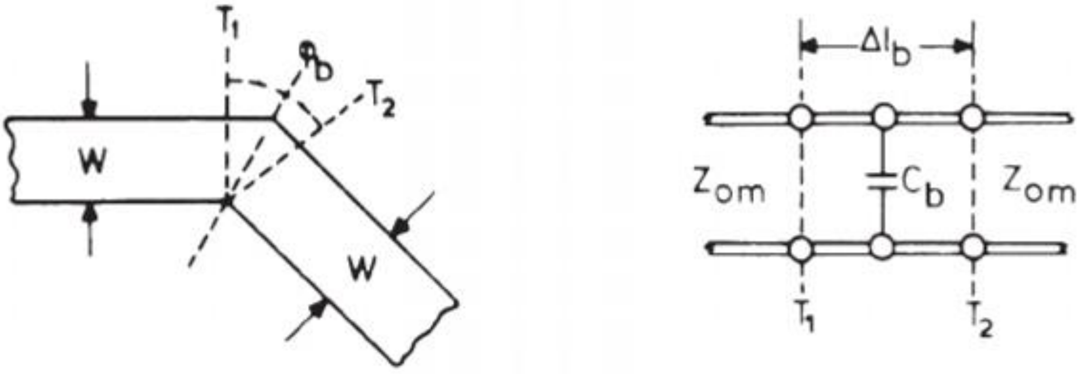

Figure 3.9 A microstrip line bend and its equivalent circuit. [22]

Expressions for right angled bend discontinuities are given in [40] as,

$$\frac{C_b}{W}\,(pF/m) = \left\{\frac{\frac{(14\,\epsilon_r + 12.5)W}{h} - (1.83\,\epsilon_r - 2.25)}{\sqrt{\frac{W}{h}}} + 0.02\,\frac{\epsilon_r}{\frac{W}{h}}\right\} \tag{3.21}$$

$$\dots for\ (W/h < 1)$$

and

$$\frac{C_b}{W}\,(pF/m) = \left\{(9.5\,\epsilon_r + 1.25)\frac{W}{h} + 5.2\,\epsilon_r + 7.0\right\} \tag{3.22}$$

$$\dots for\ (W/h \geq 1)$$

and

$$\frac{L_b}{h}\,(nH/m) = 100\left(4\sqrt{\frac{W}{h}} - 4.21\right) \tag{3.23}$$

3.3.3 T-junctions

A T-junction is very common in microwave filters, impedance networks, couplers etc. The equivalent circuit for a T-junction consists of an extra discontinuity capacitance C_T and a network of inductances in parallel to C_T as shown in Figure 3.10.

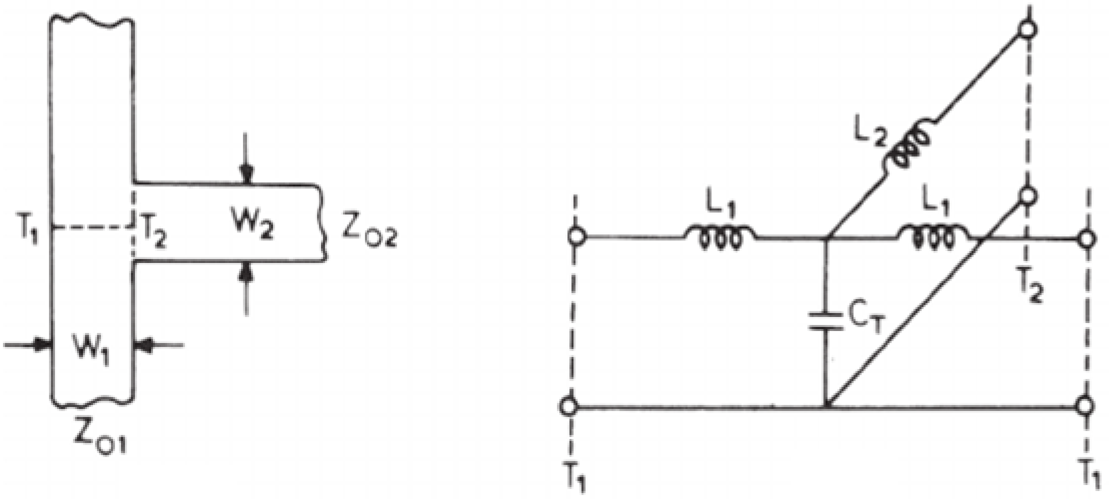

Figure 3.10 A microstrip T-junction and its equivalent circuit [22].

For symmetric T-junctions, the discontinuity reactances of the equivalent circuit with a main-line impedance of 50 Ω and for $\epsilon_r = 9.9$ the expression [40] is given as

$$\frac{C_T}{W_1}\ (pF/m) = \frac{100}{\tanh(0.0072\, Z_0)} + 0.64\, Z_0 - 261 \tag{3.24}$$

$$\ldots for\ (25 \leq Z_0 \leq 100)$$

where Z_0 is the characteristic impedance of the stub. The inductance per unit length [40] in the equivalent circuit are given by,

$$\frac{L_1}{h}\left(\frac{nH}{m}\right) = -\frac{W}{h}\left\{\frac{W_2}{h}\left(-0.016\frac{W_1}{h} + 0.064\right) + \frac{0.016}{\frac{W_1}{h}}\right\} L_{w1} \tag{3.25}$$

$$\ldots for\ \left(0.5 \leq \left(\frac{W_1}{h}, \frac{W_2}{h}\right) \leq 2.0\right)$$

and

$$\frac{L_2}{h}\left(\frac{nH}{m}\right) = \left\{\left(0.12\frac{W_1}{h} - 0.47\right) + 0.195\frac{W_1}{h} - 0.357 + 0.0283\sin\left(\pi\frac{W_1}{h} - 0.75\pi\right)\right\} L_{w2} \tag{3.26}$$

$$\ldots for\ \left(1 \leq \frac{W_1}{h} \leq 2.0; 0.5 \leq \frac{W_2}{h} \leq 2\right)$$

where L_w is the inductance per unit length for a microstrip of width W.

3.3.4 Microstrip to Slot Line Transition

Combining the above equivalent circuits, a microstrip to slot line transition can be carefully designed to obtain maximum transmission and minimum reflection losses. Figure 3.11 shows an impedance matched microstrip to circular disc ended slot line transition. The microstrip end appears as a short circuit while the circular dis end of the slot line appears as an open circuit. An equivalent of the transition is shown in Figure 3.12. L_{os} is the inductance of the shorted slot line, C_{oc} is the capacitance of the open microstrip, Z_{os}, Z_{om} are the slot line and microstrip characteristics impedances respectively. θ_s and θ_m are the electrical lengths (quarter wavelength at center frequency) od the extended portions of the slot line and microstrip respectively and n is the transformer ratio.

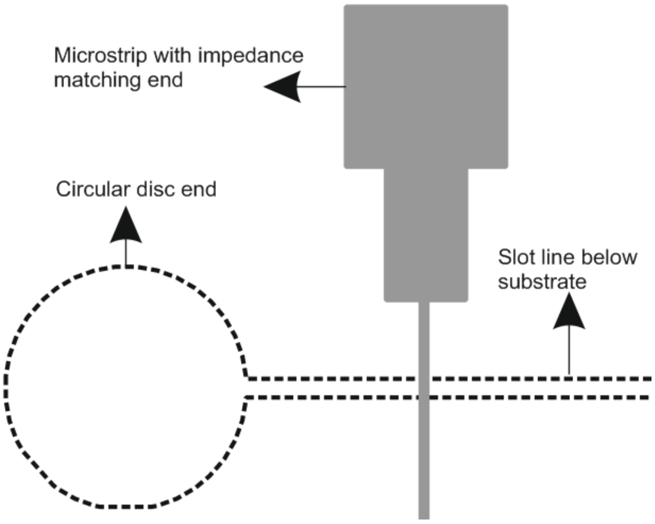

Figure 3.11 Microstrip to slot line transition with circular stubs and impedance matching end

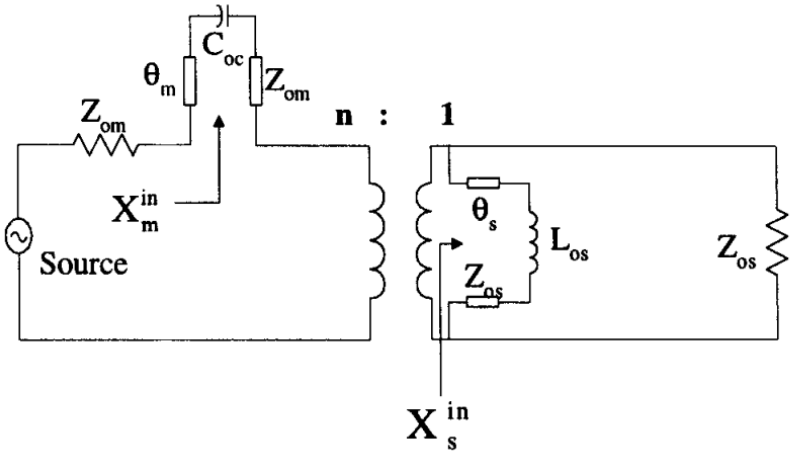

Figure 3.12 Equivalent circuit for the transition [41]

Transforming all of the circuit's components to the microstrip side, we obtain,

$$R_s = \frac{n^2 Z_{os} X_s^{in}}{Z_{os}^2 + X_s^{in}} \tag{3.27}$$

$$X_s = \frac{n Z_{os} X_s^{in}}{Z_{os}^2 + X_s^{in}} \tag{3.28}$$

$$X_m = X_m^{in} \tag{3.29}$$

The input reflection coefficient Γ_{in} is therefore given by

$$\Gamma_{in} = R_s - Z_{om} + \frac{j(X_m + X_s)}{R_s + Z_{om} + j(X_m + X_s)} \tag{3.30}$$

The geometry of the proposed MS to SL transition for this project is designed to have a configuration as shown in Figure 3.13

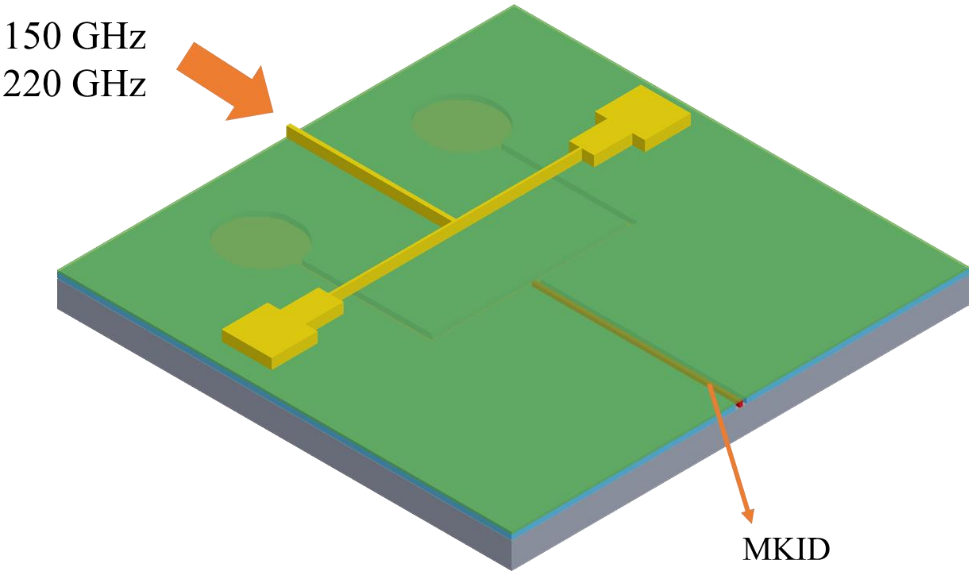

Figure 3.13 Proposed MS to SL transition

3.4 Simulations for Design Optimization

The microstrip-to-slot line design optimized here is built on a material stack as shown in Figure 3.15. The input signal is fed to a 5 µm wide microstrip line that sits on top of the 350 nm silicon nitride (SiN) while the slot line is etched from NbTiN metal that is sandwiched between the 350 nm SiN and a 5 µm thick silicon (Si) substrate. The slot line is terminated by a lossy aluminum (Al) which represents the kinetic inductance detector.

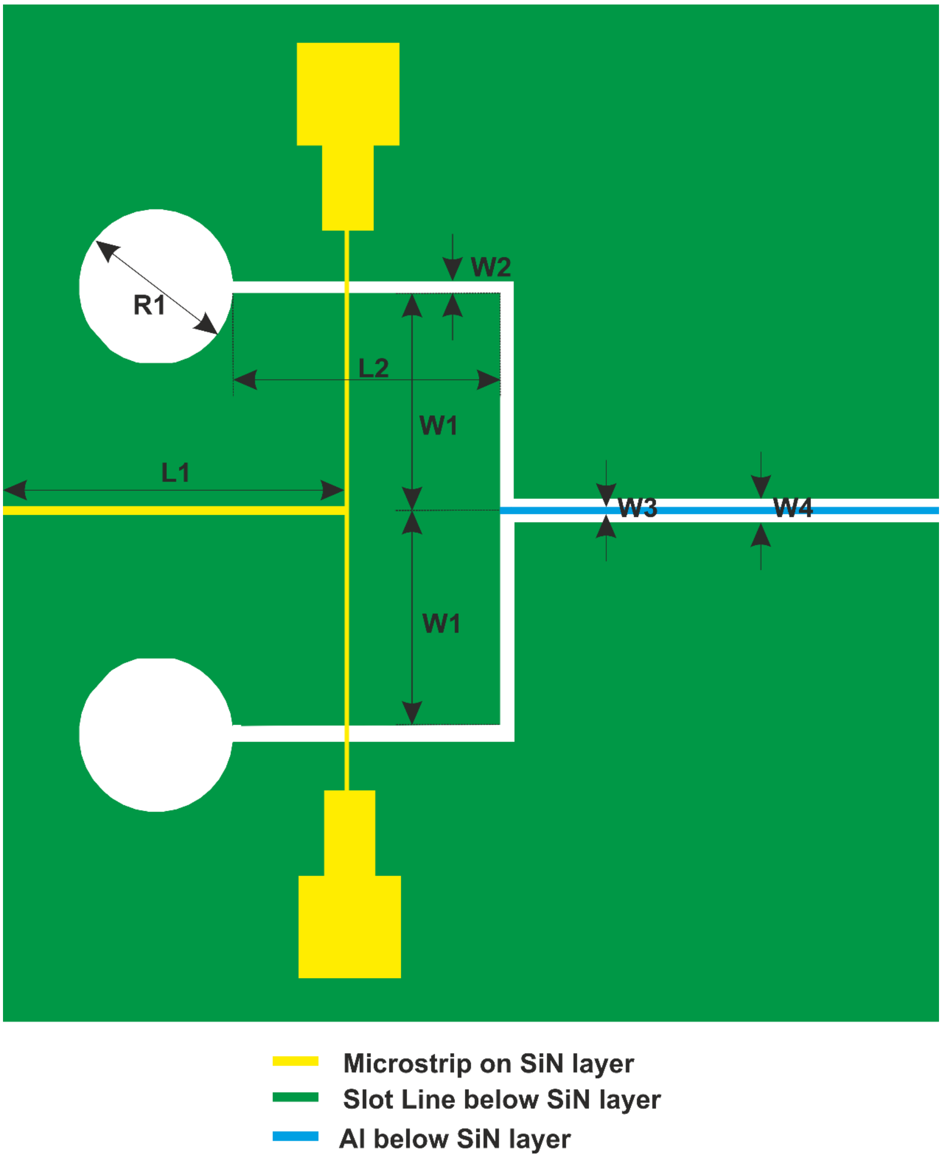

Figure 3.14 Microstrip to slotline transition layout

The slot line which is below the 350 nm SiN layer and that sits on top of a 5 µm thick Si substrate has two circular open ends followed by a right angle discontinuity to carry the signal to the lossy Al line. The microstrip starts on top of the 350 nm SiN layer is 5 µm initially and is followed by a T-junction discontinuity which is terminated by impedance matching sections on its two branches. The material stack is as shown in Figure 3.15. The crossing point of the microstrip and the slot line is approximately $\lambda/4$ from both the microstrip and the slot line ends.

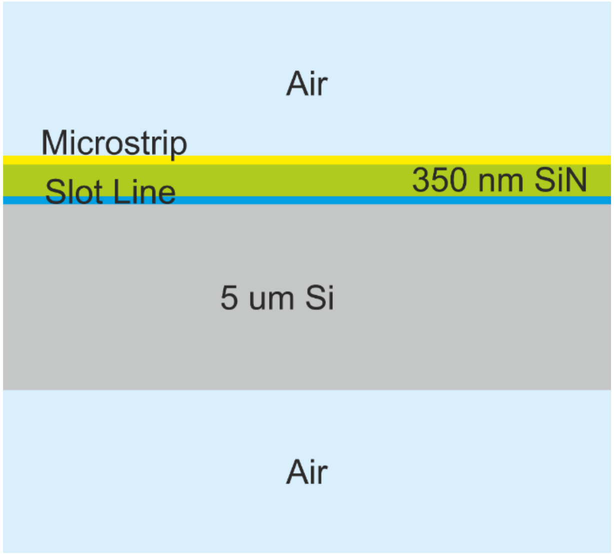

Figure 3.15 Material stack for MS to SL transition

The parameters shown in Figure 3.14 are optimized using Sonnet Suite to get maximum transmission at the Al line. The microstrip can be treated as an input port and the Al line as an output port. The parameters are optimized for a set of frequencies – 150 GHz and 220 GHz. Figure 3.16 and Figure 3.17 illustrate the S-parameters of the 150 GHz and 220 GHz optimized designs. Table 3.1 is populated with the optimized values of the parameters for both the designs.

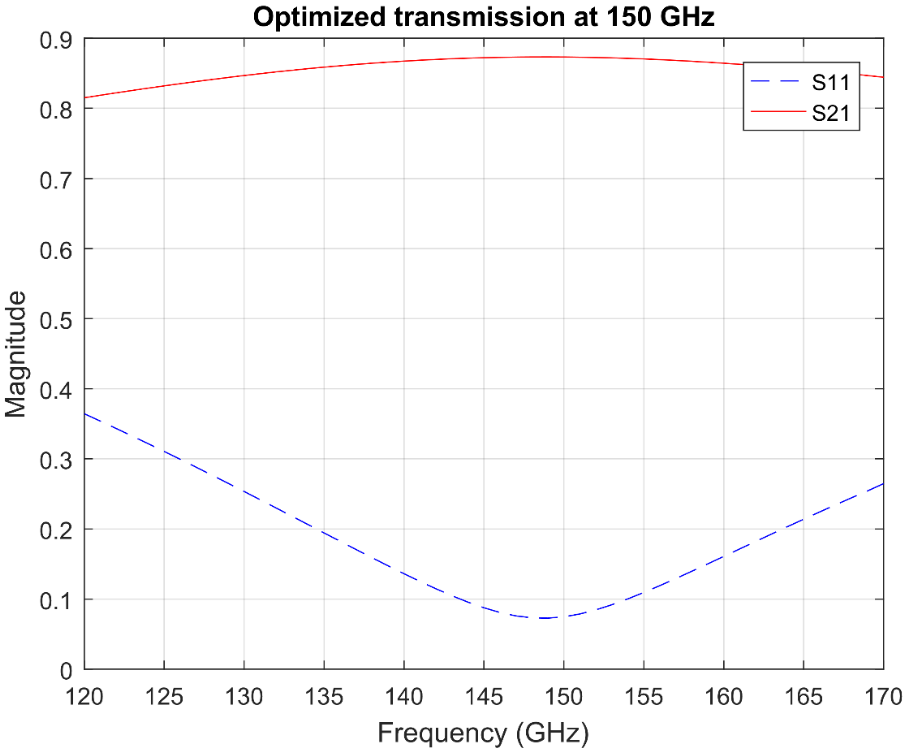

Figure 3.16 S-parameters of the design optimized for 150 GHz.

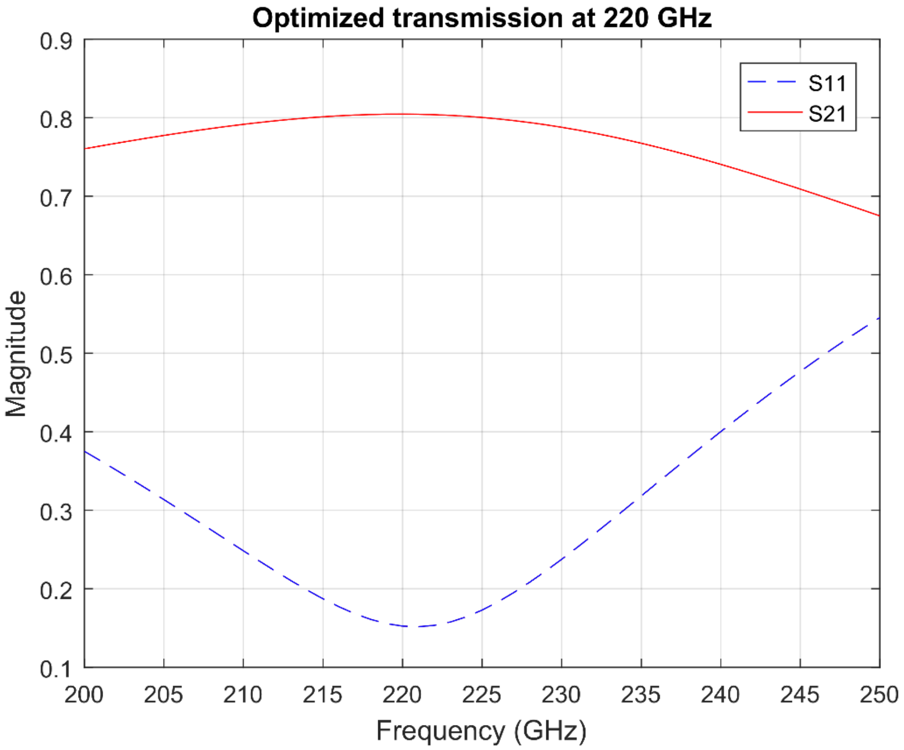

Figure 3.17 S-parameters for design optimized for 220 GHz

No.	Parameter	Optimized Value for 150 GHz	Optimized Value for 220 GHz
1	L_1	0.2 mm	0.2 mm
2	L_2	0.16 mm	0.05 mm
3	W_1	0.13 mm	0.0575 mm
4	W_2	0.002 mm	0.002 mm
5	W_3	0.004 mm	0.004 mm
6	W_4	0.014 mm	0.006 mm
7	R_1	0.09 mm	0.09 mm

Table 3.1 Optimized values of parameters of both 150 and 220 GHz designs.

3.5 Conclusion

We have designed here a microstrip to slot line transition that will be part of a microwave kinetic inductance detector readout circuit. Two separate designs of MS to SL transition are optimized for 150 GHz and 220 GHz frequencies. The transition carries the signal that originates from a orthogonal mode transducer (OMT) followed by a CPW to MS transition and a T-network and eventually terminated to the MKID transmission line. The MS to SL transition has a band width of around 30 GHz for both the designs with a transmission coefficient of ~2dB and a reflection coefficient of around 16 dB.

The complete fabrication of the MKIDs will be done by collaborators at Berkeley once all other parts of the circuit are designed and optimized.

CHAPTER 4.

PART III

2DEG KINETIC INDUCTANCE WITH CO-PLANAR WAVEGUIDES – CIRCUIT MODELLING AND EXPERIMENTAL VERIFICATION

4.1 Background and Motivation

The collective oscillations of electrons called plasmons, in two-dimensional electron systems discovered more than 35 years ago [42] have recently gathered rigorous interest in the scientific community. The research interest is mainly driven in the direction of plugging the “THz gap” [43] which refers to a lack of detectors and sources in the terahertz (10^{12} Hz) region of the electromagnetic spectrum. Surface plasmons, which are electron oscillations propagating at the surface of the three dimensional bulk metal with a finite penetration depth are specially investigated in the field of photonics which takes advantage of the phenomenon of surface electrons travelling approximately 10 times slower than the free-space light velocity. This exhibits subwavelength confinement of light [44-47]. Surface plasmons in the skin of the bulk resonate at optical frequencies whereas the resonance of 2D electron systems such as semiconductor heterojunctions, graphene and 2D transition metals, falls in the gigahertz to far-infrared or the “THz gap”. The two-dimensional electron gas or two-dimensional plasmons are able to achieve greater subwavelength confinement [48-50] with velocities as low as 100 times slower than free-space velocity i.e. c/100 [49, 51]. Moreover, the resonance of the 2D plasmons or 2D electron gas (2DEG) can be easily manipulated by changing the electron density through an applied field effect. Such qualities of the 2DEG make an excellent candidate for high frequency detection and analysis [52 - 58].

However, to probe the electromagnetic radiation, there needs to be interaction between the gigahertz or THz photon and the 2DEG. A directly incident free-space radiation on a 2D electron system does couple. For any radiation photon to couple to a 2D electron system, the frequency and momentum of the photon and the 2D electron should be the same. The dispersion relation of a wave propagating on a surface can be briefly derived as follows,

$$E = E_0 e^{i(k_x x + k_z z - \omega t)} \tag{4.1}$$

E being the electric field of a propagating electromagnetic wave, k is the eave number, ω is the angular frequency of the wave travelling parallel to the y direction. Solving Maxwell's equation at a boundary of two different materials of permittivity ε_1 and ε_2 and using appropriate boundary conditions as follows,

$$\frac{k_{z1}}{\varepsilon_1} + \frac{k_{z2}}{\varepsilon_2} = 0 \tag{4.2}$$

and

$$k_x^2 + k_{zi}^2 = \varepsilon_i \left(\frac{\omega}{c}\right)^2 \tag{4.3}$$

where $i = 1, 2$ and c is the speed of light in vacuum, k_x remains same for the both the media at the surface for a surface wave. Solving with these boundary conditions, the dispersion relation for a wave propagating on the surface is,

$$k_x = \frac{\omega}{c} \sqrt{\frac{\varepsilon_1 \varepsilon_2}{\varepsilon_1 + \varepsilon_2}} \tag{4.4}$$

In a free electron model, the dielectric function is as follows,

$$\varepsilon(\omega) = 1 - \frac{\omega_P^2}{\omega^2} \tag{4.5}$$

where the bulk plasma frequency is

$$\omega_P = \sqrt{\frac{ne^2}{\varepsilon_0 m^*}} \tag{4.6}$$

Here *n* is the electron density, *e* is the charge on the electron, m^* is the effective mass of the electron and ε_0 is the permittivity of free-space. If we plot the relation of $\frac{\omega}{\omega_P}$ and k_x we get an asymptotic behavior [59] for higher values of k_x.

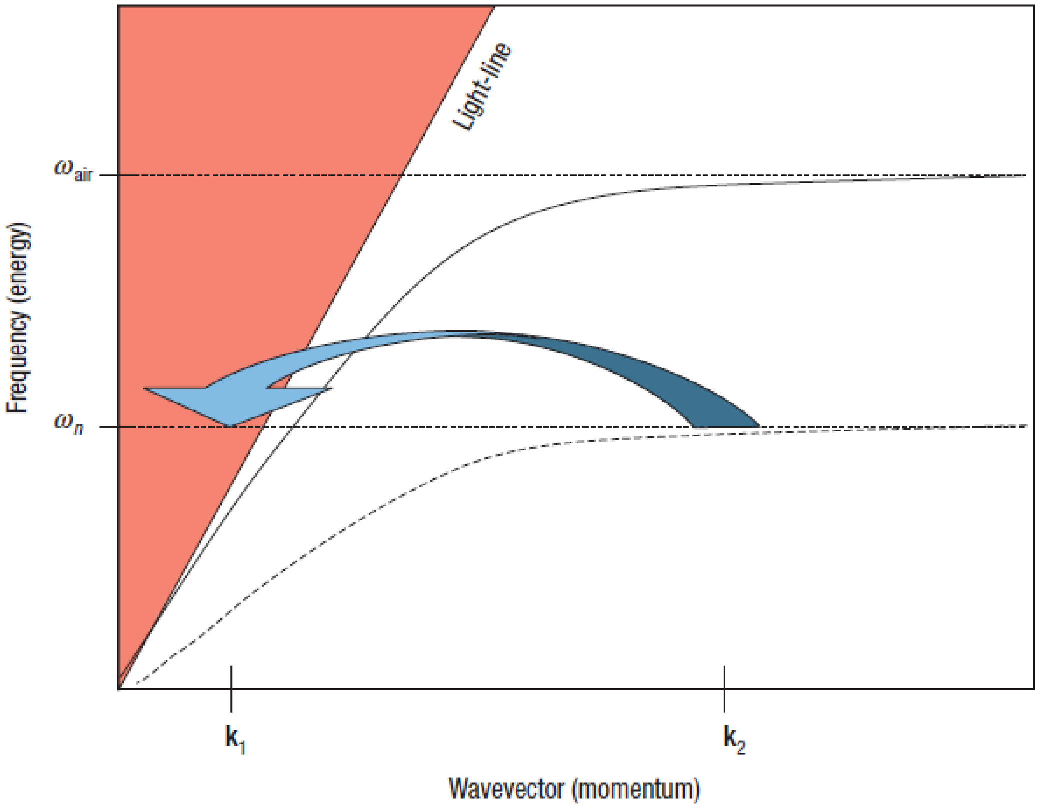

Figure 4.1. Dispersion relation of optical photons [59]

At lower values of k_x, the surface plasmons behave like a photon but as the k vector increases, the dispersion relation reaches an asymptotic limit called the "surface plasma frequency”. Figure. 4.1 shows a “light line” which indicates the dispersion relation of optical photons at $\omega = k_x c$. The dispersion of surface plasmons lies to the right of this line which indicates that the plasmons have a shorter wavelength than free-space radiation and the out-of-plane wave-vector of the surface plasmons is purely imaginary and exhibits evanescent decay. Thus the dispersion relation of surface plasmons can be given by

$$\omega_{SP} = \frac{\omega_P}{\sqrt{1+\varepsilon_2}} \tag{4.7}$$

Comparing the equations (4.4) & (4.7), the momentum of optical photons in free-space is less than the momentum of surface plasmons for the same energy. Since the surface plasma is a collective oscillation of free electrons and photons, the surface plasmons can be thought to have both of electrons and photons where the momentum of electrons is larger than that of the photons which causes the mismatch and prevents from light coupling directly into a 2D electron gas.

2D electron gas in heterojunction semiconductors are of a particular interest in the field of space exploration and Far-Infrared / THz or mm-wave astronomy. 2DEG hot electron bolometers operating at cryogenic temperatures are used to measure the cosmic microwave background (CMB) power at microwave frequencies. One way to couple electromagnetic energy into a 2D electronic system is to use planar antennas tuned to a particular band of frequency

4.2 Two-Dimensional Electron Systems

Electrons that can move freely in two dimensions *x* and *y* and whose momentum vectors are restricted in the third dimension *z* constitute a 2D electron system. 2D electron sheet densities can be found in band engineered heterojunction semiconductors, surface of liquid helium, graphene, inversion layer in a MOSFET etc. The research work in this thesis concerns with band engineered heterojunction semiconductor 2D electron systems, specifically $GaAs$ / $Al_xGa_{1-x}As$ heterojunction.

Abrupt changes in the conduction band energy level at a junction between two different semiconductors with mismatching bandgaps cause a formation of a deep discontinuity in the conduction band which forms a 2DEG. Figure 4.2 shows a conduction band profile of a $Al_xGa_{1-x}As$/GaAs heterojunction [60] with a silicon doped $Al_xGa_{1-x}As$.

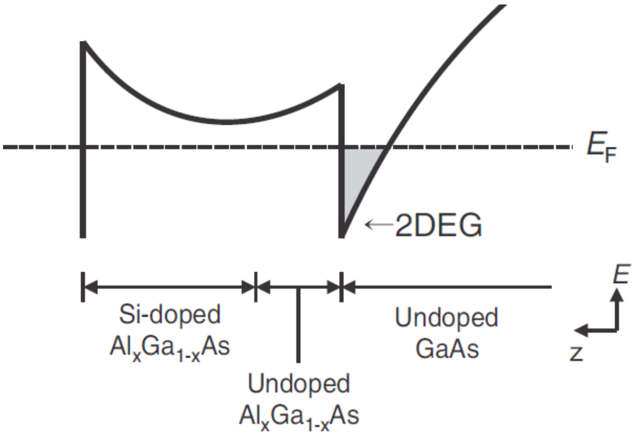

Figure 4.2. Conduction band of a Si-doped $Al_xGa_{1-x}As/GaAs$ heterojunction [60]

A quantum well structure is formed at the interface of the two mismatched III-V semiconductors. To allow the electrons to occupy only the lowest energy level in the *z* direction in the 2D well at the interface of $Al_xGa_{1-x}As$ and GaAs, the fermi level can be engineered by designing the silicon doping and the entire stack of materials. This will form a 2D electron sheet density in x and y direction along the heterojunction. This sheet density of electrons is approximately ~10nm inside the GaAs side of the junction and the conduction band energy of GaAs near the Γ point in the Brillouin zone (Figure 4.3) in momentum space can be given by

$$E(\vec{k}) = \frac{h^2 k^2}{8\pi^2 m^*} \tag{4.8}$$

where $k = |\vec{k}| = k_x^2 + k_y^2$ and $m^* \approx 0.067 m_e$ for GaAs where m_e is the mass of electron [60]. Both the momentum vector $\vec{k}$ and the conduction band energy $E(\vec{k})$ are relative to the Γ point.

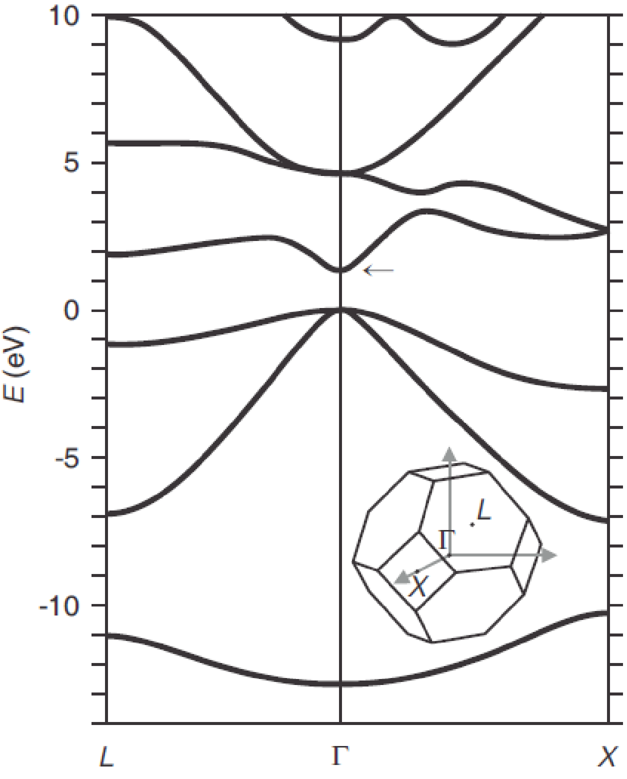

Figure 4.3 Band structure of GaAs with the Brillouin Zone inset [61]

4.3 Electron-Wave Interaction in 3D and 2D Electron Systems

Collective oscillations of electrons in bulk metals, due to inertia of the electrons and their Coulombic restoring forces of background positive charge consist of plasmonic oscillations. An electric field

$$\vec{E} = \frac{(en_{3D})}{\epsilon_0}\vec{x} \tag{4.9}$$

is created inside the bulk metal when the electron gas is shifted effectively from the equilibrium position by a displacement $\vec{x}$. The density of electrons n_{3D} is specifically for the case of bulk or 3D metals. The fermi wavenumber k_f is obtained by

$$n = \iint_{|\bar{k}| \le k_F} \frac{d^d\vec{k}}{(2\pi)^d} g \tag{4.10}$$

where *d* is the dimensionality, g is the spin and valley degeneracy. $E(\vec{k})$ has a value of *E_F* when $k = k_f$. The fermi velocity can be calculated as

$$\vartheta_F = \frac{2\pi}{h}\frac{\partial E}{\partial k}|_{k=k_F} \tag{4.11}$$

The density of state *D(E)*, representing the number of states per unit area or volume between E and $E + dE$ is obtained by

$$D(E) = \frac{d\bar{n}}{dE} \tag{4.12}$$

where

$$\bar{n}(E) = \iint_{E(\vec{k}) \le E} \frac{d^d\vec{k}}{(2\pi)^d} g \tag{4.13}$$

Therefore, the equation of motion for a unit volume of electrons inside the metal can then written as

$$(m^* n_{3D})\vec{x} = (-en_{3D})\vec{E} \tag{4.14}$$

or

$$\ddot{\vec{x}} = -\omega_P^2 \vec{x} \tag{4.15}$$

where $\omega_P^2 = n_{3D}e^2/m^*\epsilon_0$ is the plasma frequency. This collective oscillation of electron gas at angular frequency ω_P is typically in an optical frequency regime. The electric field inside a metal of a fairly large cross sectional area is given by $\vec{E} = (en_{3D}/\epsilon_0)\vec{x}$ which justifies the dispersion relation being flat at frequency ω_P. Here, purely longitudinal modes in the plasma that satisfy $\vec{k} \times \vec{E} = \omega\vec{B} = 0$ Maxwell equations are consider so as to distinguish from the transverse electromagnetic mode in 3D metal above ω_P which will have a dispersion relation of the form $\omega^2 = \omega_P^2 + \omega^2 c^2$ corresponding to a dielectric constant of $1 - (\omega_P^2/\omega^2)$. Along the direction of the surface, a hybrid mode of the electromagnetic radiation and the 3D plasmonic oscillation exists because an oblique TM wave has a longitudinal electric field component along the direction of the surface which couples the electromagnetic wave and the 3D plasmonic oscillation at the surface of the metal. Since the transverse electromagnetic wave decays exponentially inside the bulk of the metal, it only propagates in a frequency dependent depth called the penetration depth δ from the surface of the metal. The low frequency dispersion nature of this transverse wave is almost as same as an electromagnetic wave but as its frequency approaches a surface plasmon resonance frequency, which is closely related to ω_P, the dispersion nature significantly differs that of light dispersion. Near this frequency, the wave propagates at a velocity much slower than light and exhibits sub-wavelength confinement with reduced wavelength which opens up a whole new chapter of research called photonics.

In a 2D electron system, since the electrons poses inertia and also a Coulombic restoration force, the 2D conductor can also support plasmonic waves although the dispersion of these waves appears at much lower frequencies compared to the surface plasmonic waves, typically 10^{10} Hz (GHz) to 10^{12} Hz (Tera-hertz or THz). Moreover, 2D plasmonic waves can achieve greater subwavelength confinement with velocities going as low as *c*/100 [49-51]. Throughout this chapter, the terms 2D plasmonics and 2D electron gas (2DEG) are used interchangibly.

Following sections will go through the characteristics of plasmonic waves in a 2D electronic system and exploits this plasmonic behavior of the 2D electron systems by geometrically coupling electromagnetic waves of GHz frequencies to the 2DEG and make efforts in formulating a circuit model of a co-planar waveguide with a 2DEG system backed by experimental verification.

4.4 Circuit Modelling of 2D Electron Gas

The kinetic energy of the collectively oscillating electrons is accounted by the kinetic inductance which is of non-magnetic origin while on the other hand the electric potential energy due to the Coulombic restoration force which drives electrons into plasmonic oscillation can be modelled as an electrical capacitance. Electron degeneracy pressure also exerts a restoring force acting upon the disturbed equilibrium of electron density distribution which can be modelled as a quantum capacitance. Now, since the 2DEG is spread as a sheet of electrons at the junction, the overall circuit model (Figure 4.4) of the 2D plasmonic medium [62] will consist of a distributed kinetic inductance

L_k per unit length, a distributed total capacitance consisting of geometric and electrical capacitances C_c and a quantum capacitance C_q

$$C = \left(\frac{1}{C_C} + \frac{1}{C_q}\right)^{-1} \tag{4.16}$$

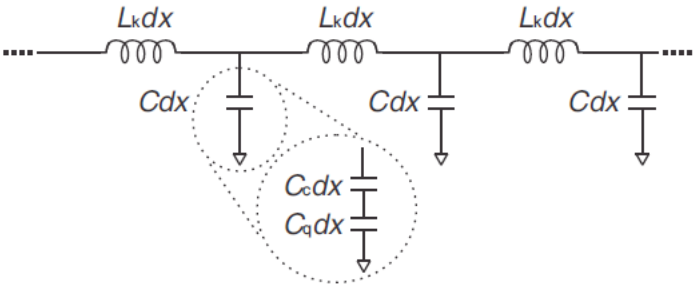

Figure 4.4 Transmission line model of a 2DEG without any loss

A lossy transmission line model, not shown here, will have an additional distributed resistance that relates to different loss mechanisms such phonon scattering, fringing etc. For a gate nearby the 2DEG, it will act as the ground in the transmission line model. For an ungated 2DEG, the ground is the potential of free space away from the 2DEG. The difference between an ordinary transmission line and a plasmonic transmission line will be that the kinetic inductance will dominate the later. So in the plasmonic case, the phase velocity will be given by $\vartheta_P = 1/\sqrt{L_k C}$ which corresponds to the plasmonic dispersion relation.

4.4.1 Kinetic Inductance L_k

The kinetic inductance accounts for the kinetic energy of the collective oscillations of electrons in the 2D plasmonic medium. The following section on kinetic inductance in a semiconductor heterojunction has been mostly derived from [63], [64] and [65]. As discussed in [63], the kinetic inductance L_k can be calculated in a 2D electron system such as $GaAs/Al_xGa_{1-x}As$ heterojunction 2DEG with a classical approach as follows.

Consider a strip of 2DEG or a 2D conductor with width W and length l applied with a time varying electric potential $V(t)$ to induce an electric field $V(t)/l$. No spatial variation of the electric field is considered here to keep the derivation simple. By Newton's equation, the inertial acceleration for an electron is

$$-e\frac{V}{l} = m^*\frac{dv}{dt} \tag{4.17}$$

where v is the velocity of electron and m* is the effective mass of electron ($m^* = 0.0067m_0$ for GaAs). The current due to electron's velocity is $I = -n_0evW$, n_0 being the conduction electron density. Also, if we Fourier transform the expression (4.17), the frequency dependent relation would be

$$-e\frac{V}{l} = i\omega m^* v \tag{4.18}$$

Therefore, the impedance obtained would be

$$\frac{V}{I} = i\omega\frac{m^*}{n_0e^2}\frac{l}{W} \tag{4.19}$$

This leads us to the kinetic inductance per unit length given by

$$L_k = \frac{m^*}{n_0e^2}.\frac{l}{W} \tag{4.20}$$

For a 2DEG, the total kinetic energy E_{total} of the electrons with velocity v can be expressed as $E_{total} = \frac{1}{2}.m^*v^2n_0Wl$. With the total current being $I = -n_0evW$, the E_{total} can also be written as

$$E_{total} = \frac{1}{2}.(L_k l)I^2 \tag{4.21}$$

where L_k being the kinetic inductance per unit length and $L_k l$ being the total kinetic inductance.

Alternately, the derivation in [63] for L_k proceeds by calculating the total kinetic energy first and then the current I in the k-space or the electron wavenumber space. A 2D fermi disk with radius k_F with center lying on the k-space origin is considered which shifts towards the positive k_F-axis with application of an electric field pointing in the negative x-axis, along the length of the 2D conductor. This shift in the 2D fermi disk increases the total kinetic energy and produces a current I. Figure. 4.5 indicates the shift of the 2D fermi disk of $\Delta k \ll k_F$ when a negative pointing electric field is applied [63].

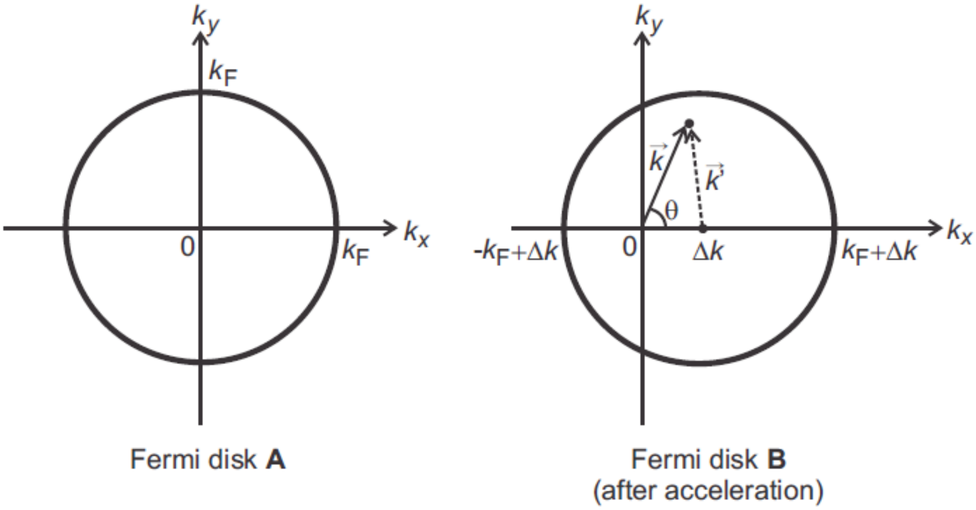

Figure 4.5 Shift of fermi disc in k-space due to an electric field [63]

Therefore, the total increase in kinetic energy per unit area is,

$$\frac{E_{total}}{Wl} = \iint_B \frac{d^2\vec{k}}{(2\pi)^2} gE(\vec{k}) - \iint_A \frac{d^2\vec{k}}{(2\pi)^2} gE(\vec{k}) \tag{4.22}$$

where g is for spin and valley degeneracy (g=2 for $GaAs/Al_xGa_{1-x}As$ 2DEGs) and $E(\vec{k}) = \frac{\bar{h}^2k^2}{2m^*}$ is the energy of an electron with wavevector $\vec{k}$. The first integration in equation (4.22), where $\overrightarrow{k'} = \vec{k} - \Delta k\hat{e}k_x$, where $\hat{e}k_x$ is the unit vector in the k_x direction which is calculated as

$$\begin{aligned} \iint_B \frac{d^2\vec{k}}{(2\pi)^2} gE(\vec{k}) &= \frac{g\bar{h}}{8\pi^2m^*} \iint_B d^2\vec{k}'\left|\vec{k}' + \Delta k\hat{e}k_x\right|^2 \\ &= \frac{g\bar{h}^2}{8\pi^2m^*} \iint_B d^2\bar{k}'[k'^2 + 2k'_x\Delta k + (\Delta k)^2] \end{aligned} \tag{4.23}$$

Now the total kinetic energy per unit area of the Fermi disk A is the same as the first term of the rightmost expression in equation (4.23) which is $\frac{g\bar{h}^2}{8\pi^2m^*} \iint_B d^2\bar{k}'[k'^2]$ and so it will cancel out the that term in (4.22). For the second term, because of the odd symmetry of k'_x in disc B, Δk term vanishes reducing the (4.22) integration to

$$\frac{E_{total}}{Wl} = \frac{g\bar{h}^2}{8\pi^2m^*}(\Delta k)^2 \iint_B d^2\vec{k}' = \frac{g\bar{h}^2k_F^2}{8\pi m^*}(\Delta k)^2 \tag{4.24}$$

From which the total current calculated is

$$I = W \iint_B \frac{d^2\vec{k}}{(2\pi)^2} gev_x(\vec{k}) \tag{4.25}$$

where $v_x(\vec{k}) = \frac{\bar{h}k_x}{m^*}$ is the x-component of the velocity of an electron with $\vec{k}$ as the wavevector. Therefore,

$$I = \frac{Wge\bar{h}}{4\pi^2m^*} \iint_B d^2\vec{k}k_x = \frac{Wge\bar{h}}{4\pi^2m^*} \int_0^{2\pi} d\theta \cos\theta \int_0^{k_F+\Delta\cos\theta} k^2dk \tag{4.26}$$

where the radius of disc B is $k_F + \Delta k$ and the distance between the origin and the edge of disc B at an angle θ is $k_F + \Delta k \cos\theta$, assuming $\Delta k \ll k_F$. Integrating up to first order Δk terms, the current obtained is

$$I = \frac{Wge\hbar k_F^2}{4\pi m^*}\Delta k \tag{4.27}$$

Substituting I from (4.27) into (4.24) and $k_F^2 = \frac{4\pi n_0}{g}$,

$$E_{total} = \frac{1}{2}\left[\frac{m^*}{n_0 e^2}.\frac{l}{W}\right]I^2 \tag{4.28}$$

which is the same as (4.21) where L_k is given by 4.(20).

This kinetic induced current I is related to the total energy E_{total} and voltage V similar to the relation between the magnetic inductance and voltage i.e.

$$V = \frac{(L_k l)dI}{dt} \tag{4.29}$$

and

$$E_{total} = \int_{t_0}^{t} VIdt = \frac{1}{2}(L_k l)I^2 \tag{4.30}$$

where t_0 is the time when the electron gas is at rest. It is also worth to be noted that the kinetic inductance opposes the change in momentum of electron just as magnetic inductance opposes change in magnetic flux.

4.4.2 Capacitance of 2DEG

The total capacitance in a 2DEG or a 2D plasmonic transmission line consists of a geometrical capacitance per unit length and a quantum capacitance per unit length.

The energy in the total capacitance can be thought to be distributed to add a unit charge on the 2DEG electron sheet density or a remainder of the kinetic energy of the electrons. Following topics elucidate the origins of the two capacitances viz. geometrical and quantum capacitance.

4.4.3 Quantum Capacitance

The kinetic inductance L_k represented the increase in kinetic energy of a fixed number of electrons due to their movement. However, the quantum capacitance C_q represents the addition of an extra unit charge to the 2DEG to increase the total kinetic energy. Therefore, C_q increases with increase in the density of states $D(E)$ at the Fermi surface. The quantum capacitance given in [66] is

$$C_q = e^2 D(E_F) W \tag{4.31}$$

The electron degeneracy pressure due to the addition of any electron into the system and thus needing to occupy Fermi level above because of Pauli's exclusion principle leads to a restoring force is accounted for by the quantum capacitance. For a GaAs/AlGaAs 2DEG system, the quantum capacitance can be given by

$$C_q = \frac{g m^* e^2}{2\pi \hbar^2} W \tag{4.32}$$

where m^* is the effective mass of electron ($m^* = 0.0067 m_0$ for GaAs) and g represents spin and valley degeneracy. Equation (4.32) can also be written as

$$C_q = \frac{g e^2 k_F}{2\pi \hbar v_F} W \tag{4.33}$$

4.4.4 Geometric Capacitance

The Coulombic attraction in a plasmonic oscillating wave of electrons accounts for the geometric capacitance C_c. The geometric capacitance also depends on the surrounding medium in which the plasmonic oscillations exist. For a 2D conductor with no surrounding conductors and with width W, the geometric capacitance C_c [68] is,

$$C_c = 2\kappa\epsilon_0 k_P W \tag{4.34}$$

where k_P is the plasmonic wavenumber and κ is the effective dielectric constant of surrounding media.

The presence of an external conductor or a gate alters the geometrical capacitance C_c. For a distance of d between the fate and the 2DEG and assuming distance d is much smaller than the plasmonic wavelength i.e. $k_P d \ll 1$, then the parallel plate capacitance per unit length becomes

$$C_c = \frac{\kappa\epsilon_0 W}{d} \tag{4.35}$$

4.5 Transmission Line Theory of 2D plasmonic waves

Now that we have obtained the geometrical capacitance C_c, quantum capacitance C_q and the kinetic inductance L_k which compose of the distributed components of a transmission line, we can formulate transmission characteristics of a 2D plasmonic system.

From the telegrapher's equation [69] & [70] that give partial differential equations that relate the induced voltage to time rate-of-change of current through inductance and the induced current to the time rate-of-change of voltage to the capacitance,

$$\frac{\partial V}{\partial x} = -L\frac{\partial I}{\partial t} \tag{4.36}$$

and

$$\frac{\partial I}{\partial x} = -C\frac{\partial V}{\partial t} \tag{4.37}$$

we can obtain the potential energy $V(x)$ and current $I(x)$ in the transmission line model as

$$\frac{d^2V(x)}{dx^2} - \gamma^2 V(x) = 0 \tag{4.38}$$

$$\frac{d^2I(x)}{dx^2} - \gamma^2 I(x) = 0 \tag{4.39}$$

where

$$\gamma \equiv \alpha + ik_P = i\omega\sqrt{L_k C} \tag{4.40}$$

is the complex propagation constant with α being the attenuation and k_P representing the plasmonic wavenumber. equation (4.40) essentially is the plasmonic dispersion relating k_P and ω. General solutions for the equations (4.38) & (4.39) are

$$V(x) = V_0^+ e^{-\gamma x} + V_0^- e^{\gamma x} \tag{4.41}$$

$$I(x) = I_0^+ e^{-\gamma x} + I_0^- e^{\gamma x} \tag{4.42}$$

Here, the $e^{-\gamma x}$ term indicates the propagation of the wave in the positive x direction whereas the $e^{\gamma x}$ term represents the wave propagating in the negative direction. The characteristic impedance of the line can now be given by,

$$Z_0 = \sqrt{\frac{L}{C}} = \frac{V_0^+}{I_0^+} = -\frac{V_0^-}{I_0^-} \tag{4.43}$$

2DEG electronic systems may often have an external conductor nearby or are "gated" which affects the overall capacitance and causes change in the dispersion relation of the 2D plasmonic waves. Following sections briefly explain the two cases viz. gated and ungated 2DEG electronic systems.

4.5.1 Gated 2DEG Electronic Systems

As introduced in geometrical capacitance section, for a 2DEG with a nearby conductor or a gate at distance d from the 2DEG which is much smaller than the plasmonic wavelength (i.e. $k_P l \ll 1$) the angular frequency can be given by

$$\omega = \sqrt{\frac{ge^2 k_F d}{4\pi\kappa\epsilon_0 \hbar v_F} + \frac{1}{2} v_F k_P} \tag{4.44}$$

In equation (4.44), the term $\frac{1}{2} v_F k_P$ represents the quantum capacitance and $\frac{ge^2 k_F d}{4\pi\kappa\epsilon_0 \hbar v_F}$ represents the geometrical capacitance which as seen depends on the distance between the gate and the 2DEG. In the case of geometrical capacitance, expression in the first bracket of $\left(\frac{ge^2}{\kappa 4\pi\epsilon_0 \hbar v_F}\right)(k_F d)$ is typically of the order of 1. However the amplitude of the second bracket is determined by the distance d and the electron density i.e. $k_F = 4\pi n_0/g$, g being the spin and valley degeneracy. For typical values of n_0 i.e. 10^{12} cm^{-2} the distance d is ~5nm for $k_F d = 1$ which means the quantum capacitance or the electron degeneracy pressure dominates for distances ~ < 5nm. For a semiconductor heterostructure such as $GaAs/Al_xGa_{1-x}As$ used this thesis, the distance d is ~135 nm, which makes it difficult for 2D plasmonic waves to propagate dominated by quantum capacitance. Therefore, we can approximate the dispersion relation (4.44) to be

$$\omega = \sqrt{\frac{ge^2 k_F d}{4\pi\kappa\epsilon_0 \bar{h} v_F}}\, v_F k_P \tag{4.45}$$

4.5.2 Ungated 2DEG Electronic Systems

In equation (4.20), if we substitute $m^* = \bar{h}k_F/v_F$, then the equation of kinetic inductance L_k can be written as

$$L_k = \frac{4\pi\bar{h}}{ge^2 v_F k_F}\frac{1}{W} \tag{4.46}$$

For a $GaAs/Al_xGa_{1-x}As$ heterojunction with no conductors nearby, we can write the following dispersion relation combining equations (4.34), (4.40), (4.43) and (4.46). can be written

$$\omega = v_F k_F \sqrt{\frac{ge^2}{8\pi\kappa\epsilon_0 \bar{h} v_F}\left(\frac{k_P}{k_F}\right) + \frac{1}{2}\left(\frac{k_P}{k_F}\right)^2} \tag{4.47}$$

In the right hand side of equation (4.47), the first term originated from the geometric capacitance and the second term from the quantum capacitance. For k_p smaller than k_F, then the first term dominates since the coefficient of the first term is of the order of 1. For k_P larger that k_F, the second term dominates. For low frequencies i.e. long-wavelengths, the effect of the quantum capacitance is negligible and the dispersion relation (4.47) is approximated as [49], [51], [62], [63],

$$\omega = \sqrt{\frac{ge^2 v_F k_F}{8\pi\kappa\epsilon_0\bar{h}}\, k_P} \tag{4.48}$$

This dispersion relation is illustrated in Figure 4.6.

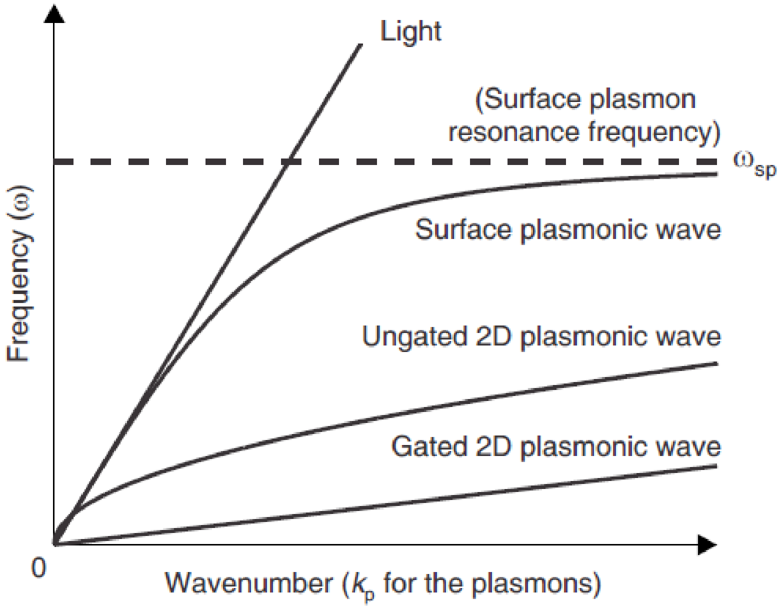

Figure 4.6 Comparison of dispersion relations light, surface plasmonic waves, gated and ungated 2D plasmonic waves. The 2D plasmonic waves appear at much lower frequencies around GHz. [64]

In the regime where Coulombic force is strong, the gated 2DEG has a much low slope compared to the ungated 2DEG which means at the same frequency, the gated 2D plasmonic wave exhibits much shorter wavelength with much slower phase velocity compared to the ungated since the gate shortens the range of Coulombic interactions in the 2D conductor.

4.6 Momentum Relaxation/Scattering Time in a 2DEG

Electron scattering in the 2DEG accumulate to give a per-unit-length resistance R, and can be added in series to the kinetic inductance L_k as shown in the transmission line circuit model in Figure 4.7.

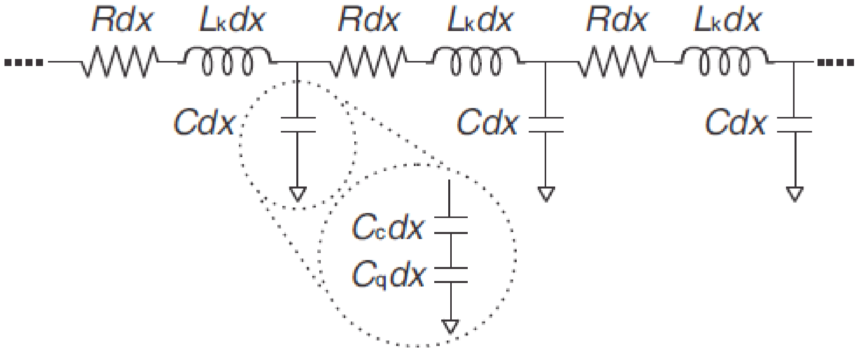

Figure 4.7 Lossy transmission line model of 2DEG [65]

The resistance per square in a 2DEG is given as follows

$$R_{sq} = \frac{m^*}{n_e e^2 \tau} \tag{4.49}$$

where m^* is the effective mass of electron, n_e is the 2D electron density in the 2DEG and τ is the momentum relaxation/scattering time. The kinetic inductance can be related to R_{sq} as follows

$$L_{k/sqr} = R_{sq}\tau = \frac{m^*}{n_e e^2} \tag{4.50}$$

The momentum scattering time τ is affected by a number of scattering mechanisms such as impurity scattering, acoustic and optical phonon scattering, defect scattering etc. The defect and impurity scattering has low temperature dependence as compared to phonon scattering. Cumulatively, the total momentum scattering time is as follows

$$\frac{1}{\tau} = \frac{1}{\tau_{impurity}} + \frac{1}{\tau_{defect}} + \frac{1}{\tau_{acoustic}} + \frac{1}{\tau_{optical}} + \cdots \qquad (4.51)$$

which means the overall momentum scattering time will be dominated with the shortest individual scattering mechanism. The momentum relaxation time of the $GaAs/Al_xGa_{1-x}As$ wafers used in this thesis is ~76 ps at 4.2 K [71]

4.7 Proposed Circuit Model for 2DEG-Co-planar waveguide coupling

The research work done for this thesis in the field of 2DEG focuses mainly on formulating, simulating and experimentally verifying the effect of 2DEG coupling to co-planar waveguide structures and capacitive coupling structure fabricated on a $GaAs/Al_{0.3}Ga_{0.7}As$ heterojunction semiconductors. Following sections will elaborate more on the proposed circuit models and discuss simulation results and experimental verifications.

4.7.1 Capacitively coupled 2DEG Contacts.

Burke (1999) [62] measured the real and imaginary conductivity $\sigma(k = 0, \omega)$ of a high mobility two dimensional electron gas system at frequecnies below and above the momentum scattering time and also observed that the imaginary part of the 2DEG impedance is inductive suggesting a kinetic inductance. Their research work also proposes a transmission line model of a 2DEG capacitively coupled to an Al Schottky barrier gate separated by 500 nm from the 2DEG (Figure 4.8). However, their measurements are limited to 2.5 GHz and do not convey any high frequency behavior.

We attempt here this thesis to verify the 2DEG circuit model theoretically and experimentally by designing and testing a capacitively coupled 2DEG.

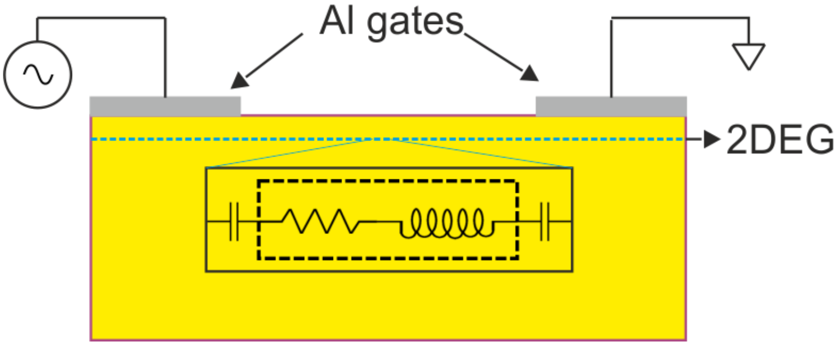

Figure 4.8 Al Schottky barrier capacitively coupled to a 2DEG with a proposed circuit model as in Burke (1999).

The $GaAs/Al_xGa_{1-x}As$ heterojunction stack used here is illustrated in Figure 4.9. The quantum well exists between the 40 nm AlGaAs layer and GaAs layer below it. The AlGaAs is doped with $1 \times 10^{12}\ cm^{-2}$ 1δ Silicon doping at the interface of AlGaAs and GaAs. A mesa structure of height ~200 nm is etched out so that the quantum well where the 2DEG exists is only in the mesa structure. 250 nm thick Al contacts are deposited in a pattern to form the capacitively coupled 2DEG over the mesa.

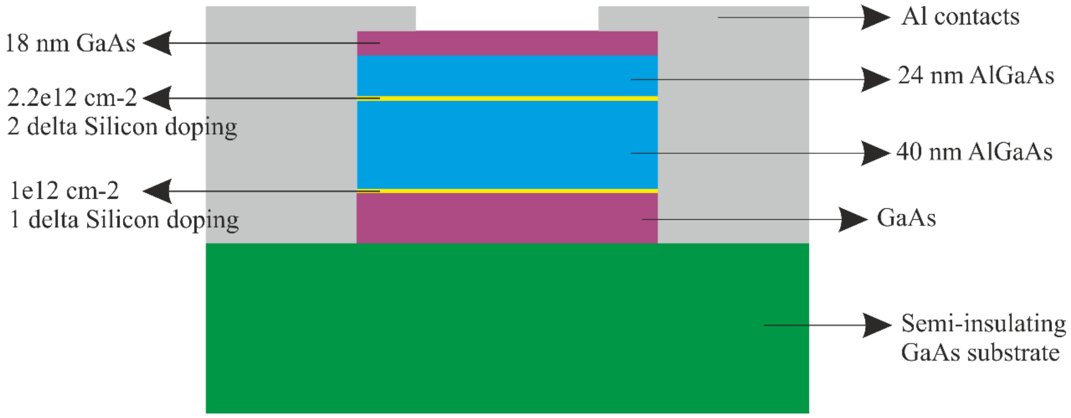

Figure 4.9 $GaAs/Al_xGa_{1-x}As$ heterojunction stack

The structure of the capacitively coupled 2DEG is shown in Figure 4.10. The capacitively coupled 2DEG is formed between two Al contacts (250 nm thick) over the mesa (~200 nm thick) and the 2DEG is approximately 122 nm below the surface of the mesa. The etched mesa is approximately 100 µm x 300 µm wide.

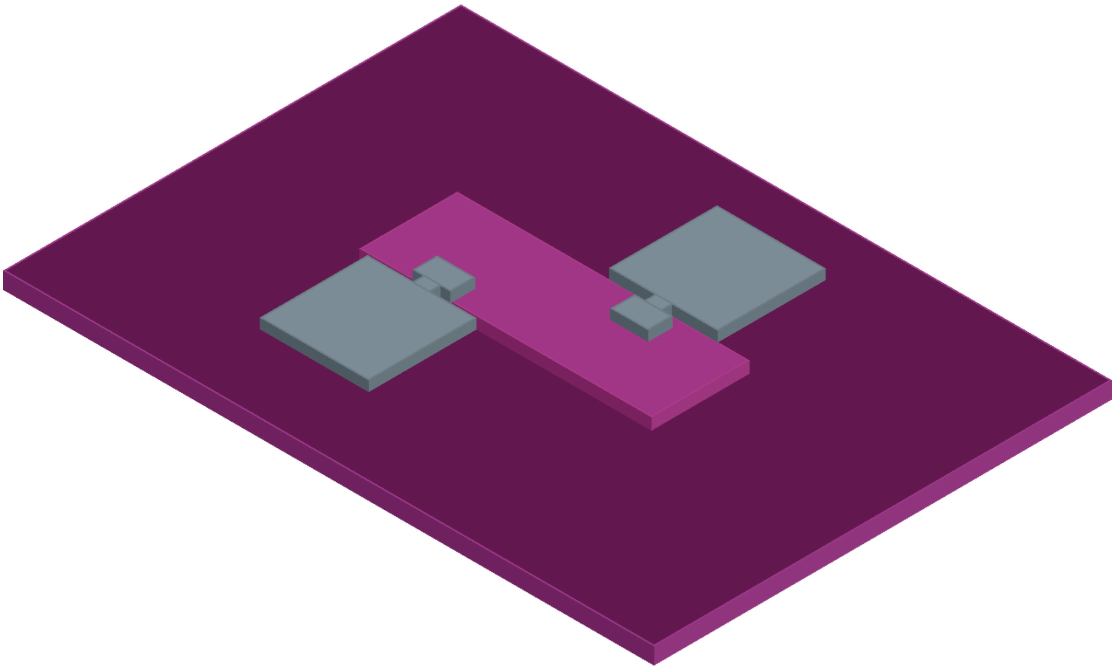

Figure 4.10 Capacitively coupled 2DEG structure

The 2DEG was simulated in Sonnet Suites by assigning a metal sheet 1.76 nH/square as a starting estimate of the kinetic inductance. Variations in the metal contact dimensions were simulated to obtain the transmission and reflection parameters of the capacitively coupled 2DEG. Figure 4.11 illustrates the dimensions of the structure where the parameter W_1 is varied. Figure 4.12 and Figure 4.13 show the transmission (S21) and reflection (S11) parameters with variations in W_1.

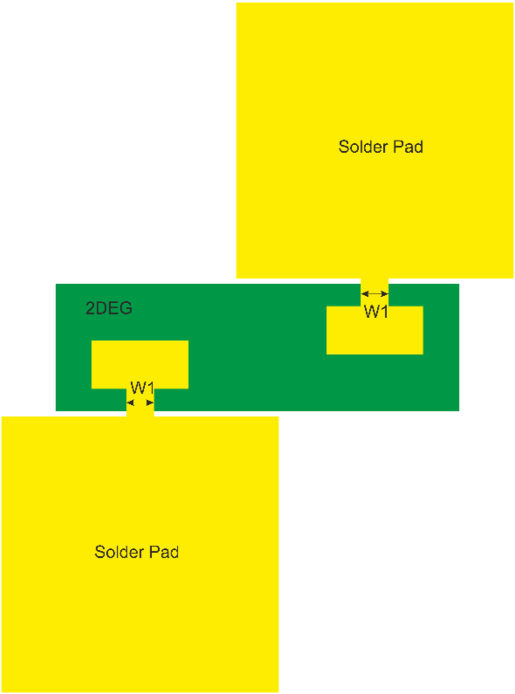

Figure 4.11 Circuit layout of the structure

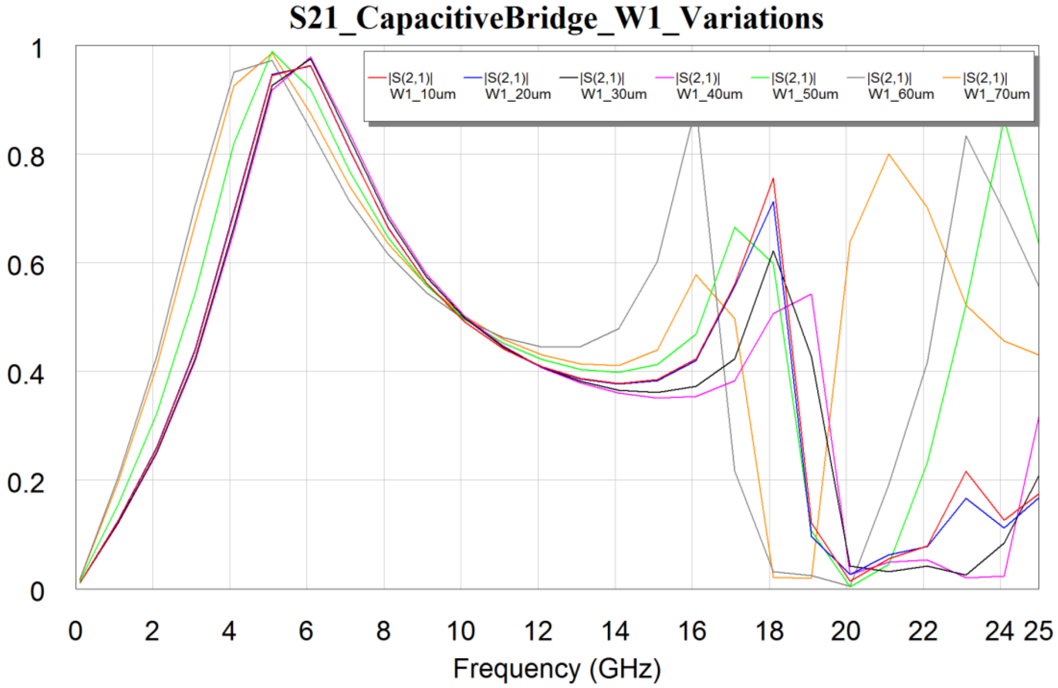

Figure 4.12 Transmission coefficient (S21) of the capacitively coupled 2DEG with variations in W_1

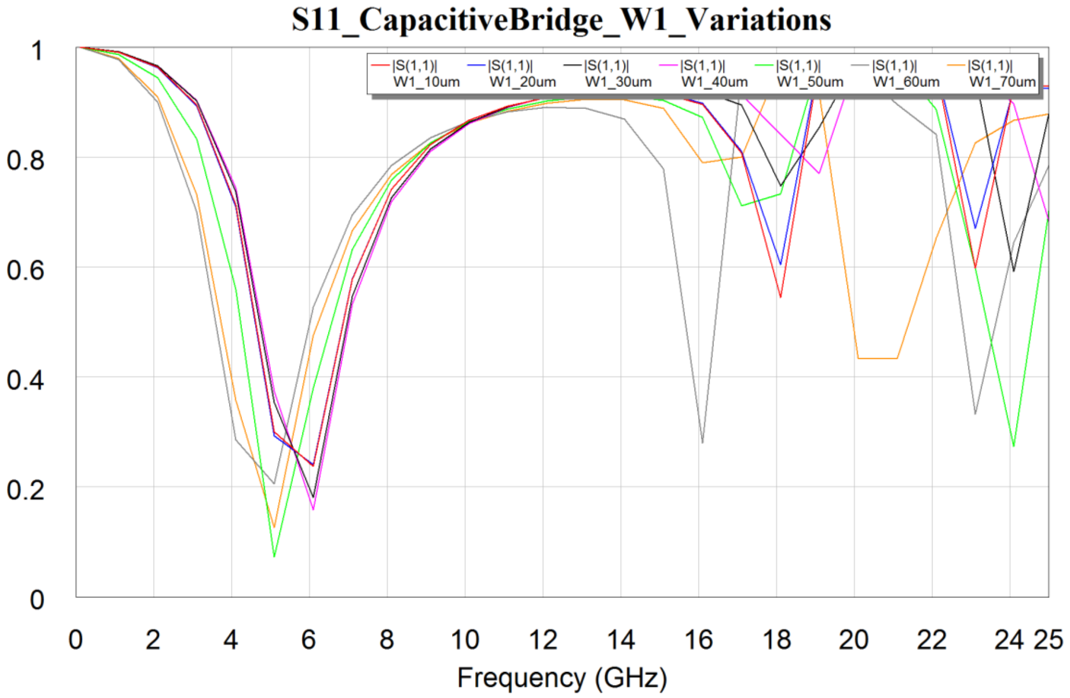

Figure 4.13 Reflection coefficient (S11) of the capacitively coupled 2DEG with variations in W_1

From the simulations we observe that as the parameter W_1 increases, the peak resonance frequency shift down in frequency This can be accounted for by the increasing capacitance because of the increasing plate area and since $\omega = 1/\sqrt{LC}$.

4.8 Fabrication Process

The capacitvely coupled 2DEG is fabricated here at ASU at the CSSER clean room facility. A number of steps are involved in fabricating the chip that include two layer photo-lithography, $GaAs/Al_xGa_{1-x}As$ etching, aluminum etching etc. All the steps of fabrication are illustrated in Figure 4.14. Many of the etching recipes were needed to be optimized to have accurate control over the depth of the mesa. The

$GaAs/Al_xGa_{1-x}As$ heterojunction was wet etched in a solution of Hydrogen Peroxide (H_2O_2), Phosphoric Acide (H_3PO_4) and water in a ratio of 1:1:38 [72] for 60 sec to obtain a rate of ~200 nm per minute.

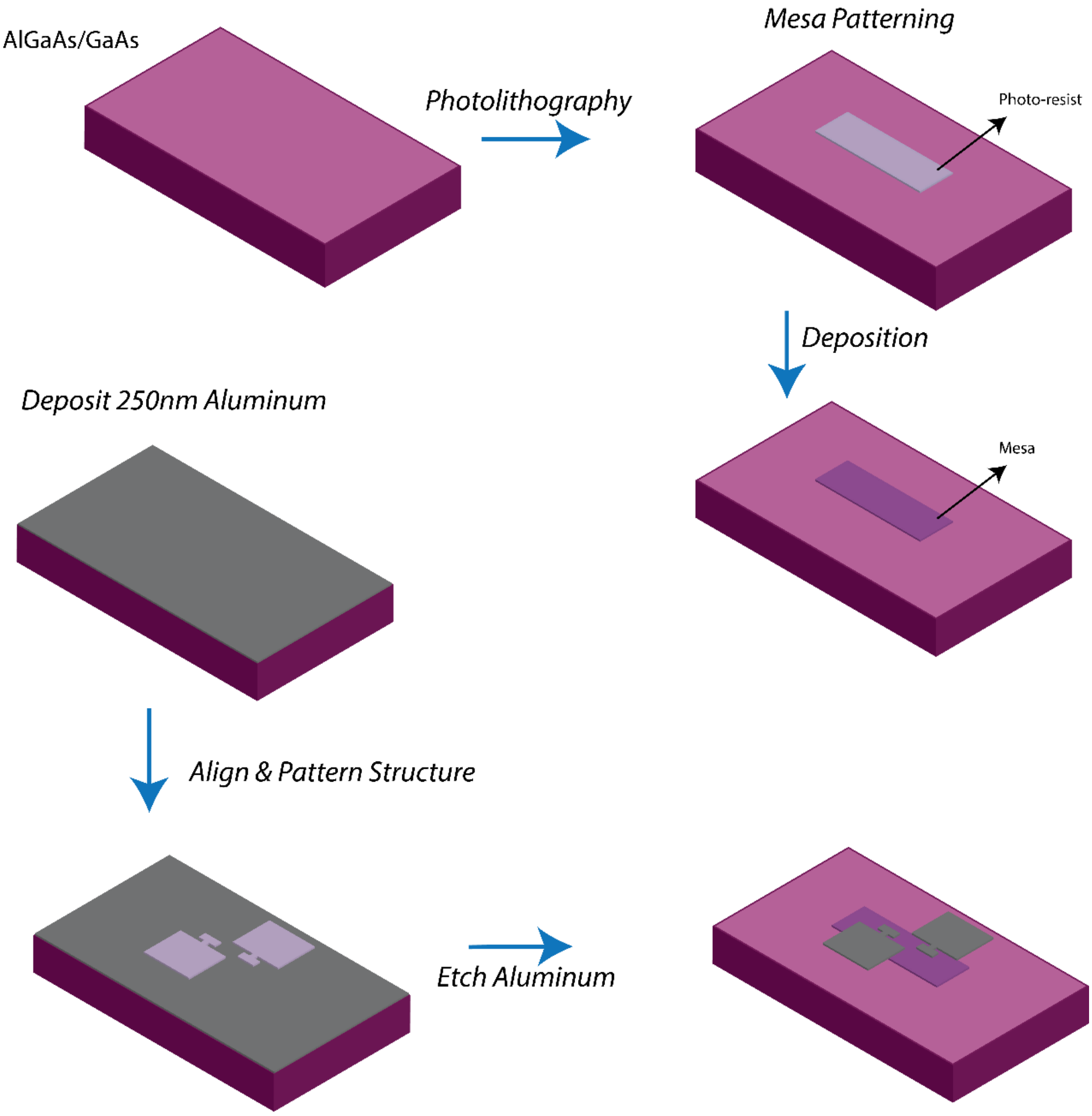

Figure 4.14 Steps involved in fabricating the capacitively coupled 2DEG

4.9 Experimental Procedure

The capacitively coupled 2DEG chip is mounted in a microwave package that is calibrated for up to 24 GHz. Inside the microwave package, the chip is wire bonded to 50 Ω microstrip lines that are soldered to the SMA input and output ports of the package (Figure 4.15).

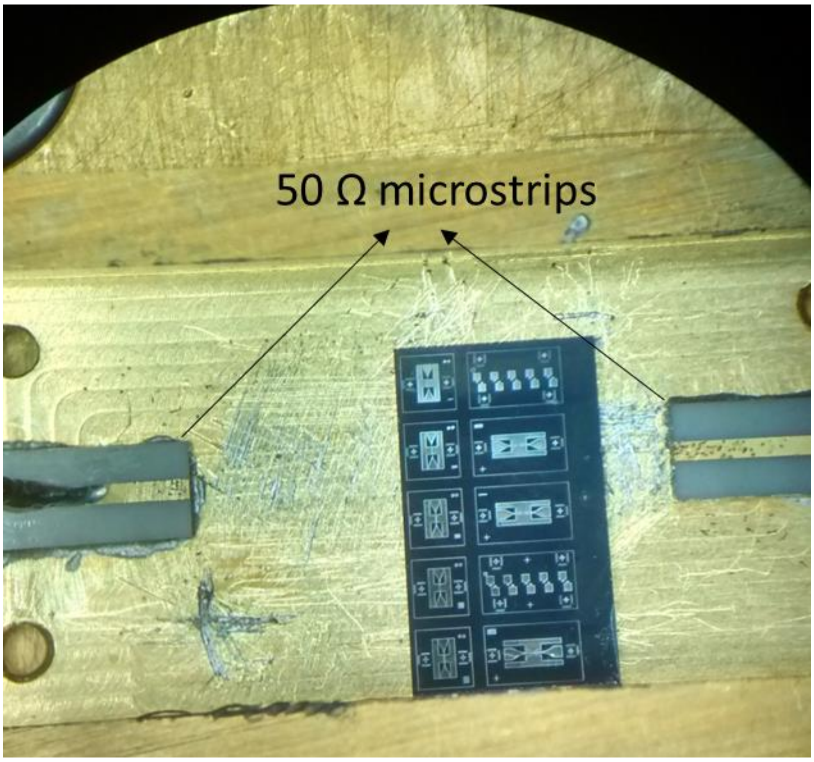

Figure 4.15 Capcitively coupled 2DEG chip connected to input and output 50 Ω microstrips.

A UV led that operates at low temperatures is also fitted inside the package in order to photo-dope the $GaAs/Al_xGa_{1-x}As$ quantum well so as to increase the electron density in the 2DEG. High frequency cables are connected to a Vector Network Analyzer (VNA) that feed the signal to the input and output SMA ports of the package housing the chip (Figure 4.16). Transmission measurements are performed at 77 K and 10 K using a bath of liquid nitrogen and a cryostat respectively.

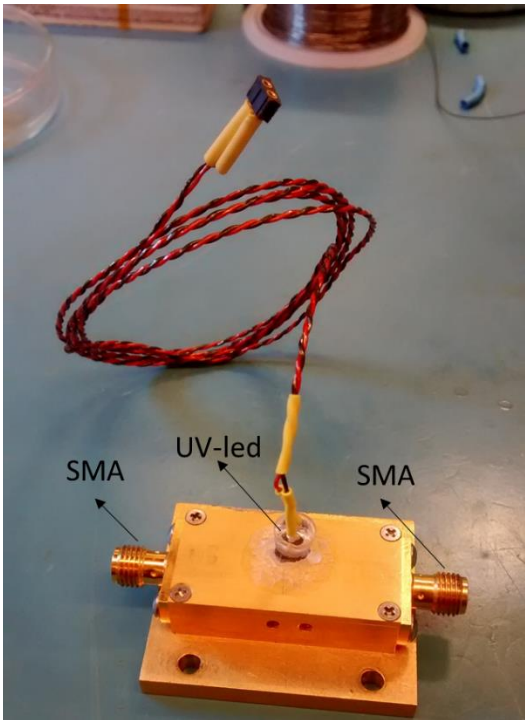

Figure 4.16 Package with UV led and input & output SMA connections housing the chip

Figure 4.17 Calibration unit for calibrating the baseline transmission and reflection of the high frequency cables.

The cables are calibrated using standard calibration equipment (Figure 4.17). The microwave package is dipped in to a bath of liquid nitrogen (77 K) as shown in Figure 4.19. The dip probes used for the 77 K measurements (Figure 4.18) are also calibrated with the calibration unit. For a 10 K measurement, the package is mounted in an ultra-high vacuum cryostat (Figure 4.20) designed in the lab. The package is also fitted with a UV-led to photo dope the GaAs/AlGaAs heterojunction and inject electrons into the 2DEG.

Figure 4.18 Dip probes attached to the microwave package housing the chip

Figure 4.19 Package dipped in liquid nitrogen at 77 K

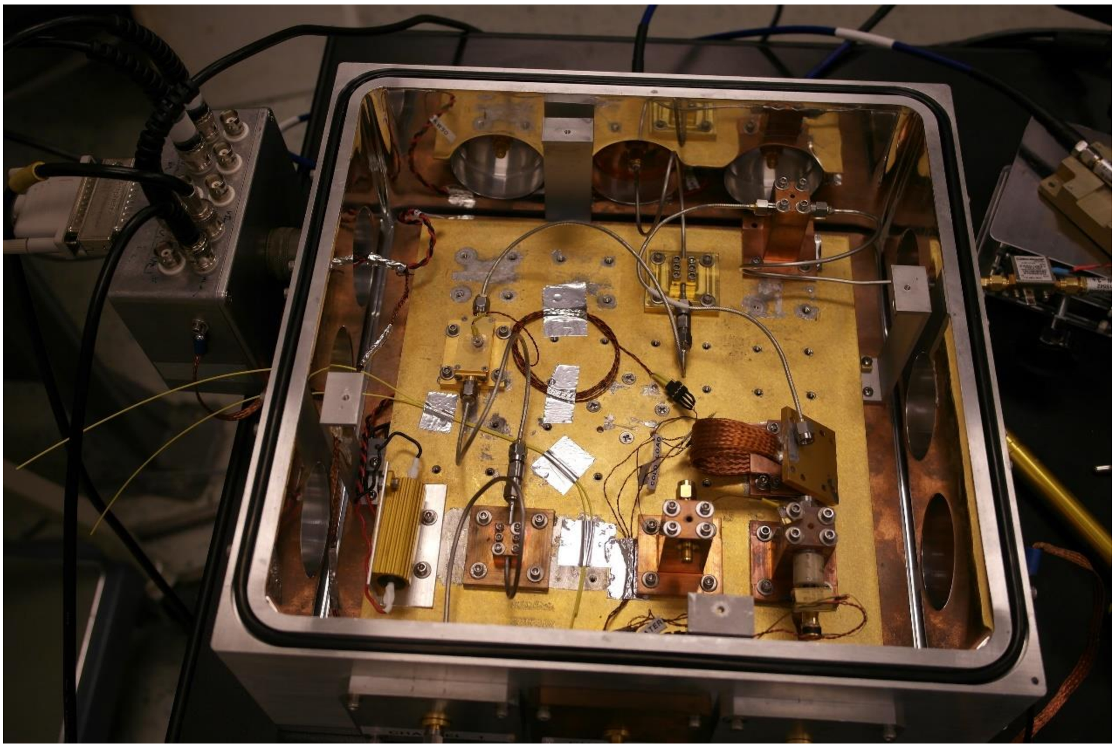

Figure 4.20 10 K ultra-high vacuum cryostat

4.10 Experimentation Results

We have obtained preliminary results of the transmission and reflection coefficients of a capacitively coupled 2DEG with W_1 = 20 μm at room temperature, 77K and 10 K. The nature of the s-parameters is the same as simulations by the observation of the peak of transmission that lies in the same range of frequencies as the simulated s-parameters. The nature of the results is also similar to the one observed by Burke (1999) which gives us confidence in the working of the 2DEG circuit model. Figure 4.21 to 4.24 show plots of the experimentally observed transmission and reflection coefficients of experiments done at 77 K and 10 K. In both of the experiments, the intensity of the UV-led is gradually increased to increase the photo doping. S-parameters are recorded for a number of intensities of the UV-led. In the 77 K case, the transmission decreases as the intensity of the UV-led is increased which might indicate that photo-carriers are still being generated in the GaAs/AlGaAs heterojunction and a total freeze out has not occurred. While for 10 K measurements we observe that after a certain intensity of the UV-led, there is no change in the transmission characteristics indicating that the 2DEG is saturated with electrons and there is a freeze out in rest of the semiconductor.

Low temperature (77 K and 10 K) transmission characteristics were measured for a variation of two values of W_1. As explained earlier through simulations that increasing W_1 leads to downward shift in the resonance frequency, from the illustrations in Figures 4.25 & 4.26 that show the transmission characteristics of a capacitive coupled 2DEG with $W_1 = 100$ μm, it is clearly the case.

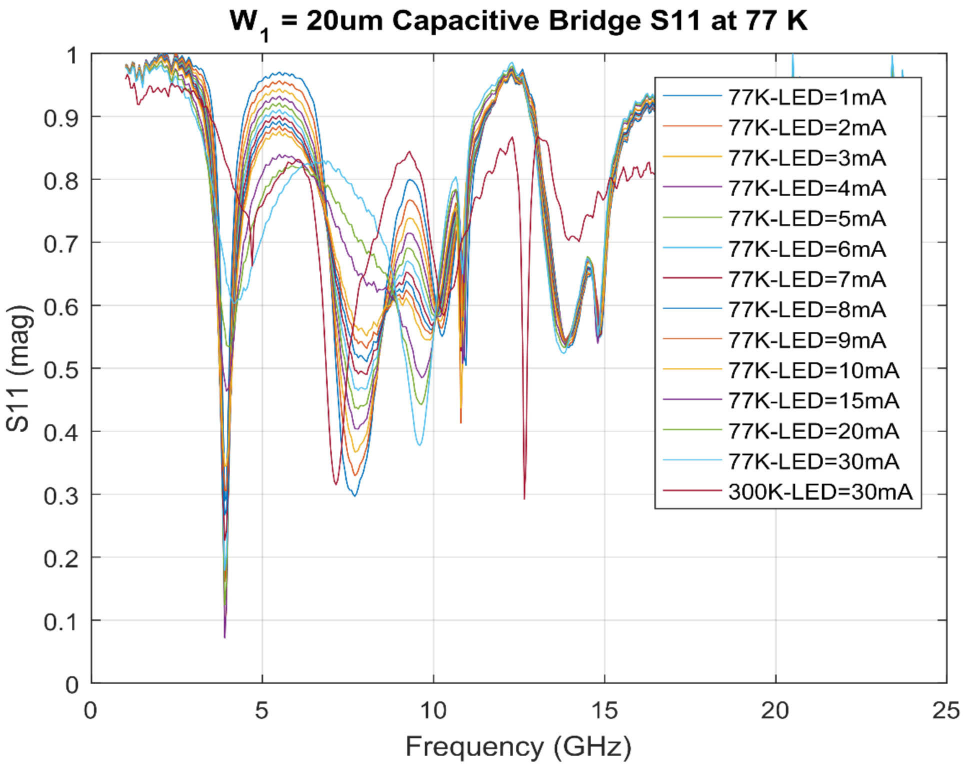

Figure 4.21 Reflection coefficient of W_1=20 µm capacitively coupled 2DEG at 77 K

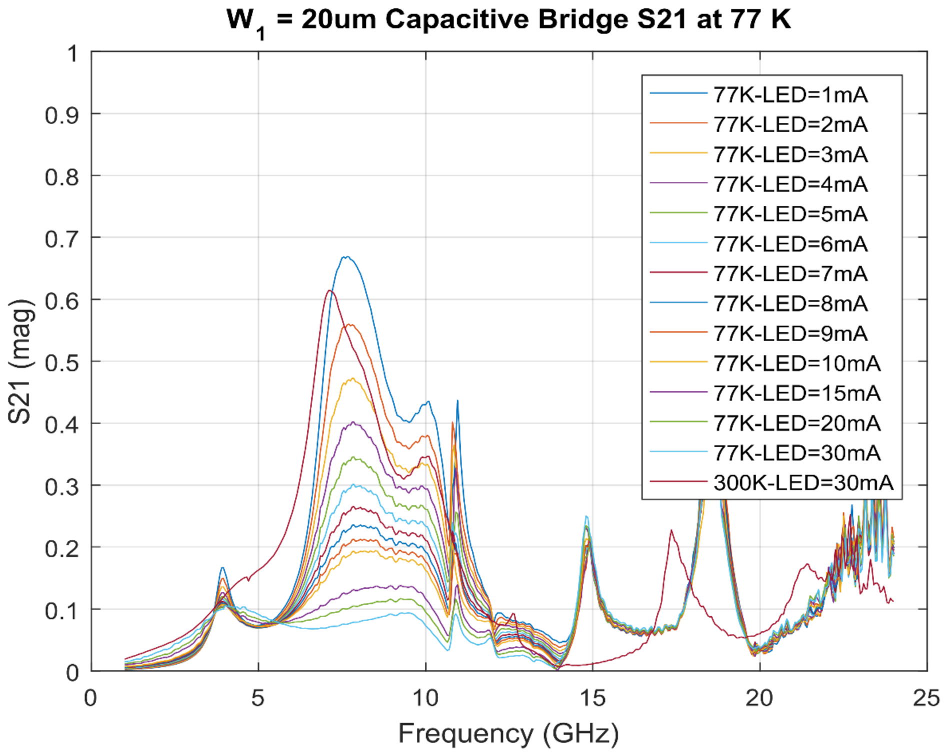

Figure 4.22 Transmission coefficient of W_1=20 µm capacitively coupled 2DEG at 77 K

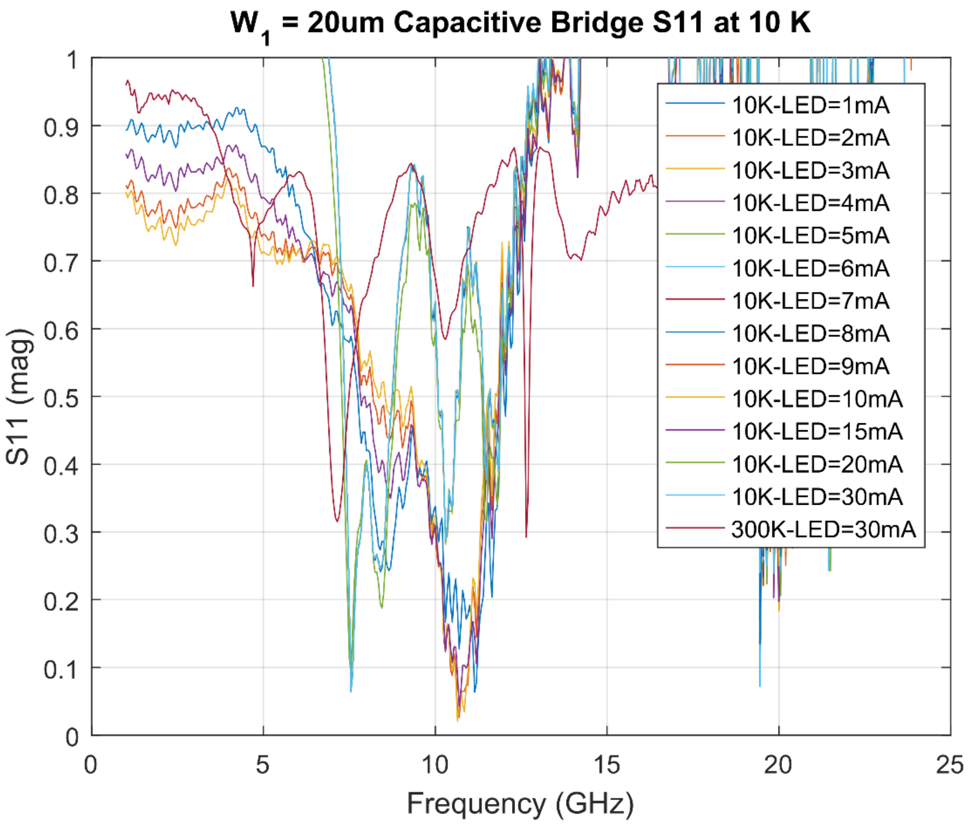

Figure 4.23 Reflection coefficient of W_1=20 µm capacitively coupled 2DEG at 10 K

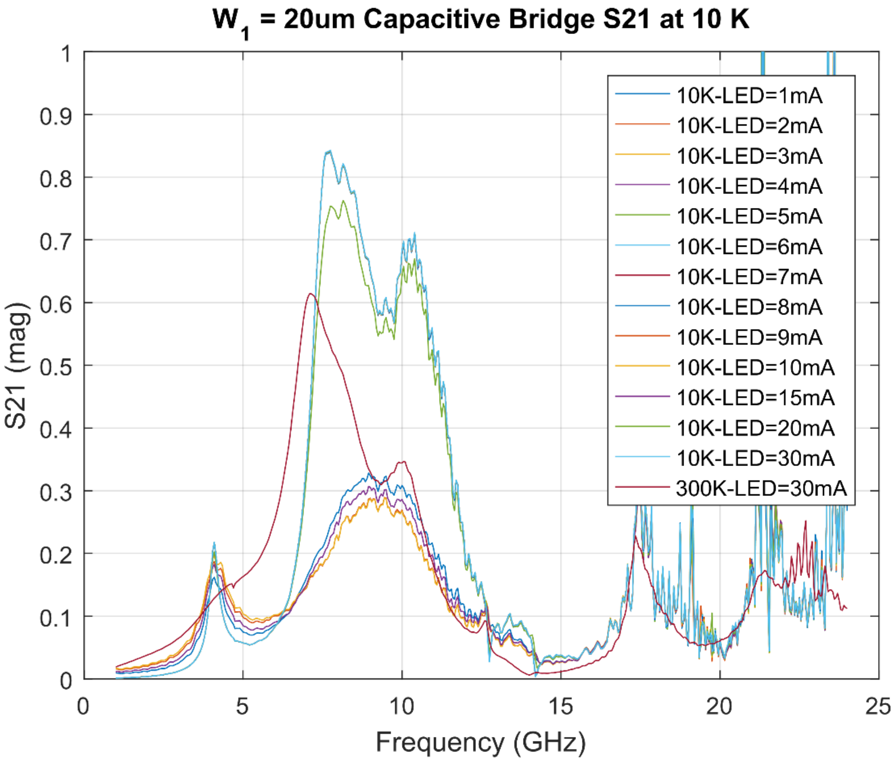

Figure 4.24 Transmission coefficient of W_1=20 µm capacitively coupled 2DEG at 10 K

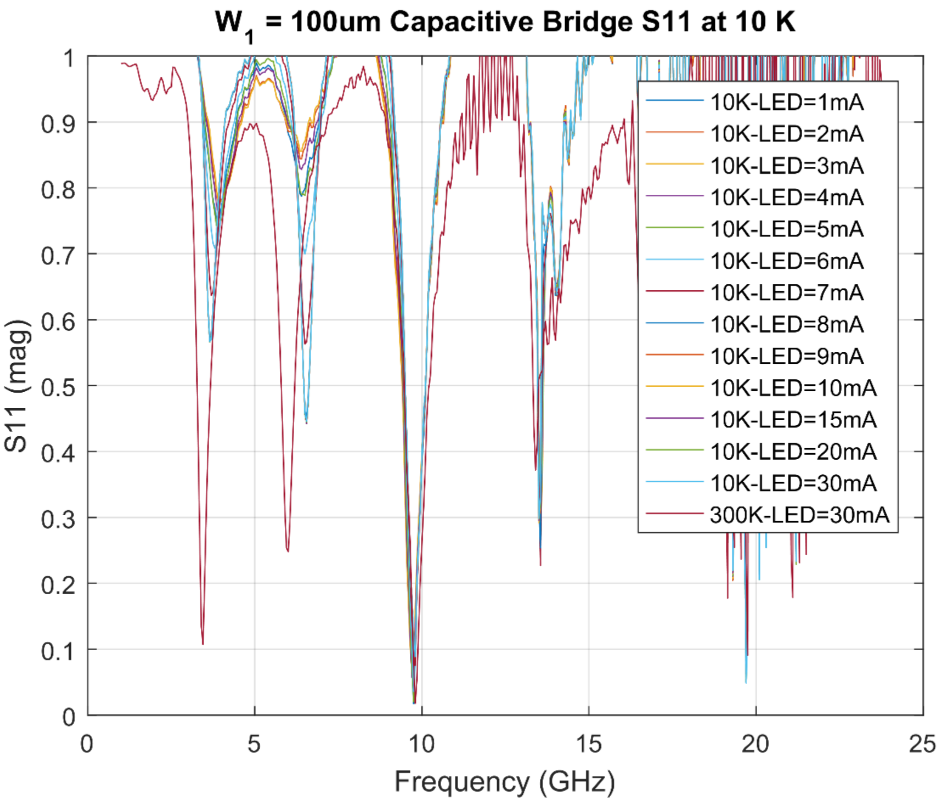

Figure 4.25 Reflection coefficient of W_1=100 µm capacitively coupled 2DEG at 10 K

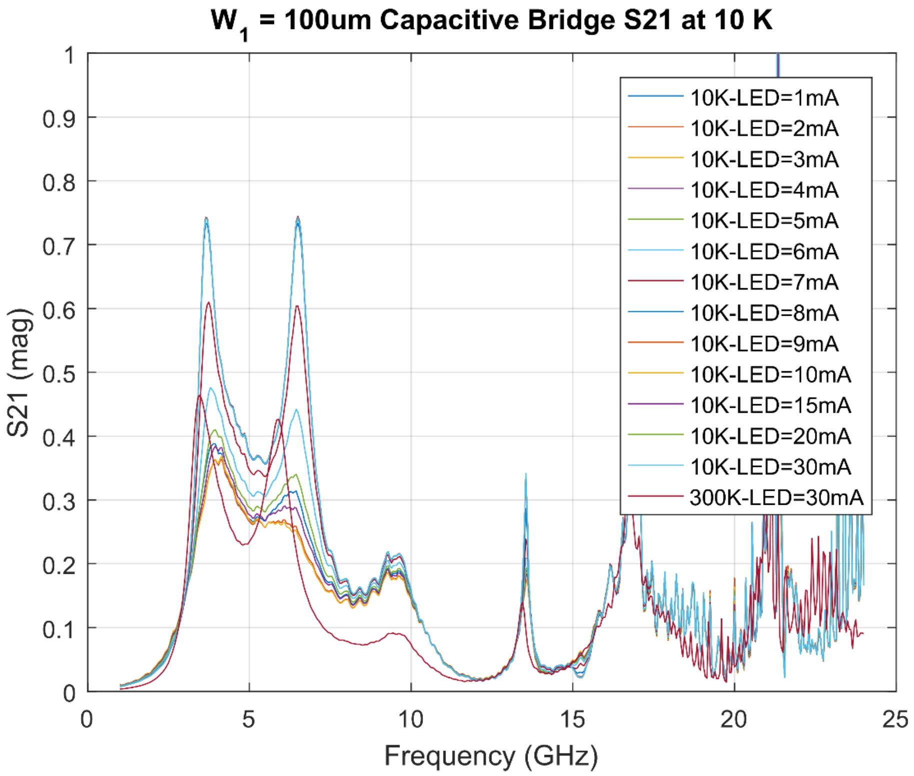

Figure 4.26 Transmission coefficient of W_1=100 µm capacitively coupled 2DEG at 10 K

4.11 Proposed 2DEG-CPW Coupling

We further investigate circuit modeling of 2DEG coupled co-planar structures by theorizing and simulating a 2DEG coupled co-planar waveguide structure. The 2DEG-cpw structure is based on the same principles of the capacitively coupled 2DEG structure in the sense that the CPW transmission line is atop a mesa structure which contains the 2DEG underneath it.

The CPW is designed to be 3 μm wide with two ground planes placed 3 μm apart from the center line. In transmit signal through the 3 μm center line, a broader solder pad needs to be placed before and after it. To minimize the reflection losses in the CPW-solder pad structure, a Klopfenstein taper structure transitions the 3 μm center line to a 200 μm solder pad (Figure 4.27). The Klopfenstein taper was chosen in order to obtain minimum reflection coefficient at maximum bandwidth and minimum length of the tapering structure [73]. The 2DEG is etched out of a 200 μm × 50 μm mesa structure, just as in the case of the capacitively coupled 2DEG.

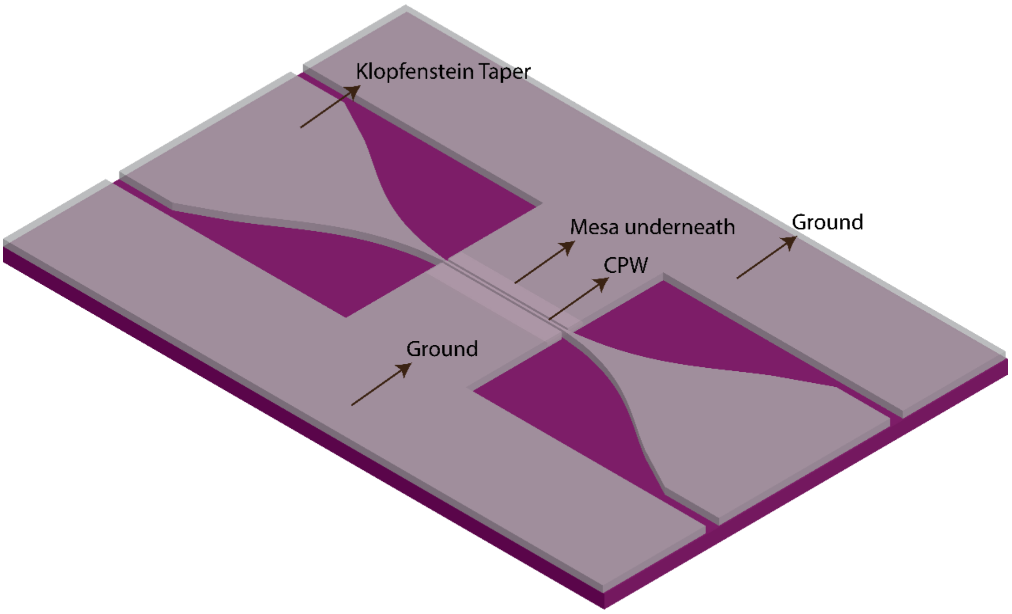

Figure 4.27 2DEG coupled CPW structure

We propose that the CPW transmission will be coupled to the 2DEG via capacitances as shown in Figure 4.28. The distributed kinetic inductance L_k of the 2DEG along with the 2DEG capacitance C_{2d} essentially forms a LC circuit along with the geometric capacitance of the CPW center line. The geometric capacitance C_g capacitively couples the 2DEG with the ground planes of the CPW.

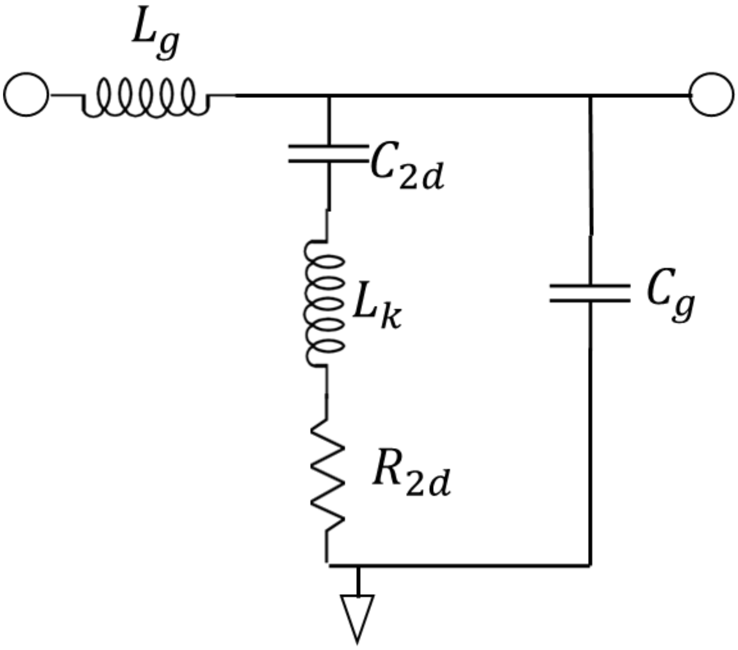

Figure 4.28 Proposed circuit model of the 2DEG-cpw structure

Sonnet simulations were performed on the 2DEG-cpw structure with an initial estimate of the distributed kinetic inductance of $L_k = 1.76\ \mathrm{nH/m}$. We observe distinct rise and dips in the reflection coefficient S11 and the transmission parameter S21 respectively, that may correspond to the resonance frequency of the LC circuit as shown in Figure 4.29. The circuit model can be analytically formulated to estimate the values of the kinetic inductance L_k, 2DEG capacitance C_{2d} and the geometric capacitance C_g, as done in the following subsection.

4.11.1 2DEG-CPW Analytical Formulation

Assuming a lossy LC circuit with a distributed 2DEG resistance R throughout the 2DEG, we can write the total impedance of the 2DEG-CPW circuit model as follows

$$Z_0 = \sqrt{\frac{i\omega L_g}{Z_{//}}} \tag{4.52}$$

where $Z_{//}$ is the impedance of the parallel LC circuit that comprises the distributed kinetic inductance, C_{2d}, distributed resistance R and the geometric capacitance C_g (Figure 4.29).

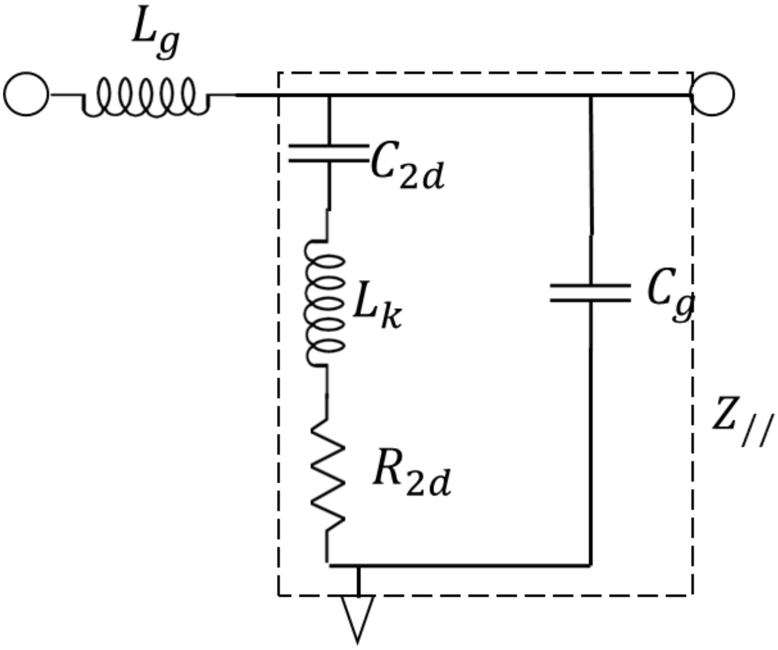

Figure 4.29 Total impedance of the 2DEG-CPW circuit model

The $Z_{//}$ can be evaluated as

$$Z_{//} = \sqrt{i\omega C_g + \frac{1}{i\omega(L_k + R) + \frac{1}{i\omega C_{2d}}}} \tag{4.53}$$

Therefore the total impedance Z_0 becomes,

$$Z_0 = \sqrt{\frac{L_g}{C_g}\left(\frac{\frac{1}{C_g} - \omega^2 L_k + i\omega R}{\frac{1}{C_{2d}} + \frac{1}{C_g} - \omega^2 L_k + i\omega R}\right)} \tag{4.54}$$

Z_0 can be analyzed for zeroes for the condition when the numerator is zero and poles when denominator is zero, as follows

$$\frac{1}{C_g} - \omega^2 L_k + i\omega R = 0 \tag{4.55}$$

$$\therefore \left(\frac{1}{C_{2d}} - \omega^2 L_k\right)^2 = -\omega^2 R^2 \tag{4.56}$$

$$\therefore\ \omega^2 = -\frac{1}{2}\left(\frac{R^2 - 2L_k}{L_k^2 C_g} \pm \sqrt{\left(\frac{R^2 - 2L_k}{L_k^2 C_g}\right)^2 - \frac{4}{C_{2d}^2 L_k^2}}\right) \tag{4.57}$$

The poles of Z_0 are when

$$\frac{1}{C_{2d}} + \frac{1}{C_g} - \omega^2 L_k + i\omega R = 0 \tag{4.58}$$

$$\therefore \left(\frac{1}{C_{2d}} + \frac{1}{C_g}\right)^2 - \left(2\omega^2 L_k\left(\frac{1}{C_{2d}} + \frac{1}{C_g}\right)\right) + \omega^4 L_k^2 = -\omega^2 R^2 \tag{4.59}$$

$$\begin{aligned} \omega^2 = -\frac{1}{2}\Bigg(&\left(R^2 - 2L_k\left(\frac{1}{C_{2d}} + \frac{1}{L_g}\right)\right) \\ &\pm \sqrt{\left(R^2 - 2L_k\left(\frac{1}{C_{2d}} + \frac{1}{C_g}\right)\right)^2 - 4L_k^2\left(\frac{1}{C_{2d}} + \frac{1}{C_g}\right)^2}\Bigg) \end{aligned} \tag{4.60}$$

The 2DEG-CPW impedance Z_0 along with load and input impedances can be visualized as a transmission line as shown in Figure 4.30. For such a transmission line, the input and load impedance are related by the propagation constant γ as follows

$$Z_{in} = \frac{Z_0(Z_l + Z_0 \tanh(\gamma l))}{Z_0 + Z_l \tanh(\gamma l)} \tag{4.61}$$

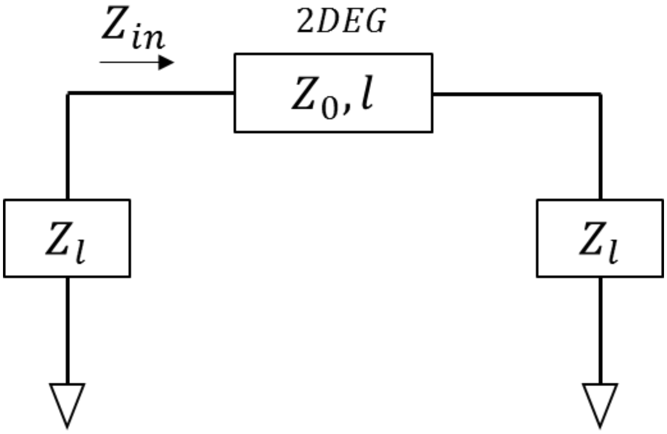

Figure 4.30 2DEG-CPW with load and input impedances

If we consider a lossless 2DEG (R = 0) that is terminated with a load impedance Z_l, the total impedance can be written as

$$Z_0 = Z_l \sqrt{\frac{1 - \omega^2 L_k C_{2d}}{1 - \omega^2 L_k \left(\frac{C_g C_{2d}}{C_g + C_{2d}}\right)}} \tag{4.62}$$

Simulations were performed with variations in the value of kinetic inductance per square (L_k) in the 2DEG so as to extract out the geometric inductance L_g and geometric capacitance C_g. From equation (4.62), we can say that for when Z_0 becomes zero i.e. when

$$1 - \omega^2 L_k C_{2d} = 0 \tag{4.63}$$

or

$$\omega_1^2 = \frac{1}{L_k C_{2d}} \tag{4.64}$$

and when Z_0 becomes infinity when

$$1 - \omega^2 L_k \left(\frac{C_g C_{2d}}{C_g + C_{2d}} \right) = 0 \tag{4.65}$$

or

$$\omega_2^2 = \frac{C_g + C_{2d}}{L_k C_g C_{2d}} \tag{4.66}$$

Therefore the transmission through the 2DEG-CPW will be zero when Z_0 is infinite or when Z_0 is zero. Hence, ω_1 and ω_2 correspond to first and second minima of the transmission coefficient. In the simulations with the 2DEG, transmission and reflection coefficients are observed at these frequencies for varying values of kinetic inductance per square as shown in Figure 4.31. From equations (4.64) and (4.66), the ratio of the two frequencies ω_1 and ω_2 gives a relation between C_g and C_{2d} as follows

$$\frac{\omega_2^2}{\omega_1^2} = \frac{C_g + C_{2d}}{C_g} \tag{4.67}$$

$$\therefore \ \omega_2 = \omega_1 \sqrt{\frac{C_g + C_{2d}}{C_g}} \tag{4.68}$$

From equations (4.64) or (4.66), we can also infer that the product $\omega\sqrt{L_k}$ is constant for a given dimension of 2DEG. Therefore, in order to verify this hypothesis, we note the values of different resonant frequencies for various values of kinetic inductance per square and observe their product to be almost constant. The simulated values of ω_1 & ω_2 for various L_k are shown in Table 4.1.

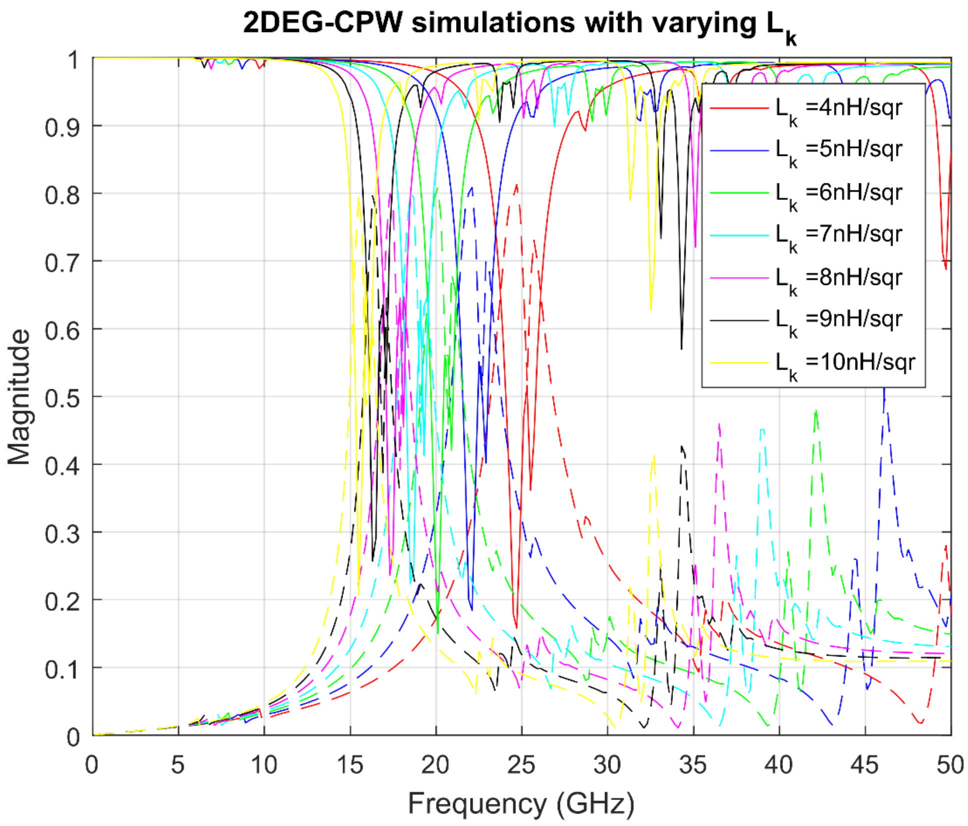

Figure 4.31 Simulations of 2DEG-CPW structure with varying L_k. Solid lines indicate the transmission coefficient S21 and dashed lines indicate reflection coefficient S11

Using Keysight's ADS simulation software, we estimate the electrical length βl of the 3 µm wide and 3µm ground spaced CPW in degrees as 6.285^o.Now since, $\beta l = \omega l/v$, for a frequency of 10 GHz, we have the following expression

$$6.285^o = \frac{2\pi 10^{10} \times 200 \times 10^{-6}}{v} \tag{4.69}$$

from which we can extract v as $1.1455 \times 10^8\ m/s$. Now since $v = 1/\sqrt{LC}$, we can write

$$\frac{1}{\sqrt{L_g C_g}} = 1.1455 \times 10^8 \; m/s \tag{4.70}$$

L_k	f_1	f_2	$\omega_1\sqrt{L_k}$	$\omega_2\sqrt{L_k}$
4 nH/sqr	24.7 GHz	50.1 GHz	1562.16	3168.6
5 nH/sqr	22.1 GHz	46.1 GHz	1562.7	3259.76
6 nH/sqr	20.1 GHz	42.1 GHz	1556.9	3261
7 nH/sqr	18.5 GHz	38.9 GHz	1547.8	3254.6
8 nH/sqr	17.3 GHz	36.5 GHz	1547.3	3264.6
9 nH/sqr	16.3 GHz	34.3 GHz	1546.3	3253.9
10 nH/sqr	15.5 GHz	32.5 GHz	1550	3250

Table 4.1 Simulated values of ω_1 & ω_2 for various values of L_k. The fourth and fifth column indicate that the product $\omega\sqrt{L_k}$ remains almost constant confirming the relation

Also for a 50 Ω terminated 3 µm wide and 3µm ground spaced CPW, we estimate its impedance Z_{cpw} from ADS as

$$Z_{cpw} = 41.039 \; \Omega \tag{4.71}$$

We also know that $Z = \sqrt{L_g/C_g}$ and from equations (4.70) and (4.71) we have

$$L_g = \frac{41.039}{1.1455 \times 10^8} = 3.5823 \times 10^{-7} \; H/m \tag{4.72}$$

and C_g can be extracted as equal to $2.127 \times 10^{-10} \; F/m$. We can substitute .the value of C_g in equation (4.67) to obtain C_{2d} as ~$0.7 \times 10^{10} \; F/m$. This value of C_{2d} can be substituted in equation (4.64) to obtain the value of kinetic inductance per meter $L_{k,m}$

as ~$1 \times 10^{13}\ H/m$. Therefore the effective length over which the kinetic inductance accumulates is $(L_k\ per\ square)/(L_{k,m})$ which approximates to $1.35 \times 10^{-5}\ m$.

4.12 Conclusion

We have designed, simulated and tested a working capacitively coupled 2DEG mesa structure lying at the heterojunction of a $GaAs/Al_xGa_{1-x}As$ ($x = 0.3$), whose circuit model is verified from Burke (1999). The experimental results of transmission and reflection coefficients are in agreement with the simulations confirming the presence of a distributed kinetic inductance in 2DEG. We also propose a 2DEG coupled co-planar waveguide structure and its circuit model whose impedance and therefore transmission line coefficients are formulated analytically. Preliminary simulations take us closer to an accurate circuit model although the next step would be to practically test the structure and measure transmission coefficient.

REFERENCES

[1] Cosmic microwave background. (2016, April 4). In Wikipedia, The Free Encyclopedia. Retrieved 02:25, April 5, 2016, from https://en.wikipedia.org/w/index.php?title=Cosmic_microwave_background&oldid=713542897

[2] Atacama Large Millimeter Array. (2016, March 24). In Wikipedia, The Free Encyclopedia. Retrieved 02:45, April 5, 2016, from https://en.wikipedia.org/w/index.php?title=Atacama_Large_Millimeter_Array&oldid=711773938

[3] Schleeh, J., Alestig, G., Halonen, J., Malmros, A., Nilsson, B., Nilsson, P. A., ... & Grahn, J. (2012). Ultralow-power cryogenic InP HEMT with minimum noise temperature of 1 K at 6 GHz. Electron Device Letters, IEEE, 33(5), 664-666.

[4] Akgiray, A. H., Weinreb, S., Leblanc, R., Renvoise, M., Frijlink, P., Lai, R., & Sarkozy, S. (2013). Noise measurements of discrete HEMT transistors and application to wideband very low-noise amplifiers. Microwave Theory and Techniques, IEEE Transactions on, 61(9), 3285-3297.

[5] Yngvesson, S. (2012). Microwave semiconductor devices (Vol. 134). Springer Science & Business Media.

[6] De Jager, J. T. (1962). Parametric amplifiers for radio astronomy. Solid-State Electronics, 4, 266-270.

[7] Davies, R. (1965, january). Parametric amplifiers in radioastronomy. In radio and electronic engineer (vol. 29, no. 5, p. 312). 99 gower st, london wc1e 6az, england: inst electron & radio eng.

[8] Adam, R., Ade, P. A. R., Aghanim, N., Arnaud, M., Aumont, J., Baccigalupi, C., ... & Battaner, E. (2014). Planck intermediate results. XXX. The angular power spectrum of polarized dust emission at intermediate and high Galactic latitudes. arXiv preprint arXiv:1409.5738.

[9] Dicker, S. R., Ade, P. A. R., Aguirre, J., Brevik, J. A., Cho, H. M., Datta, R., ... & Ford, P. (2014, July). MUSTANG2: a large focal plan array for the 100 meter Green Bank Telescope. In SPIE Astronomical Telescopes+ Instrumentation (pp. 91530J-91530J). International Society for Optics and Photonics.

[10] Fuller, G. A., Avison, A., Beltran, M., Casasola, V., Caselli, P., Cicone, C., ... & Laing, R. (2016). The Science Case for ALMA Band 2 and Band 2+ 3. arXiv preprint arXiv:1602.02414.

[11] Swinbank, A. M., Simpson, J. M., Smail, I., Harrison, C. M., Hodge, J. A., Karim, A., ... & da Cunha, E. (2013). An ALMA survey of sub-millimetre Galaxies in the Extended Chandra Deep Field South: the far-infrared properties of SMGs.Monthly Notices of the Royal Astronomical Society, stt2273.

[12] Butikov, E. I. (2004). Parametric excitation of a linear oscillator. European Journal of Physics,25(4), 535.

[13] Sushrut Das. 2015. Microwave Engineering. Oxford University Press, Oxford, UK

[14] Manley, J. M., & Rowe, H. E. (1956). Some general properties of nonlinear elements-Part I. General energy relations. Proceedings of the IRE,44(7), 904-913.

[15] Decroly, J. C. (1973). Parametric amplifiers. John Wiley & Sons.

[16] Gray, B. R. (2012). Design of RF and microwave parametric amplifiers and power upconverters.

[17] Eom, B. H., Day, P. K., LeDuc, H. G., & Zmuidzinas, J. (2012). A wideband, low-noise superconducting amplifier with high dynamic range. Nature Physics, 8(8), 623-627.

[18] Adamyan, A. A., de Graaf, S. E., Kubatkin, S. E., & Danilov, A. V. (2016). Superconducting microwave parametric amplifier based on a quasi-fractal slow propagation line. Journal of Applied Physics, 119(8), 083901.

[19] Annunziata, A. J., Santavicca, D. F., Frunzio, L., Catelani, G., Rooks, M. J., Frydman, A., & Prober, D. E. (2010). Tunable superconducting nanoinductors. Nanotechnology, 21(44), 445202.

[20] Mattis, D. C., & Bardeen, J. (1958). Theory of the anomalous skin effect in normal and superconducting metals. Physical Review, 111(2), 412.

[21] Pozar, D. M. (2009). Microwave engineering. John Wiley & Sons.

[22] Garg, R., Bahl, I., & Bozzi, M. (2013). Microstrip lines and slotlines. Artech house.

[23] Shih, Y. C., Ton, T. N., & Bui, L. Q. (1988, May). Waveguide-to-microstrip transitions for millimeter-wave applications. In Microwave Symposium Digest, 1988., IEEE MTT-S International (pp. 473-475). IEEE.

[24] Fan, L., Li, M. Y., & Chang, K. (1995). Circular waveguide-to-microstrip transitions. Electronics Letters, 31(4), 294-295.

[25] Schulz, C., Pohl, N., & Rolfes, I. (2011, December). A broadband circular waveguide-to-microstrip transition for an 80 GHz FMCW radar system. In Microwave Conference Proceedings (APMC), 2011 Asia-Pacific (pp. 391-394). IEEE.

[26] Ramasami, V. (2007). HFSS-MATLAB-SCRIPTING-API. www. cresis, ku, edu, 2011-10-18.

[27] Leong, Y. C., & Weinreb, S. (1999, June). Full band waveguide-to-microstrip probe transitions. InMicrowave Symposium Digest, 1999 IEEE MTT-S International (Vol. 4, pp. 1435-1438). IEEE.

[28] Balanis, C. A. (2012). {Advanced Engineering Electromagnetics. Wiley.

[29] Sefa, R., & Maraj, A. (2011, May). Design of back-to-back tapered line transition. In Proceedings of the 10th WSEAS international conference on Telecommunications and informatics and microelectronics, nanoelectronics, optoelectronics, and WSEAS international conference on Signal processing (pp. 143-147). World Scientific and Engineering Academy and Society (WSEAS).

[30] "Tapered Lines", Jim Stiles The Univ. of Kansas Dept. of EECS http://www.ittc.ku.edu/~jstiles/723/handouts/section_5_8_Tapered_Lines_lecture.pdf

[31] Collin, R. E. (1956). The optimum tapered transmission line matching section. Proceedings of the IRE, 44(4), 539-548.

[32] Annunziata, A. J., Santavicca, D. F., Frunzio, L., Catelani, G., Rooks, M. J., Frydman, A., & Prober, D. E. (2010). Tunable superconducting nanoinductors. Nanotechnology, 21(44), 445202.

[33] Mattis, D. C., & Bardeen, J. (1958). Theory of the anomalous skin effect in normal and superconducting metals. Physical Review, 111(2), 412.

[34] Cohn, S. B. (1969). Slot line on a dielectric substrate. Microwave Theory and Techniques, IEEE Transactions on, 17(10), 768-778.

[35] Galejs, J. (1962). Excitation of slots in a conducting screen above a lossy dielectric half space. Antennas and Propagation, IRE Transactions on, 10(4), 436-443.

[36] Janaswamy, R., & Schaubert, D. H. (1986). Characteristic impedance of a wide slotline on low-permittivity substrates (short paper). Microwave Theory and Techniques, IEEE Transactions on,34(8), 900-902.

[37] Chramiec, J. (1989). Reactances of slotline short and open circuits on alumina substrate. Microwave Theory and Techniques, IEEE Transactions on,37(10), 1638-1641.

[38] Rizzoli, V., Mastri, F., & Masotti, D. (1991). Modeling the microstrip impedance step from direct measurements in the 1-27-GHz band.Microwave and Optical Technology Letters, 4, 562-566.

[39] Gopinath, A., Thomson, A. F., & Stephenson, I. M. (1976). Equivalent Circuit Parameters of Microstrip Step Change in Width and Cross Junctions (Short Papers). Microwave Theory and Techniques, IEEE Transactions on, 24(3), 142-144.

[40] Garg, R., & Bahl, I. J. (1978). Microstrip discontinuities. International Journal of Electronics Theoretical and Experimental, 45(1), 81-87.

[41] Zinieris, M. M., Sloan, R., & Davis, L. E. (1998). A broadband microstrip-to-slot-line transition.Microwave and Optical technology letters, 18(5), 339-342.

[42] Allen Jr, S. J., Tsui, D. C., & Logan, R. A. (1977). Observation of the two-dimensional plasmon in silicon inversion layers. Physical Review Letters,38(17), 980.

[43] Mittleman, D. (2003). Terahertz imaging. In Sensing with terahertz radiation(pp. 117-153). Springer Berlin Heidelberg.

[44] Barnes, W. L., Dereux, A., & Ebbesen, T. W. (2003). Surface plasmon subwavelength optics.Nature, 424(6950), 824-830.

[45] Ebbesen, T. W., Lezec, H. J., Ghaemi, H. F., Thio, T., & Wolff, P. A. (1998). Extraordinary optical transmission through sub-wavelength hole arrays.Nature, 391(6668), 667-669.

[46] Polman, A. (2008). Plasmonics applied. Science,322(5903), 868-869.

[47] Gramotnev, D. K., & Bozhevolnyi, S. I. (2010). Plasmonics beyond the diffraction limit. Nature photonics, 4(2), 83-91.

[48] Stern, F. (1967). Polarizability of a two-dimensional electron gas. Physical Review Letters, 18(14), 546.

[49] Andress, W. F., Yoon, H., Yeung, K. Y., Qin, L., West, K., Pfeiffer, L., & Ham, D. (2012). Ultra-subwavelength two-dimensional plasmonic circuits. Nano letters, 12(5), 2272-2277.

[50] Ju, L., Geng, B., Horng, J., Girit, C., Martin, M., Hao, Z., ... & Wang, F. (2011). Graphene plasmonics for tunable terahertz metamaterials.Nature nanotechnology, 6(10), 630-634.

[51] Yeung, K. Y., Yoon, H., Andress, W., West, K., Pfeiffer, L., & Ham, D. (2013). Two-path solid-state interferometry using ultra-subwavelength two-dimensional plasmonic waves. Applied Physics Letters, 102(2), 021104.

[52] Dyakonov, M., & Shur, M. (1996). Detection, mixing, and frequency multiplication of terahertz radiation by two-dimensional electronic fluid.Electron Devices, IEEE Transactions on, 43(3), 380-387.

[53] Knap, W., Dyakonov, M., Coquillat, D., Teppe, F., Dyakonova, N., Łusakowski, J., ... & Kasalynas, I. (2009). Field effect transistors for terahertz detection: physics and first imaging applications.Journal of Infrared, Millimeter, and Terahertz Waves, 30(12), 1319-1337.

[54] Peralta, X. G., Allen, S. J., Wanke, M. C., Harff, N. E., Simmons, J. A., Lilly, M. P., ... & Eisenstein, J. P. (2002). Terahertz photoconductivity and plasmon modes in double-quantum-well field-effect transistors. Applied Physics Letters, 81(9), 1627-1629.

[55] Shaner, E. A., Lee, M., Wanke, M. C., Grine, A. D., Reno, J. L., & Allen, S. J. (2005). Single-quantum-well grating-gated terahertz plasmon detectors. Applied Physics Letters, 87(19), 193507.

[56] Shaner, E. A., Grine, A. D., Wanke, M. C., Lee, M., Reno, J. L., & Allen, S. J. (2006). Far-infrared spectrum analysis using plasmon modes in a quantum-well transistor. Photonics Technology Letters, IEEE, 18(18), 1925-1927.

[57] Shaner, E. A., Wanke, M. C., Grine, A. D., Lyo, S. K., Reno, J. L., & Allen, S. J. (2007). Enhanced responsivity in membrane isolated split-grating-gate plasmonic terahertz detectors. Applied physics letters, 90(18), 181127.

[58] Dyer, G. C., Crossno, J. D., Aizin, G. R., Shaner, E. A., Wanke, M. C., Reno, J. L., & Allen, S. J. (2009). A plasmonic terahertz detector with a monolithic hot electron bolometer. Journal of Physics: Condensed Matter, 21(19), 195803.

[59] Barnes, W. L. (2004). Light-emitting devices: turning the tables on surface plasmons. Nature materials, 3(9), 588-589.

[60] Lin, B. J. F., Tsui, D. C., Paalanen, M. A., & Gossard, A. C. (1984). Mobility of the two-dimensional electron gas in GaAs-AlxGa1− xAs heterostructures. Applied Physics Letters, 45(6), 695-697.

[61] Rohlfing, M., Krüger, P., & Pollmann, J. (1993). Quasiparticle band-structure calculations for C, Si, Ge, GaAs, and SiC using Gaussian-orbital basis sets. Physical Review B, 48(24), 17791.

[62] Burke, P. J., Spielman, I. B., Eisenstein, J. P., Pfeiffer, L. N., & West, K. W. (2000). High frequency conductivity of the high-mobility two-dimensional electron gas. Applied Physics Letters,76(6), 745-747.

[63] Yoon, H., Yeung, K. Y., Umansky, V., & Ham, D. (2012). A Newtonian approach to extraordinarily strong negative refraction. Nature, 488(7409), 65-69.

[64] Yoon, H., Yeung, K. Y., Kim, P., & Ham, D. (2014). Plasmonics with two-dimensional conductors.Philosophical Transactions of the Royal Society of London A: Mathematical, Physical and Engineering Sciences, 372(2012), 20130104.

[65] Yoon, Hosang. 2014. Two-Dimensional Plasmonics in Massive and Massless Electron Gases. Doctoral dissertation, Harvard University.

[66] Dröscher, S., Roulleau, P., Molitor, F., Studerus, P., Stampfer, C., Ensslin, K., & Ihn, T. (2010). Quantum capacitance and density of states of graphene. Applied Physics Letters, 96(15), 152104.

[67] Luryi, S. (1988). Quantum capacitance devices.Applied Physics Letters, 52(6), 501-503.

[68] Staffaroni, M., Conway, J., Vedantam, S., Tang, J., & Yablonovitch, E. (2012). Circuit analysis in metal-optics. Photonics and Nanostructures-Fundamentals and Applications, 10(1), 166-176.

[69] Kraus, John D. (1984), Electromagnetics (3rd ed.), McGraw-Hill, ISBN 0-07-035423-5

[70] Hayt, William (1989), Engineering Electromagnetics (5th ed.), McGraw-Hill, ISBN 0-07-027406-1

[71] Kabir, N. A., Yoon, Y., Knab, J. R., Chen, J. Y., Markelz, A. G., Reno, J. L., ... & Bird, J. P. (2006). Terahertz transmission characteristics of high-mobility GaAs and InAs two-dimensional-electron-gas systems. Applied physics letters,89(13), 132109.

[72] Dutta, M. (2014). Hysteresis in the Conductance of Quantum Point Contacts with In-Plane Side Gates. (Electronic Thesis or Dissertation).

[73] Klopfenstein, R. W. (1956). A transmission line taper of improved design. Proceedings of the IRE,44(1), 31-35.